

Andreas Breivik

Fault Detection and Diagnosis of Induction Motor for Ship Propulsion by utilizing Electrical Signature and Finite Element Method

Master's thesis in Marine Technology

Supervisor: Amir R. Nejad

Co-supervisor: Mostafa Valavi

June 2021

Andreas Breivik

Fault Detection and Diagnosis of Induction Motor for Ship Propulsion by utilizing Electrical Signature and Finite Element Method

Master's thesis in Marine Technology
Supervisor: Amir R. Nejad
Co-supervisor: Mostafa Valavi
June 2021

Norwegian University of Science and Technology
Faculty of Engineering
Department of Marine Technology

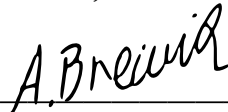
Preface

This master thesis is a part of the study programme Marine Technology at the Norwegian University of Science and Technology (NTNU). The work was carried out during the spring semester of 2021 for the course TMR4930 Marine Technology, master thesis, at the Department of Marine Systems Design/Machinery and has a weighting of 30 ECTS.

The focus of this thesis has been to analyze the effect of different faults in the induction motor for propulsion installed on the polar supply and research vessel SA Agulhaus II. This is motivated to be a contribution to the HealthProp project, which aims to develop a digital twin platform of the propulsion system onboard this vessel. The thesis assumes the reader has a basic knowledge of induction motors, condition monitoring techniques and finite element modelling.

Firstly, I would like to express my sincere thanks to my supervisor Amir Rasekhi Nejad who have provided me with the guidance, insightful discussions and help. Secondly, I would like to express my gratitude towards my co-supervisor, Mostafa Valavi, for his assistance throughout the whole thesis. His guidance, discussions and help is acknowledged and much appreciated.

Trondheim, 10th June 2021



Andreas Breivik

Summary

The induction motor studied in this thesis is one of two propulsion motors installed onboard the polar supply and research vessel SA Agulhaus II and the work is a contribution to the HealthProp Project (HealthProp 2020). HealthProp is a collaboration between German, Norwegian and South African partners and is funded through the EU MARTERA programme. The project aims to improve safety in Arctic and Antarctic operations by developing an intelligent predictive monitoring, life prediction and maintenance system.

This mater thesis presents a method for detection and diagnosis of stator short circuit, broken bar and eccentricity faults in large induction motors by analyzing the stator current frequency spectrum. This method has proven successful in past research. The novelty of the work done in this thesis includes modelling of different faults with Finite Element Method (FEM) analysis. To understand how the different faults affect the current spectrum of the induction motor, the working principle and characteristics of the current spectrum of the motor are presented.

To study the effect of the different fault conditions, time-stepping finite element (TSFE) - simulations were performed on a 2D model of the induction motor. Finite element method was used to perform dynamical simulation, which leads to more precise results than other models, as the reel geometry and winding layout of the machine are used. The different faults are modeled to represent real faults by modifying the model of a healthy motor. The model is based on the parameters of the induction motor used for propulsion onboard SA Agulhaus II. The three faults were modeled with different degree of fault severity to analyze the effect of a developing fault and if the fault could be detected at an incipient stage.

The thesis concludes that the proposed method can potentially detect and diagnose the different faults studied. Based on the novelty of the work performed, more simulations should be performed for different load profiles. The fault modelling and results should be verified with real data from the polar supply and research vessel SA Agulhaus II as the next step in developing a digital twin model of the propulsion system.

Sammendrag

Induksjonsmotoren studert i denne masteroppgaven er en av to fremdriftsmotorer installert ombord polarforsynings- og forskningsfartøyet SA Agulhaus II og arbeidet er et bidrag til HealthProp-prosjektet (HealthProp 2020). HealthProp er et samarbeid mellom tyske, norske og sørafrikanske partnere og finansieres gjennom EU MARTERA-programmet. Prosjektets mål er å forbedre sikkerheten i arktiske og antarktiske operasjoner ved å utvikle et intelligent system for prediktiv overvåking, livsprognose og vedlikehold.

Denne masteroppgaven presenterer en metode for deteksjon og diagnose av stator kortslutning, knekte rotorbarer og eksentrisitetsfeil i store induksjonsmotorer ved å analysere statorens strømfrekvensspektrum. Denne metoden har vist seg å være vellykket i tidligere forskningsarbeid. Det nye i denne oppgaven inkluderer modellering av de ulike feilene med FEM analyse. For å forstå hvordan de forskjellige feilene påvirker induksjonsmotorens strømspekter, presenteres virkemåten og egenskapene til motorens strømspekter.

For å studere effekten av de forskjellige feilene ble det utført simuleringer av time-stepping finite element (TSFE) på en 2D-modell av induksjonsmotoren. Finite element-metoden ble brukt til å utføre dynamisk simulering, noe som fører til mer presise resultater enn andre modeller, ettersom den virkelige geometrien og viklingsutformingen til maskinen brukes. De forskjellige feilene er modellert for å representere en reell feil ved å modifisere modellen til en frisk motor. Modellen er basert på parameterne til induksjonsmotoren som brukes til fremdrift ombord på SA Agulhaus II. De tre feilene ble modellert med ulik grad av alvorlighetsgrad for å analysere effekten av en utviklende feil og om feilen kunne oppdages på et tidlig stadium.

Oppgaven konkluderer med at den foreslåtte metoden potensielt kan oppdage og diagnostisere de forskjellige feilene som er undersøkt. Basert på den nye metoden i det utførte arbeidet, bør det utføres flere simuleringer for forskjellige lastprofiler. Feilmodelleringen og resultatene bør verifiseres med reelle data fra polarforsynings- og forskningsfartøyet SA Agulhaus II som neste trinn i utviklingen av en digital tvilling av fremdriftssystemet.

Contents

| | |
|---|-------------|
| Preface | iii |
| Summary | v |
| Sammendrag | vii |
| Contents | ix |
| Figures | xiii |
| Tables | xv |
| Abbreviations | xvii |
| 1 Introduction | 1 |
| 1.1 Motivation | 2 |
| 1.2 SA Agulhaus II | 3 |
| 1.3 Objectives | 3 |
| 1.4 Scope of work | 4 |
| 1.5 Limitations | 4 |
| 1.6 Outline | 5 |
| 2 Induction Motor | 7 |
| 2.1 Induction characteristics | 8 |
| 2.1.1 Space MMF harmonics | 9 |
| 2.1.2 Slot harmonics | 9 |
| 2.1.3 Saturation permeance harmonics | 10 |
| 2.2 Application in Maritime industry | 11 |
| 2.2.1 System design | 11 |
| 2.2.2 Mechanical propulsion system | 11 |
| 2.2.3 Hybrid propulsion system | 12 |
| 2.2.4 Electrical propulsion system | 12 |
| 2.2.5 Electrical propulsion with DC hybrid power supply | 13 |
| 3 Fault overview | 15 |
| 3.1 Classification of faults | 15 |
| 3.2 Fault types | 17 |
| 3.2.1 Stator faults | 18 |
| 3.2.2 Rotor Faults | 19 |
| 3.2.3 Effect of rotor unbalance and eccentricity | 20 |
| 3.2.4 Bearing Faults | 21 |
| 3.3 Fault signatures | 24 |
| 3.3.1 Stator fault characteristics | 24 |

| | | |
|----------|---|-----------|
| 3.3.2 | Broken rotor bar characteristics | 25 |
| 3.3.3 | Eccentricity fault characteristics | 26 |
| 4 | Condition Monitoring and Fault Detection | 29 |
| 4.1 | Introduction | 29 |
| 4.2 | Overview of prognosis and health management | 29 |
| 4.3 | Condition monitoring of ship propulsion systems | 31 |
| 4.3.1 | State of the art in marine industry | 32 |
| 4.3.2 | Development trend | 32 |
| 4.4 | Measurement signals | 33 |
| 4.4.1 | Vibration analysis | 33 |
| 4.4.2 | Motor current signature analysis | 35 |
| 4.4.3 | Temperature | 35 |
| 4.5 | Data acquisition | 35 |
| 4.5.1 | Location of measurement | 36 |
| 4.6 | Signal processing | 36 |
| 4.6.1 | Fast Fourier Transform | 37 |
| 4.6.2 | STFT | 37 |
| 4.7 | State of the art: Induction motor fault detection | 38 |
| 5 | FEM modelling | 41 |
| 5.1 | Modeling of the Healthy Induction Motor | 42 |
| 5.1.1 | Effect of parallel branches | 42 |
| 5.1.2 | Mesh | 43 |
| 5.2 | Fault modeling | 45 |
| 5.2.1 | Modelling of inter turn short circuit fault | 45 |
| 5.2.2 | Modelling of broken rotor bar | 46 |
| 5.2.3 | Modelling of static eccentricity fault | 47 |
| 5.2.4 | Modelling of dynamic eccentricity | 48 |
| 5.3 | Signal processing | 49 |
| 5.4 | Simulations | 50 |
| 5.4.1 | ITSC fault simulation | 50 |
| 5.4.2 | Broken rotor bar simulations | 50 |
| 5.4.3 | Eccentricity fault simulations | 50 |
| 6 | Results | 51 |
| 6.1 | Healthy Motor | 52 |
| 6.1.1 | Healthy motor with external circuit | 52 |
| 6.1.2 | Healthy motor without external circuit - Lower Frequency Range | 53 |
| 6.1.3 | Healthy motor without external Circuit - Higher Frequency Range | 54 |
| 6.2 | ITSC faults - 1 or 2 coils with Short Circuit | 55 |
| 6.2.1 | 1 Turn Short Circuit | 55 |
| 6.2.2 | 3 Turn Short Circuit | 56 |
| 6.2.3 | 6 Short Circuited Turns in one phase | 57 |
| 6.2.4 | 6 Turn Short Circuited - 3 turns in 2 coil | 58 |
| 6.2.5 | 9 Short Circuited Turns | 59 |
| 6.2.6 | 12 Turn Short Circuited - 6 turns in 2 coil | 60 |

| | | |
|----------|---|-----------|
| 6.3 | ITSC Fault - Percent of turns in one phase | 61 |
| 6.3.1 | 5% ITSC of phase A | 61 |
| 6.3.2 | 10% ITSC of phase A | 62 |
| 6.3.3 | 15% ITSC of phase A | 63 |
| 6.3.4 | 20% ITSC of phase A | 64 |
| 6.4 | Broken Bar Fault | 65 |
| 6.4.1 | 1 Broken Bar | 65 |
| 6.4.2 | 2 Broken Bars | 66 |
| 6.4.3 | 3 Broken Bars | 67 |
| 6.4.4 | 2 Broken Bars - 90 deg relative | 68 |
| 6.4.5 | 2 Broken Bars - 180 deg relative | 69 |
| 6.5 | Eccentricity fault | 70 |
| 6.5.1 | Static Eccentricity | 70 |
| 6.5.2 | Dynamic Eccentricity | 71 |
| 6.6 | Comparison of healthy and faulty cases | 72 |
| 6.6.1 | ITSC Faults with % Short Circuited Turns in Phase A | 72 |
| 6.6.2 | ITSC Fault in 1 or 2 Coils | 73 |
| 6.6.3 | Broken Bar Faults | 75 |
| 6.6.4 | Eccentricity Faults | 75 |
| 7 | Discussion | 77 |
| 7.1 | Healthy motor | 77 |
| 7.2 | ITSC fault | 78 |
| 7.2.1 | ITSC Faults in one and two coils | 78 |
| 7.2.2 | ITSC Faults - Percent in one phase | 78 |
| 7.3 | Broken Bar Faults | 78 |
| 7.4 | Eccentricity Faults | 79 |
| 7.4.1 | Static Eccentricity | 79 |
| 7.4.2 | Dynamic Eccentricity | 79 |
| 8 | Conclusion and Further Work | 81 |
| | Bibliography | 83 |

Figures

| | | |
|------|--|----|
| 1.1 | SA Agulhaus II on a voyage in Antarctica (de Waal et al. 2018) | 2 |
| 1.2 | Shaft arrangement of one shaft onboard SA Agulhaus II | 3 |
| 1.3 | Flow chart of the thesis structure | 6 |
| 2.1 | Illustration of induction motors | 7 |
| 2.2 | Equivalent circuit for induction motor operation (Kirtley et al. 2015) | 8 |
| 2.3 | Different propulsion systems | 12 |
| 2.4 | Different propulsion systems | 14 |
| 3.1 | Sources of Machinery Faults | 15 |
| 3.2 | Schematic diagram of the Internal Faults | 16 |
| 3.3 | Schematic diagram of the External Faults | 16 |
| 3.4 | Results failure distribution (Bazurto et al. 2016) | 18 |
| 3.5 | Failure distribution in induction motors (Bazurto et al. 2016) | 18 |
| 3.6 | Proportion of bearing fault in mechanical faults of motor (Bagheri et al. 2020) . | 19 |
| 3.7 | Schematic representation of stator possible failure modes (Eftekhari et al. 2014) | 19 |
| 3.8 | Illustration of broken rotor bar (Glowacz 2016) | 20 |
| 3.9 | Illustration of eccentricity faults (Miljković 2015) | 20 |
| 3.10 | Sleeve bearing and Forces acting on a shaft (Tavner et al. 2008) | 22 |
| 3.11 | Bearing components and main dimensions (Gonçalves et al. 2015) | 23 |
| 4.1 | Flowchart of the PHM of rotating machinery (Lei 2017) | 30 |
| 4.2 | Condition monitoring and stages of identification of an incipient failure - over- view (Ibrion et al. 2021) | 33 |
| 4.3 | Range of typical values for zone boundaries (ISO 2016) | 34 |
| 4.4 | Visual illustration of FFT (UiO 2019) | 37 |
| 4.5 | Visual illustration of STFT (Fischman 1997) | 38 |
| 5.1 | Induction motor model in Maxwell | 42 |
| 5.2 | Schematic diagram of phase A stator winding | 43 |
| 5.3 | Mesh of the whole motor | 43 |
| 5.4 | Air-gap mesh in Maxwell | 44 |
| 5.5 | The external circuit for inter-turn short circuit fault | 45 |
| 5.6 | Short circuited coils in Maxwell | 46 |
| 5.7 | Broken rotor bar in Maxwell | 47 |

6.1 Current frequency spectrum of the healthy motor with external circuit 52

6.2 Low range current frequency spectrum of the healthy motor 53

6.3 High range current frequency spectrum of the healthy motor 54

6.4 Current frequency spectrum of 1 short circuited turn 55

6.5 Current frequency spectrum of 3 short circuited turns 56

6.6 Current frequency spectrum with 6 short circuited turns 57

6.7 Current frequency spectrum with 6 turn short circuited, 3 turns in 2 coils 58

6.8 Current frequency spectrum with 9 short circuited turns 59

6.9 Current frequency spectrum with 12 short circuited turns 60

6.10 Current frequency spectrum for 5% short circuited phase 61

6.11 Current frequency spectrum for 10% short circuited phase 62

6.12 Current frequency spectrum for 15% short circuited phase 63

6.13 Current frequency spectrum for 20% short circuited phase 64

6.14 Current frequency spectrum with 1 Broken Bar 65

6.15 Current frequency spectrum with 2 Broken Bars 66

6.16 Current frequency spectrum with 3 Broken Bars 67

6.17 Current frequency spectrum with 2 Broken Bars 90 deg relative to each other . . 68

6.18 Current frequency spectrum with 2 Broken Bars 180 deg relative to each other . 69

6.19 Current frequency spectrum with static eccentricity of 1mm 70

6.20 Current frequency spectrum with dynamic eccentricity of 1mm 71

6.21 Comparison of lower range current frequency components for % ITSC of Phase A 72

6.22 Comparison of mid range current frequency components for % ITSC of Phase A 73

6.23 Comparison of upper range current frequency components for % ITSC of Phase A 73

6.24 Comparison of lower current frequency components with ITSC fault 74

6.25 Comparison of upper current frequency components with ITSC fault 74

6.26 Comparison of current frequency components with broken bar fault 75

6.27 Comparison of lower range current frequency components with eccentricity fault 76

6.28 Comparison of upper range current frequency components with eccentricity
 fault 76

Tables

| | | |
|------|---|----|
| 1.1 | Vessel specification | 3 |
| 2.1 | Space harmonic orders of induction motor | 9 |
| 3.1 | Source fault classification | 17 |
| 5.1 | General motor parameters | 41 |
| 5.2 | Coil parameters for ITSC fault | 46 |
| 5.3 | Characteristic frequencies for ITCS fault | 46 |
| 5.4 | Characteristic frequencies for broken rotor bar fault | 47 |
| 5.5 | Static eccentricity parameters in Maxwell | 47 |
| 5.6 | Characteristic frequencies for static eccentricity | 48 |
| 5.7 | Dynamic eccentricity parameters in Maxwell | 48 |
| 5.8 | Characteristic frequencies for static eccentricity | 48 |
| 5.9 | Time step for the different fault simulations | 49 |
| 5.10 | Signal length of the different fault simulations | 49 |
| 5.11 | ITSC fault simulations | 50 |
| 5.12 | Broken rotor bar fault simulations | 50 |
| 5.13 | Eccentricity fault simulations | 50 |
| 6.1 | Significant amplitudes of FFT spectrum for healthy motor | 52 |
| 6.2 | Significant amplitudes of FFT spectrum - 1 turn short circuited | 55 |
| 6.3 | Significant amplitudes of FFT spectrum - 3 turns short circuited | 56 |
| 6.4 | Significant amplitudes of FFT spectrum - 6 turns short circuited | 57 |
| 6.5 | Significant amplitudes of FFT spectrum - 6 Turn Short Circuited, 3 in 2 coils | 58 |
| 6.6 | Significant amplitudes of FFT spectrum - 9 turn short circuited | 59 |
| 6.7 | Significant amplitudes of FFT spectrum - 12 turn short circuited | 60 |
| 6.8 | Significant amplitudes of FFT spectrum - 5% short circuited phase | 61 |
| 6.9 | Significant amplitudes of FFT spectrum - 10% short circuited phase | 62 |
| 6.10 | Significant amplitudes of FFT spectrum - 15% short circuited phase | 63 |
| 6.11 | Significant amplitudes of FFT spectrum - 20% short circuited phase | 64 |
| 6.12 | Significant amplitudes of FFT spectrum - 1 Broken Bar | 65 |
| 6.13 | Significant amplitudes of FFT spectrum - 2 Broken Bars | 66 |
| 6.14 | Significant amplitudes of FFT spectrum - 3 Broken Bars | 67 |
| 6.15 | Significant amplitudes of FFT spectrum - 2 Broken Bars 90 deg | 68 |

| | |
|---|----|
| 6.16 Significant amplitudes of FFT spectrum - 2 Broken Bars 180 deg | 69 |
| 7.1 Current spectrum content - Healthy motor | 77 |

Abbreviations

AC Alternating Current.

AI Artificial Intelligence.

CMB Condition Based Maintenance.

DAQ Data Acquisition.

DC Direct Current.

DFT Discrete Fourier Transform.

EMF Electromotive Force.

FEM Finite Element Method.

FFT Fast Fourier Transform.

FT Fourier Transform.

HVAC Heating, Ventilation and Air Conditioning.

IMO International Maritime Organisation.

ITSC Inter Turn Short Circuit.

LSB Lower Side Band.

MCSA Motor Current Signal Analysis.

MMF Magnetomotive Force.

PCMS Propulsion Condition Monitoring Service.

PHM Prognosis and Health Management.

PMS Power Management System.

RPM Revolutions Per Minute.

RSH Rotor slot harmonics.

RUL Remining Useful Life.

SFOC Specific Fuel Oil Consumption.

STFT Short Time Fourier Transform.

TSFE Time-Stepping Finite Element.

USB Upper Side Band.

VSD Variable Speed Drive.

Chapter 1

Introduction

Electric propulsion of ships has increased steadily for several decades. Since the early 20th century, icebreakers have utilized Direct Current (DC) motors for icebreaking capabilities. The flexibility of control of electrical motors is the reason for this, where rapid control leads to more effective operation. The electric motor can rapidly change from forward to reverse operation. This allows the ship to “ram” and break up ice formations. When sophisticated power electronics devices became available, a transition to synchronous and induction machines was made (Kirtley et al. 2015).

For the 2019 Safety and Shipping Review, Allianz Global Corporate & Specialty SE analyzed 26,022 shipping incidents between January 2009 and December 2018. Of these incidents, more than a third (8,862) were caused by machinery damage or breakdown, such as engine failure. This is over twice as many as the next highest causes of incidents, being collision (3,648) and wrecked/stranded (3,610) (Safety4sea 2019). In a wide variety of industrial applications, an increasing demand exists to improve the reliability and availability of critical systems. A sudden failure of a system in these examples may lead to cost expensive downtime, damage to surrounding equipment or even danger to humans. Monitoring and failure detection improves the reliability and availability of an existing system. Since various failures degrade relatively slowly, there is potential for fault detection followed by corrective maintenance at an early stage. This avoids the sudden, total system failure, which can have serious consequences.

Induction machines are widely used in industrial applications thanks to their reliability, ruggedness, and low cost. Unfortunately, several faults can occur, leading to process failure, loss of propulsion, or damage to humans and surrounding equipment. Because of this, much research has been done within the field of fault detection and diagnosis of induction motors in the past decades. The research includes many different methods for detecting and diagnosing faults and is mainly done for smaller motors.

In this thesis, a method for fault detection and diagnosis of stator short circuit, broken bar and eccentricity faults for the induction motor for propulsion installed onboard the icebreaker SA Ahulhaus II polar supply vessel will be presented.

1.1 Motivation

The research done in this thesis is a contribution to the HealthProp project. HealthProp is a collaboration between German, Norwegian and South African partners and is funded through the EU MARTERA programme. The project aims to improve safety in Arctic and Antarctic operations by developing an intelligent predictive monitoring, life prediction and maintenance system. The components include power generation, power transmission and propeller. The SA Agulhas II polar supply and research vessel from South Africa is selected as the case study for validation of tools and models. A picture of the research vessel is shown in figure 1.1.



Figure 1.1: SA Agulhaus II on a voyage in Antarctica (de Waal et al. 2018)

The main goal of HealthProp is to develop a digital twin platform towards monitoring the propulsion system and driveline of ships in Arctic and Antarctic operations, to improve the system reliability and increase the operational safety in harsh environmental conditions. The models, developed and verified by the project partners through real data measurements from the research vessel SA Agulhas II in South Africa, will be used in a virtual model of the propulsion system for life prediction, fault detection and robust decision support during ice navigation. The developed digital twin will be tested on SA Agulhas II to estimate the remaining useful life of her propulsion machinery and -components and to predict failure due to ice impact. The data and findings are relevant to the information and further develop new codes and guidelines for Arctic and Antarctic operations.

1.2 SA Agulhaus II

The polar research and polar vessel, SA Agulhas II, is propelled by two induction motors of 4,5MW each. Each motor is connected to a propulsion shaft with four-bladed variable pitch propellers. Four 3MW diesel generators are used to supply propulsion power. The ship was manufactured in Rauma shipyard in 2012 by STX Finland with an ice-strengthened hull in accordance with DNV ICE-10. She is classified to Polar Ice Class PC-5 and therefore rated for year-round operations in medium first-year ice containing old ice inclusions. Further specifications of the vessel are presented in Table 1.1. An illustration of the shaft arrangement of one propeller is shown in figure 1.2 below.

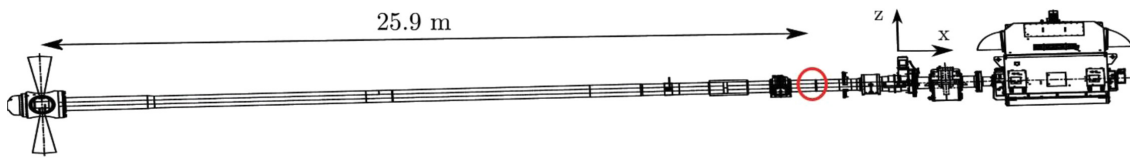


Figure 1.2: Shaft arrangement of one shaft onboards SA Agulhaus II

Table 1.1: Vessel specification

| | | | |
|-------------------|------------------|------------------------------|--------------------|
| Gross tonnage | 12,897 tons | Diesel engine type | 6 L32 |
| Length | 134 m | Electric motor type | N3 HXC 1120 LL8 |
| Breadth | 22 m | Speed (n) at MCR | 140rpm |
| Classification | DNV | Power (P_D) at MCR | 4500 kW |
| Class notation | 1A1 PC-5/ICE-10 | Nominal torque (Q_{MCR}) | 307kNm |
| Yard/Year | STX Finland/2012 | Propeller maker | Rolls-Royce |
| Main engine maker | Wärtsilä | No. of blades/ Diameter | 4/4.3 m |

1.3 Objectives

The main objective of this thesis was to detect and diagnose stator short circuit, broken bar and eccentricity faults in large induction motors with Motor Current Signal Analysis (MCSA). To answer the main objective of the thesis, seven part objectives will be answered:

1. How does the current frequency spectrum for a healthy motor look like?
2. What are the sources of faults in induction motors?
3. What are the characteristics of the different faults?
4. How is fault detection and diagnosis done today?
5. How can the different faults be modelled?
6. How is the current frequency spectrum affected in the presence of different faults?
7. Can the faults be detected at an incipient stage?

To study the effect of the fault conditions mentioned above, Time-Stepping Finite Element (TSFE)- simulation were performed on a 2D model of the induction motor.

1.4 Scope of work

This section describes the scope of the work done in this thesis and an explanation for including the specific literature.

- An overview of the working principle of the induction motor and it's application in the marine industry.
- A presentation of the different fault sources and the resulting fault in the induction motor. Their consequence and signature are also presented.
- An overview of condition monitoring in general, what is done in the marine industry today, and the different steps for conducting fault detection and diagnosis.
- TSFE -modeling and simulation of an induction motor operating under healthy and faulty conditions.
- Evaluate the current spectrum of the models with a focus on the signatures presented in the literature.

The literature and theory presented in this thesis are the information needed to understand how condition monitoring is done and the operating principle of an induction motor to understand how the different faults affect the induction motor.

1.5 Limitations

The lack of available experimental setup limits the thesis to investigating the fault signatures through simulations. The simulation was performed with Maxwell Ansys v.2021 R1, which is capable of performing electromagnetic TSFE-simulations. The simulations were limited by the thesis's time constraint. Because of the time constraint, a 2D model was used instead of a 3D model, limiting the thesis to assuming the faults have a symmetrical effect in the axial direction, which is not necessarily the case for dynamic eccentricity, which are introduced in chapter 3.2. To reduce the computation time further, the core losses and eddy current losses for all parts were not included. This simplification is based on the assumption that the core losses and eddy current effects will have minimal impact on the fault induced harmonic spectrum. The motor and winding geometry was simplified, components with little effect on the magnetic field, like insulation and slot wedge, was modelled as air. The simulations were done with and without an external circuit. This can affect the harmonic components of the current spectrum.

1.6 Outline

Chapter 2: Induction Motors

This chapter presents the working principle and characteristics of induction motors. In addition, applications in the marine industry is described, and different system design is presented. The first research question will be answered here.

Chapter 3: Fault overview

This chapter presents an overview of the faults that can occur in an induction motor. In addition, the most common faults are explained in detail, and their signature is discussed. The second and third research question will be answered in this chapter.

Chapter 4: Condition monitoring and fault detection

In this chapter, condition monitoring and fault detection techniques are presented and some focus points for implementation. In addition, state of art in the industry is presented. The fourth research question will be answered here.

Chapter 5: FEM Modeling

This chapter presents the modeling of the induction motor studied in this thesis. The parameters of the motor and how the different faults are modeled is shown. The fifth research question is answered here

Chapter 6:Results

In this chapter, the spectral analysis of the different faults are presented. In addition, a comparison of different fault severity for each fault are shown.

Chapter 7: Discussion

The results from Chapter 6 is discussed in this chapter. The trends and correlations between the faults are explained in addition to a comparison with the literature.

Chapter 8: Conclusion

The key findings from chapter 6 are presented, and concluding remarks from the results are presented in addition to recommendations for further work. Research question six and seven are answered here.

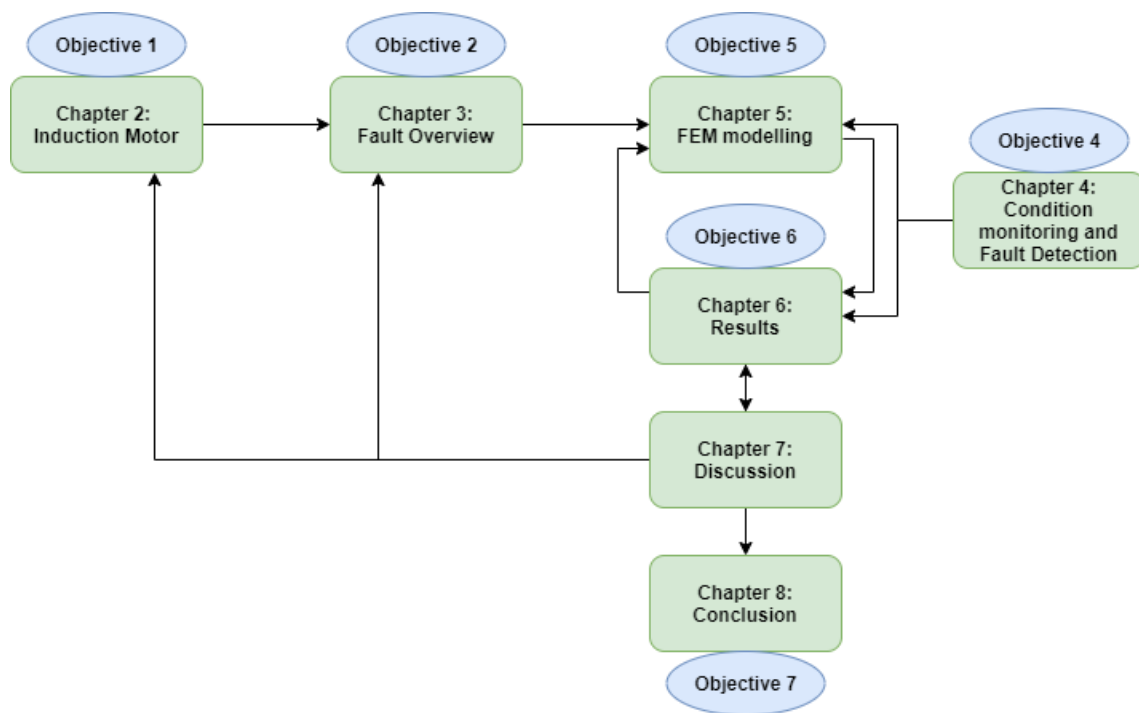
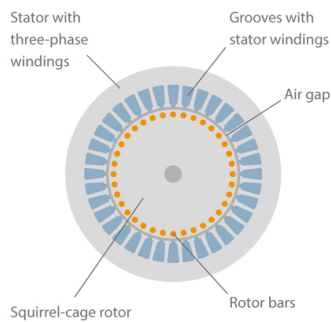


Figure 1.3: Flow chart of the thesis structure

Chapter 2

Induction Motor

Induction motors are probably the most common electrical motor in industrial, commercial, and residential applications today. The reason for this is the simple and rugged construction. The design of the induction motor makes it economical to build and is reasonably compact and efficient. An example of an induction motor used for ship propulsion is shown in figure 2.1b, where the simple and rugged construction is presented.



(a) Axial view of induction motor (Kirtley et al. 2015)



(b) Induction motor for ship propulsion (Kirtley et al. 2015)

Figure 2.1: Illustration of induction motors

The main components of an induction motor are the stator, rotor, and motor housing. The stator contains polyphase windings, which produce a rotating flux wave in the stator and air gap of the motor. The rotor might have a winding similar to that of the stator, but most often, it has a so-called squirrel cage. A squirrel cage is built by a number of uniformly spaced conductors, often copper, around the periphery of the rotor. These conductors are shorted by conduction end rings. An exploded view of an induction motor is shown in Figure 2.1a. The rotating flux wave produced by the stator is turning at a speed with respect to the stator as shown below,

$$\Omega_s = \frac{\omega}{p} \quad (2.1)$$

where ω is the electrical frequency supplied to the motor and p is the number of pole pairs. From equation 2.1 the rotating speed of the induction motor is a function of the electrical

frequency, which can be regulated using a Variable Speed Drive (VSD). In an induction motor, the rotor is turning at a speed that is generally less than the rotating speed of the flux wave produced by the polyphase voltage in the stator. The reason for this is that the mechanical force on the rotor is created by the induced current in the rotor. The motion of the flux wave with respect to the rotor induces currents in the rotor conductors, and those currents interact with the flux wave to produce torque. This current is induced by the relative movement between the rotating flux wave produced by the polyphase voltage in the stator and the conductors in the squirrel cage of the rotor. When the rotor and stator are rotating at the same speed, no mechanical force is applied to the rotor, hence no torque is produced. This results in a drop of the speed of the rotor. This leads to a relative speed difference between the rotor and stator, so the rotor speed is always lower than the rotation of the flux wave. This is called the "slip" of the motor. The slip can be calculated from equation 2.2 below,

$$\omega_r = s\omega = \omega - \omega_m = \omega - p\Omega \quad (2.2)$$

where s is a dimensionless quantity being the relative "slip" between the rotor and the rotating flux wave. The equivalent circuit for induction motor operation shown in figure 2.2 shows the effect of the relative frequency seen by the rotor by dividing the rotor resistance by slip. This shows that the voltage induced in the rotor is proportional to frequency and hence the slip. This results in equation 2.3 which represents the power crossing the air gap (Kirtley et al. 2015).

$$P_{ag} = q|I_2|^2 \frac{R_2}{s} \quad (2.3)$$

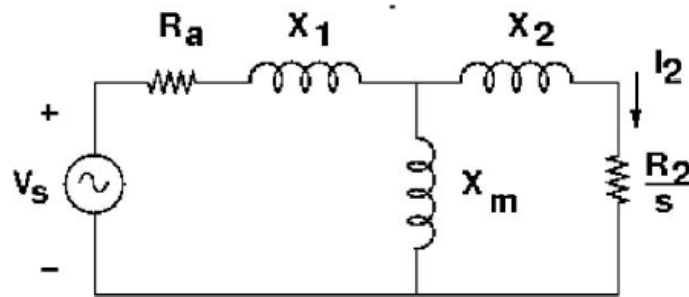


Figure 2.2: Equivalent circuit for induction motor operation (Kirtley et al. 2015)

2.1 Induction characteristics

To understand how faults in an induction motor affect its operation, the working principle must be explained more in detail. In this section, the characteristics of the stator current spectrum of a healthy induction motor will be explained. This includes a description of the different

harmonics produced in the in the motor as a result of induced Magnetomotive Force (MMF) waves. The harmonics included, are the space harmonics, slot permeance harmonics and the saturation permeance harmonics.

2.1.1 Space MMF harmonics

The stator winding of a symmetrical induction machine produces a series of MMF waves given by equation 2.4.

$$F_s(t, \theta) = \sum_{\nu} F_{\nu} \cos(\omega_1 t - \nu p \theta) \quad (2.4)$$

where p is the number of pole pairs, ω_1 is the mains angular frequency, and ν is the harmonic order (Joksimovic and Penman 2000). Due to the placement of the stator windings in the slots of the induction motor, the phase as well as the resulting rotating MMF wave shape is stepwise. This result in rotating MMF beside the fundamental harmonic with p pole pairs contain higher space harmonics. The above-mentioned series of MMF space harmonics are defined by the well-known expression (Joksimovic, Riger et al. 2011),

$$\nu = 6g + 1, \quad g = 0, \pm 1, \pm 2, \dots \quad (2.5)$$

where ν is the harmonic order. Table 2.1 present the first harmonic orders calculated from equation 2.5.

| g | Harmonic order (ν) |
|-----|--------------------------|
| 0 | 1 |
| -1 | 5 |
| 1 | 7 |
| -2 | 11 |
| 2 | 13 |
| -3 | 17 |
| 3 | 19 |

Table 2.1: Space harmonic orders of induction motor

2.1.2 Slot harmonics

The above mentioned MMF waves in 2.1.1, induce currents in the rotor bars. This current produce its own MMF waves. The resulting harmonics are reffered to as Rotor slot harmonics (RSH). RSH are of much interest in cage induction motors. These harmonics are not only the most prominent harmonic of rotor MMF, but also only exist in the spectrum beside the fundamental rotor MMF wave. The rotor cage reacts on the flux density waves from the stator with the following three series of MMF waves,

$$M_1 = M_{1m} \cos(s_{\nu} \omega t - \nu p \theta_r) \quad (2.6)$$

$$M_2 = M_{2m} \cos\left(s_v \omega t + \left(\frac{\lambda R}{p} - v\right) p \theta_r\right) \quad (2.7)$$

$$M_3 = M_{3m} \cos\left(s_v \omega t - \left(\frac{\lambda R}{p} + v\right) p \theta_r\right) \quad (2.8)$$

where $s_v = 1 - v(1 - s)$, R is the number of rotor bars and $\lambda = 1, 2, 3, \dots$

In an unsaturated machine, these MMF waves interact with the constant air-gap permeance. This produces flux density waves with the same shape. These waves, seen from the stator frame, are:

$$B_1 = B_{1m} \cos(\omega t - v p \theta_s) \quad (2.9)$$

$$B_2 = B_{2m} \cos\left(\left(1 - \lambda \frac{R}{p}(1 - s)\right) \omega t + \left(\frac{\lambda R}{p} - v\right) p \theta_s\right) \quad (2.10)$$

$$B_3 = B_{3m} \cos\left(\left(1 + \lambda \frac{R}{p}(1 - s)\right) \omega t - \left(\frac{\lambda R}{p} + v\right) p \theta_s\right) \quad (2.11)$$

This results in all the flux density harmonics from the stator side are reflected by the rotor at the fundamental frequency. This results in a series of two additional slip dependent frequencies, located in the higher current frequency spectrum of the stator. These frequencies are referred to as the lower and upper rotor slot harmonics (Joksimovic, Riger et al. 2011), expressed by equation 2.12 and 2.13.

$$f_{RSH-L} = \left(1 - \lambda \frac{R}{p}(1 - s)\right) f_1, \quad (2.12)$$

$$f_{RSH-U} = \left(1 + \lambda \frac{R}{p}(1 - s)\right) f_1, \quad (2.13)$$

2.1.3 Saturation permeance harmonics

The MMF waves in a saturated induction machine, through variable air-gap permeance, induce flux density waves that do not exist in an unsaturated machine. These waves are,

$$B_4 = B_{4m} \cos((1 - (2 - v)(1 - s)) \omega t + (v - 2) p \theta_r), \quad (2.14)$$

$$B_5 = B_{5m} \cos((3 - (v + 2)(1 - s)) \omega t - (v + 2) p \theta_r) . \quad (2.15)$$

Because these waves exist, new MMF waves in the cage rotor can appear. Nevertheless, these new MMF waves, as described above, can induce the Electromotive Force (EMF) and lead to currents in the stator winding. In a saturated machine, the new frequency components are referred to as saturation lower and upper harmonic. These new stator current components can be expected only at the following frequencies (Joksimovic, Riger et al. 2011),

$$f_{s-L} = \left(3 - \lambda \frac{R}{p}(1 - s)\right) f_1 \quad (2.16)$$

$$f_{s-u} = \left(3 + \lambda \frac{R}{p} (1-s) \right) f_1. \quad (2.17)$$

2.2 Application in Maritime industry

Electric propulsion has existed for more than 100 years (Hansen and Wendt 2015). There are examples of diesel-electric propulsion systems back to 1903. Despite a few examples of early-stage diesel-electric propulsion systems, the first generation of electric ship propulsion is usually considered as the ones built in the 1920s (Hansen and Wendt 2015). High propulsion power demand was the reason for this. Turbo-electric generators could only achieve this at this time. A steam turbine generator powered each propeller, and by varying the generator speed, the propulsion motor speed was controlled. As the diesel engines were developed further and took over as direct propulsion prime movers, the electric propulsion solution was seldom used until the 1980s (Hansen and Wendt 2015). At this time, semiconductor technology was developed, and this opened new solutions for controlling the speed of electric motors. At first, the variable speed motors were DC motors, controlled by thyristor rectifiers. Further, the development of frequency converters made it possible to regulate the speed of Alternating Current (AC) motors as well. The possibility of operating the propeller with a variable speed independent from the generator operation resulted in new ways of applying electric propulsion. This meant that the onboard power system could be designed as any land-based industrial power plant with multiple generator sets. This solution was welcomed in several sectors of the marine industry where the operational profile varied much or had large electrical consumers onboard. These were typically cruise vessels, ice breakers, offshore oil and gas exploration vessels (Hansen and Wendt 2015). The main reason for utilizing electric propulsion for vessels with a varying operational profile is that variable speed controlled electric motors have a high efficiency of approx. 95 % between 5% and 100% of rated power. Compared to conventional combustion engines, where the optimum efficiency is around 85%-90% of rated power and dropping considerably at lower load operation, electrical propulsion with variable speed control will contribute to fuel savings and more flexible operation of the propulsion system (Hansen and Wendt 2015).

2.2.1 System design

The ship propulsion system onboard a vessel is often designed for the specific type of vessel and operational profile. This results in several different types of solutions. This section presents the similarities and differences of four commonly found propulsion systems onboard ships.

2.2.2 Mechanical propulsion system

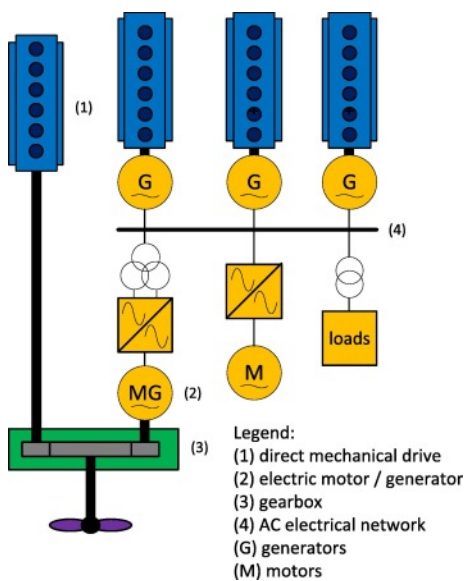
The architecture of a conventional ship with mechanical propulsion system is illustrated in Figure 2.3b. The prime mover (1) is usually a diesel engine supplying power to the shaft (3) through a gearbox (2) if the Revolutions Per Minute (RPM) have to be reduced. The gearbox is required if the RPM of the engine is higher than the required RPM for the propeller. For a slow speed two-stroke engine, the gearbox is often not needed, but for four-stroke medium

speed engines running on RPM of 500+, the gearbox is needed. A set of diesel generators is required to supply power to auxiliary loads like bow thrusters, cargo pumps, cranes, Heating, Ventilation and Air Conditioning (HVAC) and other auxiliary systems.

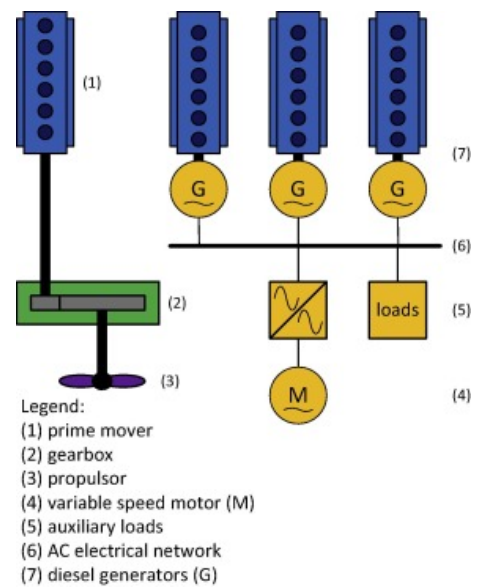
2.2.3 Hybrid propulsion system

Ships that often operates at low speed can reduce the fuel consumption with a hybrid propulsion system. The Specific Fuel Oil Consumption (SFOC) of a diesel engine is high at low load. With a hybrid system, the diesel generators can take the load of the propeller and run more efficiently than by using the main engine. Another advantage is that the main engine can take the load of the auxiliary systems to operate at a more efficient load, reducing the number of auxiliary engines running.

The architecture of a typical hybrid propulsion system is illustrated in Figure 2.3a. The main engine(1) is connected to a gearbox(3). On the same gearbox, a electrical motor/generator is connected to either supply power to the propeller or to supply power to the AC electrical network for the auxiliary systems.



(a) Typical hybrid propulsion system (Geertsma et al. 2017)



(b) Typical mechanical propulsion system (Geertsma et al. 2017)

Figure 2.3: Different propulsion systems

2.2.4 Electrical propulsion system

The electric propulsion system does not have any main engine to supply power to the propulsion. Instead, a set of diesel generators(1) supply power to the AC electrical network. The diesel generators have to run at a fixed speed to obtain the required frequency for AC electrical network. All the loads like propulsion motors(5), auxiliary loads, and motors(6) are connected to

the AC electrical network. The voltage and frequency for the different loads are regulated by transformers(3) and frequency converters(4) to obtain the required operating parameters for the different loads. To optimize the efficiency of the system, the number of diesel generators running can be controlled, depended on the load required, resulting in each engine running on optimal load. The architecture of a typical electrical propulsion system is illustrated in Figure 2.4a.

Electric propulsion is a fuel-efficient propulsion solution when the hotel load is a significant fraction of the propulsion power requirement, and the operating profile is diverse because the generator power can be used for both propulsion through the electric motors and auxiliary systems. To achieve this, a Power Management System (PMS) matches the amount of running engines with the required combined propulsion and hotel load power. This control strategy ensures engines do not run inefficiently in part load and is often referred to as the power station concept (Geertsma et al. 2017).

2.2.5 Electrical propulsion with DC hybrid power supply

Compared to the electrical propulsion system with AC electrical network, where the diesel generators have to run at fixed speed, the diesel generators for an electrical propulsion system with DC power supply can run on variable speed. The advantage of this is that the fuel consumption for engines running at variable speed is lower than for engines running at a fixed speed in part load. The diesel generators are all connected to the DC electrical network through voltage rectifiers, which rectifies the AC voltage produced by the generators to DC. The DC energy source, for example, a battery, is connected to the DC network through a bidirectional DC/DC converter. This converter can either supply power to the DC network or charge the battery with excessive power from the diesel generators. To obtain the required frequency and voltage for the loads, power electronic devices like DC/AC converter are used. The advantage of having a battery package connected to the system is that it can take the peak loads, resulting in a more stable operation of the diesel generators. This reduces fuel consumption. The architecture of a typical electrical propulsion system with DC hybrid power supply is illustrated in Figure 2.4b.

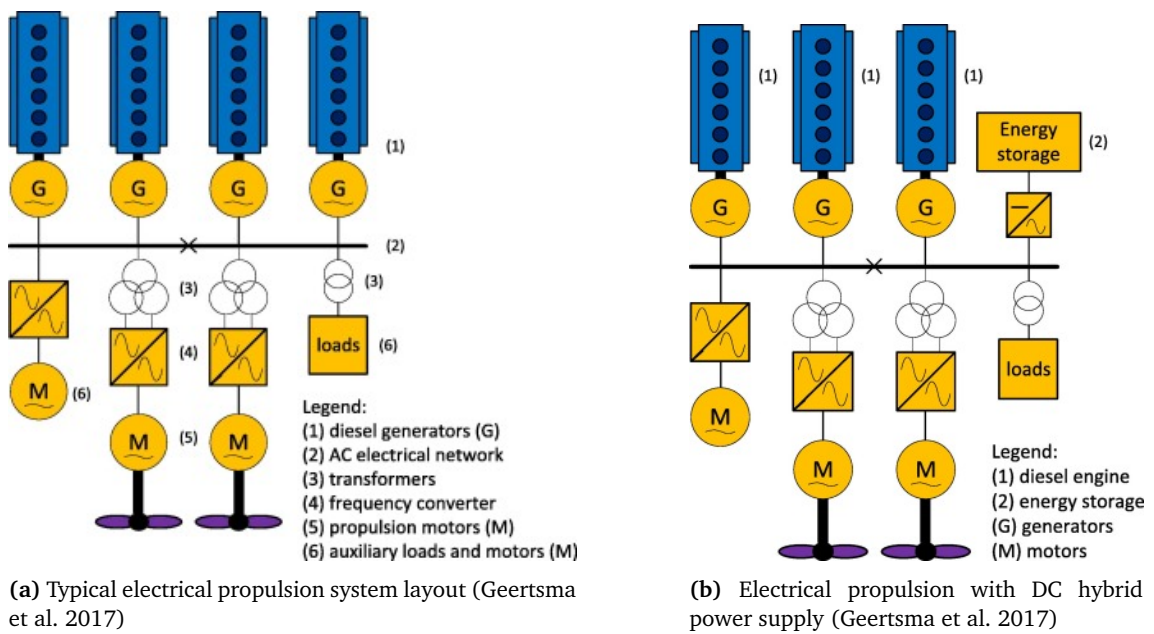


Figure 2.4: Different propulsion systems

Chapter 3

Fault overview

There are many sources of faults resulting in induction motor failure. To separate the different fault types of an induction motor and classify the fault source, a hierarchy is chosen to present this. This chapter explains the sources of the different faults in an induction motor and explains the most common faults and their signatures.

3.1 Classification of faults

The classification of the origin of the faults in an electric motor can be divided in two main levels, the internal and the external source as shown in figure 3.1 Both the internal and external

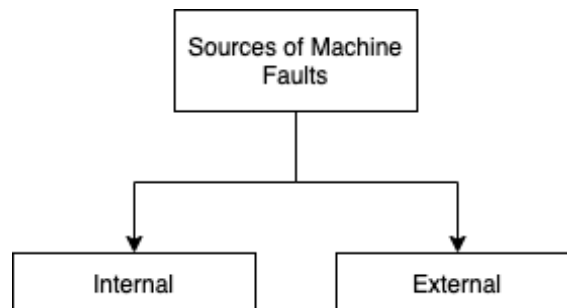


Figure 3.1: Sources of Machinery Faults

sources of fault can be divided into more branches. Figure 3.2 shows that the internal fault can be either mechanical or electrical with their associated fault sources. These faults are caused by manufacturing errors or the deterioration of materials over time. Deterioration-related faults are typically bearing faults, broken rotor bar, and stator insulation failure resulting in a short circuit of windings. Manufacturing faults can be eccentric due to misalignment of the rotor or bearing during assembly. In addition, material weakness from production can also cause internal faults to occur. The mechanical faults are coil and lamination movement, bearing faults, rotor faults, and eccentricity. Several of these faults are related, like bearing faults and eccentricity. If the bearing is loose, this will result in eccentricity faults as well. Coil and lamination movement will result in non-symmetrical operation and can lead to bearing faults and, again,

eccentricity. Rotor strikes occur when the rotor comes in contact with the stator, which is related to eccentricity fault. The electrical failures are dielectric failures, rotor bar crack, and magnetic circuit failure. The dielectric failure is a common term for different internal short circuit faults in the motor. The electrical faults are a result of material degradation over time due to high temperature and high forces. The external fault can either be mechanical, enviro-

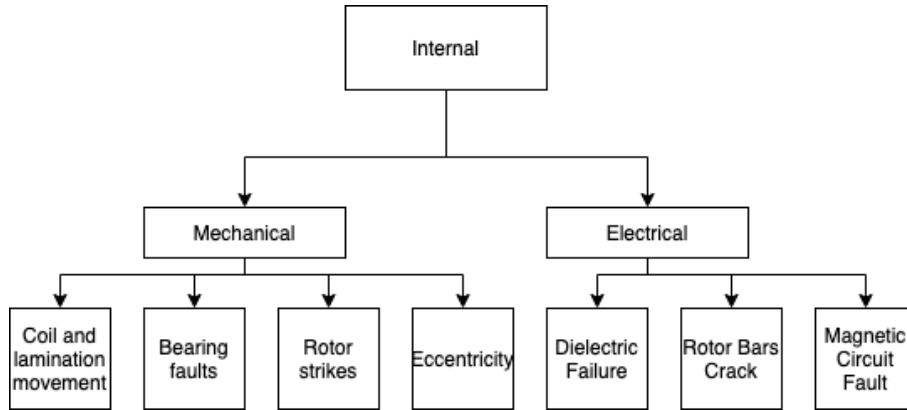


Figure 3.2: Schematic diagram of the Internal Faults

onmental, or electrical, as shown in figure 3.3. These faults result from a failure outside the induction motor, which affects the motor’s operation. The mechanical faults are related to the electrical generation’s mechanical source or the power management system, which often contain power electronic switches. The Environmental fault source is related to the environment in which the motor is operating. High humidity, temperature, and dirt contribute to a higher degradation of materials in the motor, resulting in a shorter lifetime and faults occurring more frequently. The external electrical faults are related to the external load and how this affects the motor. Pulsating load result in load variation and high stresses in the motor. Overload will raise the temperature of the motor, resulting in higher material degradation.

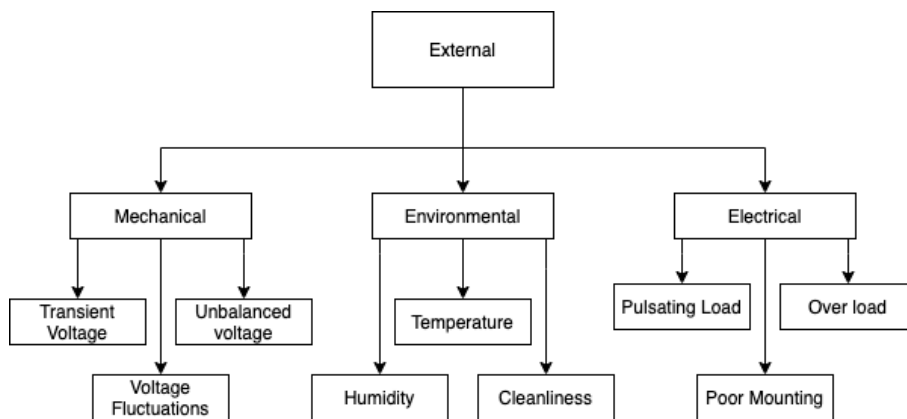


Figure 3.3: Schematic diagram of the External Faults

It is essential to specify the definition of failure in an electrical machine, like how changes in any component of the machine prevent proper operation. It is also possible to define it as the unavailability of an element to perform an intended action. In this sense, the stages of failure are incipience of failure, material fatigue, deterioration, and the fault itself. In the paper *Causes and failures clas-sification of industrial electric motor* (Bazurto et al. 2016) the causes of failures are classified as:

- Inherent weakness of material, design, and manufacturing.
- Misuse or application of efforts in the wrong direction.
- The gradual deterioration as a result of wear, tear, fatigued by stress or corrosion.

The rotor and stator failures can be classified as a combination of several forces acting on each of these components. In table 3.1 a classification of these factors are presented.

Table 3.1: Source fault classification

| | |
|--------|---|
| Stator | Stress thermal (Aging, overload, work cycles) Stress electric (Insulation, corona effect, transient) Stress mechanical (Coil displacement, mechanical rubs) Stress environmental (Pollution, moisture, abrasion, foreign objects.) |
| Rotor | Stress electromagnetic Stress residual Stress dynamic Stress mechanical Stress environmental |

It is challenging to obtain failure statistics of large induction motors as a large part of such statistical data goes unpublished due to confidentiality maintained by the operators. However, for smaller induction motors, such statistical data exist publicly. In the paper *Causes and failures classification of industrial electric motor* (Bazurto et al. 2016), a survey performed at the main centers of repair of electrical machines of Valle del Cauca, Colombia is presented. The survey sample was taken from the repair centers database from January to June 2016. Approximately 500 electric motors were analyzed in this period. The motor power ranged between 1 to 300 HP. The results are presented in figure 3.4 and figure 3.5 below. The paper concludes that the mechanical component is the most significant part of electric motors. As such, the mechanical faults are the most common in electrical motors, as shown in figure 3.4. As shown in figure 3.5a, short circuit faults are the most common electrical fault presented in the paper. For the mechanical faults in figure 3.5b, the majority of the faults are unspecified.

3.2 Fault types

So far, the sources of the failures in an induction motor have been presented. This section will focus on the resulting faults that can occur in an induction motor. For an induction motor, the region of fault occurrence are primarily put under five types.

- Stator fault

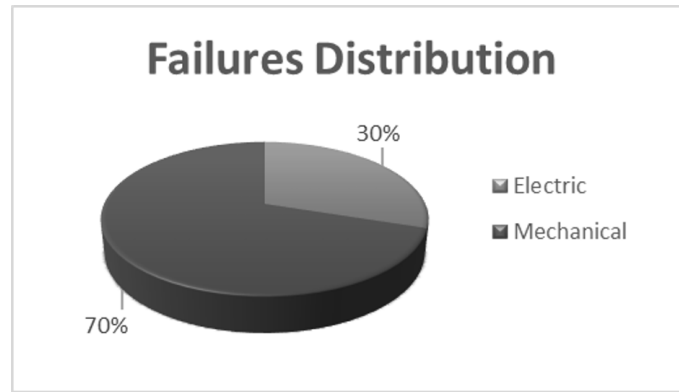


Figure 3.4: Results failure distribution (Bazurto et al. 2016)

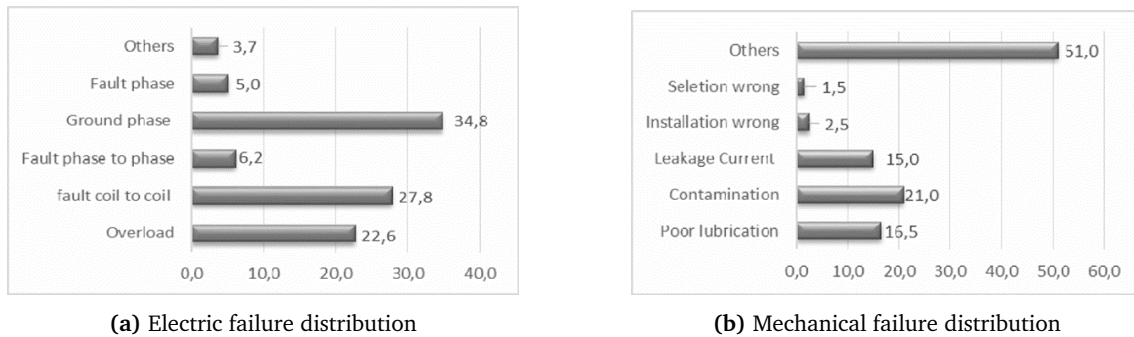


Figure 3.5: Failure distribution in induction motors (Bazurto et al. 2016)

- Rotor fault
- Air-gap irregularities - Static and/or dynamic
- Dynamic eccentricity
- Gearbox and bearing fault

From the faults mentioned above, bearing faults, stator faults, rotor broken bar faults, and eccentricity faults are the most critical faults, and thus more attention is required for these types of fault (Dash et al. 2016). In *Air-gap eccentricity fault diagnosis and estimation in induction motors using unscented Kalman filter* (Bagheri et al. 2020), an overview of the different faults and their fault percentage is presented and shown in Figure 3.6.

3.2.1 Stator faults

There exist several types of stator faults. The fault can be inter-turn, coil-to-coil, phase-to-phase, or phase-to-ground short circuit fault and is usually related to insulation failure. The paper *Online Detection of Induction Motor's Stator Winding Short-Circuit Faults* (Eftekhari et al. 2014) present that according to the Motor Reliability Working Group of the IEEE Industry Applications Society (IAS) and the Electric Power Research Institute (EPRI), stator faults are responsible for 26%–36% of the induction motor failures. Since a stator turn-to-turn fault is

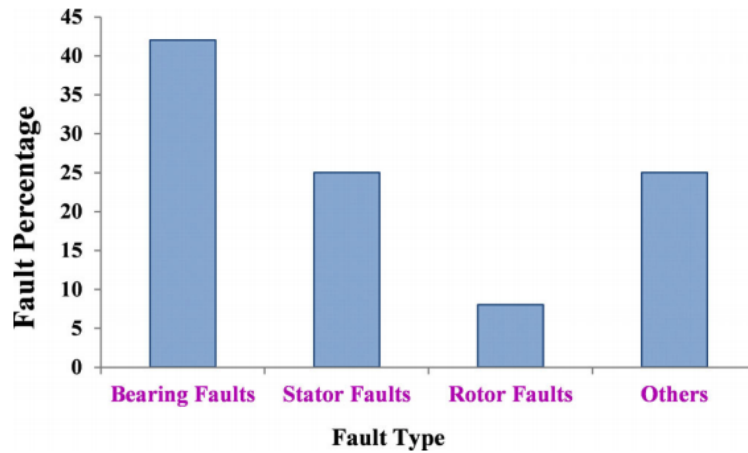


Figure 3.6: Proportion of bearing fault in mechanical faults of motor (Bagheri et al. 2020)

widely believed to represent the incipient stage of most motor winding failures, the detection of a stator turn-to-turn fault has drawn much attention since the early 80's (Zhang et al. 2011). Such a fault produces high currents and winding overheating, resulting in severe turn-to-turn, phase-to-phase, or phase-to-ground faults, as shown in figure 3.7. All these may lead to irreversible damage in stator windings or the stator core (Eftekhari et al. 2014).

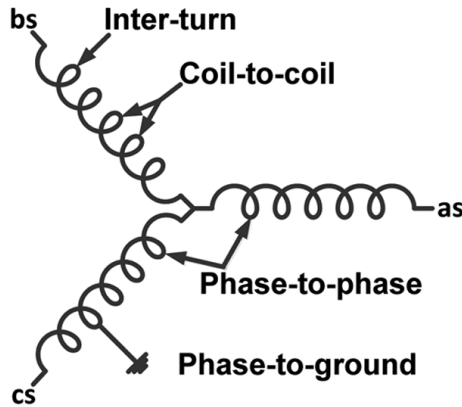


Figure 3.7: Schematic representation of stator possible failure modes (Eftekhari et al. 2014)

3.2.2 Rotor Faults

Rotor faults are electrical failures relating to a bar defect, bar breakage, or mechanical failures such as bearing failure. In large motors, during transient start-up operation, the bar defect develops from thermal stresses, hot spots, or fatigue stresses (Dash et al. 2016). During start-up, the rotor current of an induction motor is very high, typically 5 to 6 times rated current (Supangat et al. 2005). Torque is changed notably by a broken bar, as the other bars must

carry the current of the broken bar (RELJIC et al. 2016). This state is harmful to the steady operation and safety of electric machines (Dash et al. 2016). An illustration of a broken rotor bar is shown in figure 3.8.

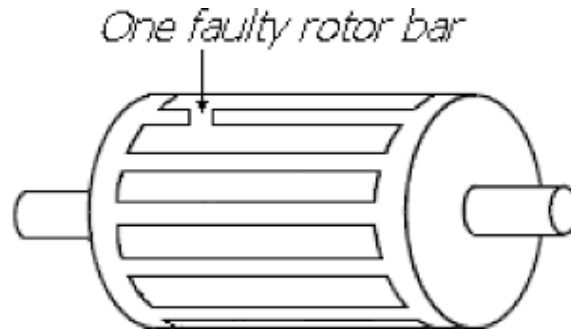


Figure 3.8: Illustration of broken rotor bar (Glowacz 2016)

3.2.3 Effect of rotor unbalance and eccentricity

Statistics show that 80% of mechanical faults are due to eccentricity in induction motors, promoting many research efforts still devoted to the eccentricity in these motors (Faiz et al. 2006). Electrical and mechanical faults during the operation of the motor can lead to the eccentricity between the rotor and stator. Having the precise distribution of magnetic fields makes it possible to predict the performance characteristics of the motor due to the variations of parameters caused by different faults. The eccentricity of an induction motor can be divided into two main classes, being static and dynamic eccentricity. Mixed eccentricity is used as a third class but is only a combination of the two main classes. Figure 3.9 shows an illustration of the two main classes of eccentricity in addition to the healthy state.

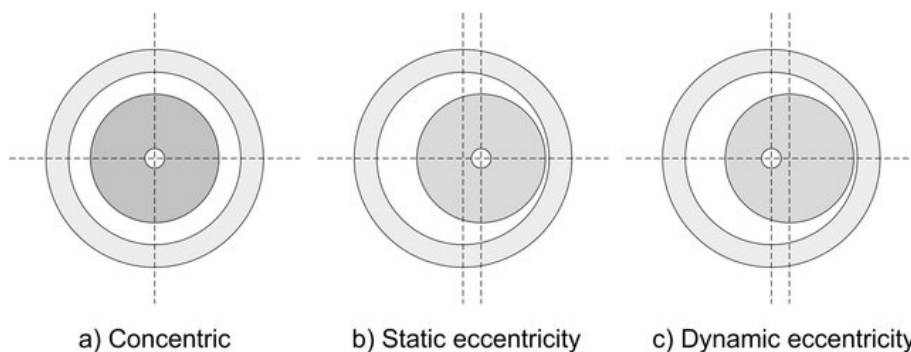


Figure 3.9: Illustration of eccentricity faults (Miljković 2015)

In the case of static eccentricity, the rotational axis of the rotor is identical to its symmetrical axis but has been displayed with respect to the symmetrical stator axis. Although the air gap distribution around the rotor is not uniform, it is time-independent. The reasons for increasing the static eccentricity are the bad position of the stator core due to the mounting of the motor or the non-orientation of the stator and rotor centers during the basic maintenance.

In dynamic eccentricity, the minimum air gap length depends on the rotor's angular position, and it rotates around the rotor. This may be due to misalignment or curvature of the rotor axis. Meanwhile, the static eccentricity generates an asymmetrical magnetic pull, which results in dynamic eccentricity. With this type of eccentricity, the symmetry axis of the stator and rotation axis of the rotor is identical, but the rotor symmetry axis has been displaced. In such a case, the air gap around the rotor is non-uniform and time-varying. This misalignment can be caused by several factors such as a bent rotor shaft, bearing wear or misalignment, mechanical resonance at critical speed, etc.

If there are both static and dynamic eccentricities present, the eccentricity is called a mixed eccentricity. In this case, the symmetry axis of the rotor and stator and the rotation axis of the rotor is displaced. This is the result of the application of the resultant vector of static and dynamic transfer vectors (Faiz et al. 2006).

3.2.4 Bearing Faults

This section describes the characteristic frequencies of the journal and roller bearings with regard to fault detection. Bearing faults in the induction motor studied in this thesis are not modelled, but the literature is presented to get an overview of the most common faults in an induction motor.

Journal bearings

In journal and sleeve bearings, the shaft is supported by an oil film which is "pumped" by the motion of the rotating shaft, creating a space between the bearing liner and shaft as illustrated in figure 3.10. Because of the limited flexibility and oil film compliance, vibration measured at the bearing housing will be small. By using shaft proximeters, the displacement of the shaft inside the bearing can be measured but are only useful at lower frequencies. In journal bearings, the onset of instability in the oil film causes an oil whirl and a subsequent oil whip. The oil film circulates at speed near half of the shaft speed, but because of the pressure difference on either side of the minimum clearance point, the shaft precesses at just below the half-speed described by equation 3.1 (Tavner et al. 2008).

$$\omega_{sm} = (0.43 \text{ to } 0.48)\omega_m \quad (3.1)$$

Journal, plain and tilted pad bearings have infinite life, provided adequate lubrication to support the oil wedge on which the shaft rotates. The shaft performance is normally monitored by two orthogonally positioned eddy current probe transducers that measure the relative displacement between shaft and bearing block. Displacement warning alarms will indicate the need for possible shaft balancing procedures. The bearing condition is best assessed by sump oil analysis, which confirms excessive metal wear (Mais 2002).

Roller bearings

The most common failure mode in induction motors is bearing faults, which represent 40-45% of failures in large industrial motors. Most industrial induction motors operate under stress and

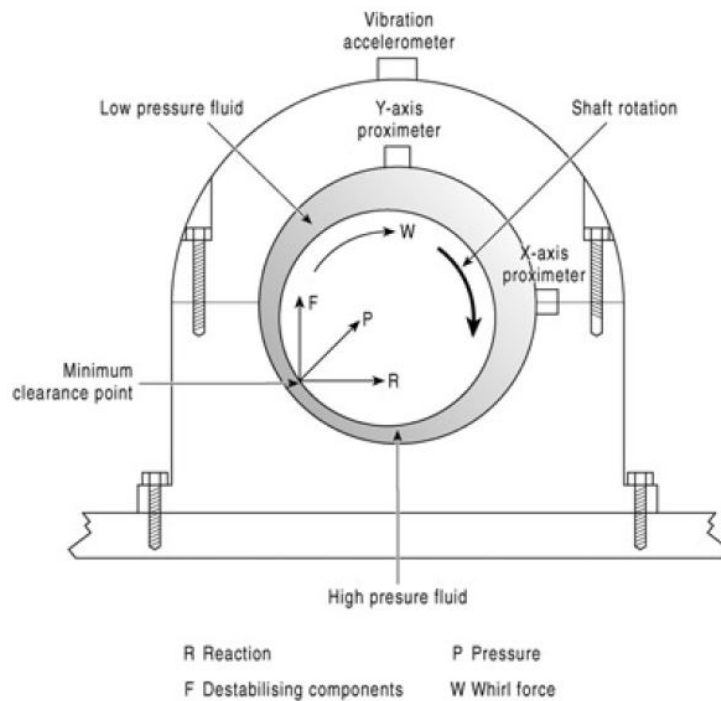


Figure 3.10: Sleeve bearing and Forces acting on a shaft (Tavner et al. 2008)

are subject to local vibrations, fatigue, overloading, misalignment, current distortion, corrosive environment, and insufficient lubrication. In addition, minor defects in the bearing can progress over time and damage the inner race, outer race, and rolling elements, as shown in Figure 3.11. Thereby, bearing failures are not sudden events. Generally, they are progressive with time, cause an increase in motor vibration, and lead to an unscheduled stop or motor breakdown. That is why bearing condition monitoring is an important method to improve the machine reliability (Gonçalves et al. 2015).

Consider a roller bearing where the outer race is flawed due to any of the failure mechanisms. Every time the roller rotate over the flaw, impulsive force is incurred, resulting in the bearing vibrating. The excitation and response in a bearing occur every time a roller rotate over the flaw, generating a specific frequency. This frequency is of interest in the fault detection of bearings, and it can be predicted from the bearing geometry and the speeds at which the inner and outer races rotate. This technique is applicable for faults in other components of the bearings as well. The different characteristic frequencies of a roller bearing is listed below.

- F_{ord} – Frequency Outer Race Defect
- F_{ird} – Frequency Inner Race Defect
- F_{bd} – Frequency Ball Defect
- F_c – Frequency Cage

In the litteratureShrivastava and Wadhvani 2012, these frequencies are often presented as:

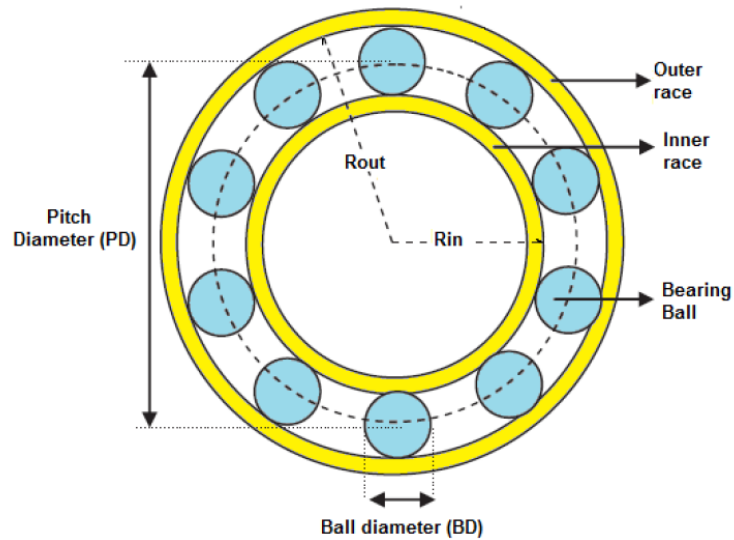


Figure 3.11: Bearing components and main dimensions (Gonçalves et al. 2015)

- BPFO – Ball Pass Frequency Outer Race
- BPFi – Ball Pass Frequency Inner Race
- BSF – Ball Spin Frequency
- FTF – Fundamental Train Frequency

By definition, the ball defect frequency is twice the ball spin frequency, as the ball defect hits the inner and outer race during one rotation. The correlation of the above frequencies is presented in the list below.

- $F_{ord} = \text{BPFO}$
- $F_{ird} = \text{BPFi}$
- $F_{bd} = 2 \cdot \text{BSF}$
- $F_c = \text{FTF}$

The characteristic frequencies of an angular ball bearing in which the inner cage rotates and the outer is stationary Shrivastava and Wadhwani 2012 are:

Ball spin frequency

If a roller or Ball has a defect on the surface, such as a pit, the pulse repetition rate occur each time the defect is struck, is given by the following equation

$$BSF = \frac{N}{60} * \frac{D}{d} * \left(1 - \left(\frac{d}{D} \cos \phi \right)^2 \right) \quad (3.2)$$

Ball pass frequency inner race

If the inner race of the bearing has a defect such as a crack, the fundamental frequency of the vibration resulting from a ball rolling over the defect is called Ball pass inner race frequency and is obtained from

$$BPFI = \left(\frac{N}{60} * \frac{n}{2} \right) * \left(1 + \frac{d}{D} \cos \phi \right) \quad (3.3)$$

Ball pass frequency outer race

Similar to the BPFI, if the inner race has a defect, the fundamental frequency of the vibration is called ball pass outer race and is obtained from

$$BPFO = \left(\frac{N}{60} * \frac{n}{2} \right) * \left(1 - \frac{d}{D} \cos \phi \right) \quad (3.4)$$

Fundamental train frequency

For a defect in the bearing cage, the fundamental train frequency is given by

$$FTF = \left(\frac{N}{60} * \frac{1}{2} \right) * \left(1 - \frac{d}{D} \cos \phi \right) \quad (3.5)$$

where N is the shaft rotation in RPM, d is the ball diameter, D is the pitch angle, n is the number of balls in the bearing and ϕ is the contact angle.

3.3 Fault signatures

Each fault has its distinctive signature, based on how the fault interacts with the induction motor's operation. This is presented as to how the faults affect the current spectrum of the stator current. This section presents the signature of each fault analyzed further in this thesis to get an overview of what to look for when conducting fault detection.

3.3.1 Stator fault characteristics

Consequence

Inter Turn Short Circuit (ITSC) faults will lead to asymmetrical operation of the induction motor and are harmful to the industrial application and safety of operation people. When the fault occurs, harmonics in the air gap flux, torque ripple, and changes in stator current will increase with the degree of short-circuited turns in the faulty winding. As the severity of the fault is increasing with the number of short-circuited turns, detection at an early stage is essential. In addition, when the motor is operating in an asymmetrical state, additional stresses in other components in the system will occur. They will lead to a reduced lifetime of the induction motor as a whole (Chen et al. 2019).

Physics

When inter-turn short circuit fault occurs, a new series of MMF waves will be induced, which can be expressed by equation 3.6 below (Joksimovic and Penman 2000).

$$F_{\text{add}}(t, \theta) = \sum_{\substack{k=-\infty \\ k \neq 0}}^{\infty} F_{\text{add } k} \cos(\omega_1 t - k\theta) \quad (3.6)$$

Equation 3.6 above show that it exists MMF and flux-density waves at all number of pole pairs and in both directions of rotation. One of these waves has the same number of pole pairs as the basic flux-density wave in the machine but with an opposite direction of rotation. This wave induces only base frequency components and will not influence the stator current spectra. As shown in section 2.1, all other waves only induce EMFs and generate currents at rotor slot harmonic frequencies. As a result, no new frequency components appear in the stator current spectra in the presence of stator winding short circuit. The only effect the fault has on the current spectrum is a rise in the rotor slot harmonic frequency can be expected. There are two reasons for this: Firstly, under fault conditions, a greater number of flux-density waves exist in the machine, and all of these frequencies contribute at the same frequencies. Secondly, there is a greater probability of flux-density waves with the basic number pole pairs now existing (Joksimovic and Penman 2000). As described in section 2.1, the rise of rotor slot harmonic frequencies will appear at the following frequencies: $(1 \pm \lambda n(1-s)/p)f_1, \lambda = 1, 2, 3 \dots$

3.3.2 Broken rotor bar characteristics

Consequence

Broken rotor bar faults in an induction motor can lead to unwanted secondary effects like torque and speed oscillation that provoke premature wear of bearings. In addition, rotor unbalance can occur that causes high motor vibration and rotor eccentricity, resulting in the rotor may rub against the stator. Another aspect is that healthy rotor bars in the vicinity of the broken rotor bar are carrying additional current. This leads to asymmetrical overheating of the rotor cage that can cause rotor thermal bending and further fault propagation (RELJIC et al. 2016).

Physics

As explained in section 2.1, when the stator windings are supplied by a balanced three-phase sinusoidal voltage, a forward-rotating magnetic field in the air gap occurs. This field rotates at the same speed as the stator supply frequency f_s . When assuming that the rotor cage is ideal, the slip-dependent EMFs induced in the rotor bar by the stators rotating field are of equal amplitude but a different phase. Therefore, the currents in the rotor bars are of equal amplitudes as well. The frequency of bar currents is $s \cdot f_s$. If breakage of a rotor bar occurs, the bar currents will have different amplitudes and distributions. This results in an electrical asymmetry of the rotor cage. This asymmetry is reflected in the rotor's backward-rotating magnetic field. With respect to the stator, this backward-rotating magnetic field rotates at frequency f_{lsb} as shown in equation 3.7 below (RELJIC et al. 2016):

$$f_{lsb} = -s \cdot f_s + (1-s) \cdot f_s = (1-2s) \cdot f_s \quad (3.7)$$

As a result of this, EMFs of the frequency f_{lsb} are induced in the stator windings. Now, the stator current consist of an additional frequency component, f_{lsb} , in addition to the fundamental. This component is usually called the Lower Side Band (LSB) component. Due to a cyclic variation of current, a torque pulsation at twice the slip frequency, $2s \cdot f_s$, occur, in addition to speed oscillation, which is also a function of drive inertia. This speed oscillation can reduce the magnitude of the LSB. In addition, an Upper Side Band (USB) current component appears in the stator windings due to rotor speed oscillation. The frequency of the USB current component f_{usb} is expressed by equation 3.8 below (RELJIC et al. 2016):

$$f_{usb} = (1 + 2s) \cdot f_s \quad (3.8)$$

These two frequency components are called classical twice slip frequency side-bands due to broken rotor bars. Generally, these broken bar current side-bands are only caused by rotor asymmetry and rotor speed oscillations. Due to imperfection in the construction of the motor, healthy induction motors always have some degree of rotor asymmetry. The side-band current components from broken rotor bar represented by frequencies f_{lsb} and f_{usb} and their interaction flux lines and speed ripple result in additional side-band current components at frequencies $(1 \pm 2ks) \cdot f_s$, where k is an integer(1, 2, 3, ...) (RELJIC et al. 2016).

3.3.3 Eccentricity fault characteristics

Static eccentricity

The flux density components in the presence of static eccentricity can be expressed as in equation 3.9

$$B_{se} = \sum_{n=1,2,3,\dots}^{\infty} A_n \cos \{n(x')\}_{k_s=0,1,2,3,\dots}^{\infty} P_{k_s}^S \cos \{k_s(x)\} \quad (3.9)$$

With p as the number of fundamental pole pairs and $x = x' + \omega_r t$, where ω_r is the rotor speed, equation 3.9 can be expanded into those related to the modified average and static eccentricity permeance component as shown in equation 3.10 below.

$$\begin{aligned} B_{se} = P_0^S & \sum_{n=1,2,3,\dots}^{\infty} A_n \cos \left\{ nx - \left(\frac{n}{p} \right) p \omega_r t \right\} \\ & + \sum_{k_s=1,2,3,\dots} \frac{A_n P_{k_s}^S}{2} \left[\cos \left\{ (n + k_s) x - \left(\frac{n}{p} \right) p \omega_r t \right\} \right] \\ & + \sum_{k_s=1,2,3,\dots} \frac{A_n P_{k_s}^S}{2} \left[\cos \left\{ (n - k_s) x - \left(\frac{n}{p} \right) p \omega_r t \right\} \right]. \end{aligned} \quad (3.10)$$

From equation 3.10, it is clear that only existing components, given by

$$f_e = \left(\frac{n}{p} \right) p f_r, \quad f_r = \frac{\omega_r}{2\pi} \quad (3.11)$$

will be influenced by the presence of static eccentricity (Nandi et al. 2011).

Dynamic eccentricity

The flux density components in the presence of dynamic eccentricity can be expressed by equation 3.12 below.

$$B_{de} = \sum_{n=1,2,3,\dots}^{\infty} A_n \cos \{n(x')\} \sum_{k_d=0,1,2,3,\dots}^{\infty} P_{k_d}^d \cos \{k_d(x')\} \quad (3.12)$$

The same way as equation 3.10, equation 3.12 can be rewritten as

$$\begin{aligned} B_{de} = & P_0^d \sum_{n=1,2,3,\dots}^{\infty} A_n \cos \left\{ nx - \left(\frac{n}{p} \right) p \omega_r t \right\} \\ & + \sum_{k_d=1,2,3,\dots}^{\infty} \frac{A_n P_{k_d}^d}{2} \\ & \times \left[\cos \left\{ (n + k_d) x - \left(\frac{n + k_d}{p} \right) p \omega_r t \right\} \right] \\ & + \sum_{k_s=1,2,3,\dots}^{\infty} \frac{A_n P_{k_d}^d}{2} \\ & \times \left[\cos \left\{ (n - k_d) x - \left(\frac{n - k_d}{p} \right) p \omega_r t \right\} \right] \end{aligned} \quad (3.13)$$

From equation 3.13, it is clear that new components given by

$$f_e = \left(\frac{n \pm k_d}{p} \right) p f_r \quad (3.14)$$

will be introduced. Depending on the values of n and k_d , some components may be the same as those expressed by equation 3.11. However, line to line voltage harmonics that only correspond to those components associated with a pole pair number matching that of a three phase winding will be seen (Nandi et al. 2011).

Chapter 4

Condition Monitoring and Fault Detection

This chapter gives an overview of the concept of condition monitoring, its application in the marine industry, and how it is performed.

4.1 Introduction

Maintenance can be classified into two main types and management categories, being planned and unplanned maintenance. Planned maintenance can further be divided into two types of strategies. Preventive maintenance aims to prevent a failure from occurring, either by doing periodic overhauls or by continuous condition monitoring of the equipment. Corrective maintenance is a strategy where the equipment runs until failure. This is typically used for equipment not critical for safety or availability. This paper will focus on condition-based maintenance. This strategy is based on inspection and measurement of equipment parameters to be able to decide whether it is in a satisfactory condition or not. The process requires that the equipment is continuously or periodically evaluated and compared to acceptable operational limits. This is also referred to as condition monitoring and fault detection. Fault detection is defined as the "determination of faults present in a system and time of detection," while faults are defined as "unpermitted deviation of at least one characteristic property or variable of the system" (Isermann and Ballé 1997).

4.2 Overview of prognosis and health management

Predictive maintenance is a maintenance strategy that recommends maintenance actions based on the information collected through condition monitoring. The maintenance strategy is often called Condition Based Maintenance (CMB) for this reason. The degradation trend of the rotating machinery in this strategy is first revealed through the analysis of condition monitoring data. The degradation trend in the future is then predicted using some prediction models or techniques. With a failure threshold that is pre-specified, the Remaining Useful Life (RUL) of the rotating machinery can be predicted. Based on the predicted RUL, maintenance can

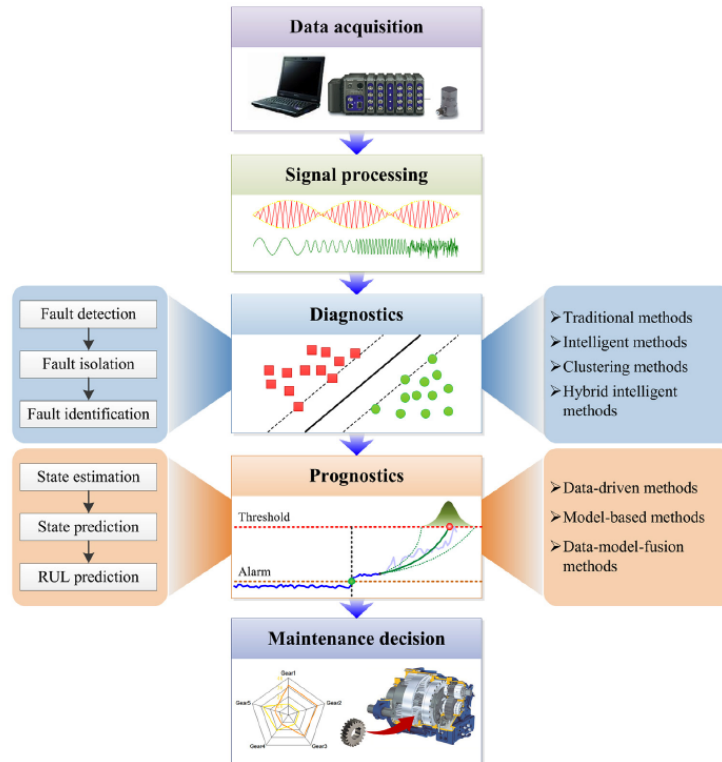


Figure 4.1: Flowchart of the PHM of rotating machinery (Lei 2017)

be scheduled with an optimal maintenance strategy before the real occurrence of the final failure. The predictive maintenance strategy has evident advantages compared with either reactive or preventive maintenance. It has proven able to predict the potential breakdown of a machine through regular condition monitoring before the failure occurs, thus preventing the machine's potential total failure. In addition, the maintenance strategy can use the predicted RUL to schedule maintenance at an optimum time, resulting in the machine having a maximum uptime with minimum maintenance cost. This has resulted in predictive maintenance has attracted substantial attention in recent years. Based on predictive maintenance strategy, a new concept of Prognosis and Health Management (PHM) has been developed in recent years (Lei 2017).

The flowchart of the PHM of rotating machinery is shown in Figure 4.1. The concept is generally composed of five major processes, being data acquisition, signal processing, diagnostics, prognosis and maintenance decision.

Fault diagnosis and protection of electrical machines have existed for many years and are an old concept. In the beginning, producers and operators depended on simple and uncomplicated protection methods such as measuring overcurrent, over-voltage, earth faults, etc., to ensure safe and reliable operation (Dash et al. 2016). Monitoring these parameters and actions to protect the electrical machine can only be done as the fault occurs. Over the years, as induction motors got more significant in size and used in large industrial plants and as propulsion

drives for ships, it was essential to diagnose faults at their very inception. The reason is that unscheduled machine downtime in industries and shipping will lead to high financial losses and can even lead to a hazardous event if propulsion is lost.

4.3 Condition monitoring of ship propulsion systems

The International Maritime Organisation (IMO) is an organization created to ensure that relevant conventions and standards related to shipping are up to date and relevant. The principal technical advisor of IMO is the International Association of Classification Societies (IACS), with established minimum requirements aimed at increasing maritime safety and decreasing pollution. The IACS combined these rules into Unified Requirements, which serve as minimum requirements for member societies. Classification societies are independent bodies that confer classification to vessels that are build and operated according to the requirements set by the individual classification society (Nejad et al. 2021).

Maintenance of critical systems onboard ships can increase system reliability and reduce the risks associated with propulsion losses. Maintenance strategies include planned preventive maintenance, condition-based maintenance, unplanned maintenance, or a combination of these methods. Condition-based maintenance uses condition monitoring to determine which maintenance strategy to use. All DNV GL classified ships must have all equipment "properly maintained" according to recognized standards or manufacturer recommendations (DNV-GL 2020a) as a basic requirement. Maintenance is defined to be carried out at defined intervals as part of a maintenance plan. Periodic surveys are mandated in order to confirm satisfactory condition of the machinery, hull, equipment, and systems (DNV-GL 2020b).

DNV GL describe condition monitoring in its rules as follows. Condition monitoring of a ship propulsion system is a survey arrangement based on audits of an approved and implemented condition-based maintenance program on ship's board, allowing the maintenance intervals of various components to be changed based on the monitored data (DNV-GL 2020b). Nevertheless, the audits shall be part of the main class annual survey. In order to offer an alternative to planned based renewal surveys, companies providing condition monitoring services of ship propulsion systems shall be approved by the society . The class program of DNV GL is limited to the following standardized methods (DNV-GL 2016):

- Vibration condition and diagnostics
- Lubricant analysis (oil).

Ship operators are required by the manufacturers of the components and the classification society to maintain their systems on a regular basis. The ship operators work out a maintenance plan with the component manufacturers and the classification societies to meet this requirement. They must take into account the risk of failure, minimization of maintenance costs, and time spent in dry docking, etc. The trend in the industry is moving towards condition monitoring services, where the monitored condition of the component is accounted for in the maintenance plan, and maintenance intervals can be adjusted in a cost- and risk-efficient manner.

4.3.1 State of the art in marine industry

Wärtsilä is a company manufacturing power plants and marine engines. The Wärtsilä Propulsion Condition Monitoring Service (PCMS) is recognized by the classification societies LR, ABS and DNV GL. This recognition eliminates the need to enter a dry dock for visual inspections of the installed machinery. These classification societies have acknowledged that Wärtsilä PCMS can determine the condition of propulsion equipment without internal visual inspections and detect potential failures. This is achieved by measuring vibration and oil condition in order to effectively monitor gears, bearings, the propeller, and other propulsion equipment components. In addition, the service gathers operational parameters from the propulsion control system. At the same time, the data is processed onboard and sent to Wärtsilä. If these data show any issue that requires immediate attention, the operator will be informed. Each month a PCMS report is sent to the customer that outlines the latest findings and recommendations. It also describes the condition of the propulsion equipment, the recommended maintenance interval, and how the equipment can be kept in optimal condition (Wärtsilä 2018). PCMS is applicable to electric pods, steerable thrusters, transverse thrusters, controllable pitch propellers, including reduction gears and water jets. Typical measurements include:

- Vibration
- Lubrication oil contamination
- Lubrication oil-water saturation
- Driveshaft RPM
- E-motor load (for E-driven applications)
- Control system parameters

Condition monitoring services for marine propulsion systems are offered by ABB Ltd, Kongsberg Gruppen ASA, Rolls-Royce Holdings plc, SCHOTTEL GmbH, Siemens AG and ZF Friedrichshafen AG. Information about what the systems measure, how the data is processed, and how these systems are implemented onboard is difficult to access. The description of Wärtsilä's condition monitoring service is freely available and recognized by the major classification societies and reflects the industry's expertise in condition monitoring of marine propulsion systems sufficiently.

4.3.2 Development trend

This section discusses the research and development trend relating to condition-monitoring techniques and methods for marine propulsion systems. It is important to note that most techniques and methods are generic and have also been used in other industries.

Condition monitoring and fault diagnosis of electrical machines has always been a topic of interest and importance in industry and academia. In recent years, there has been extensive research activity in this field towards the development of predictive maintenance systems. This is because electrical machines are increasingly used in new applications and are often a critical part of the system. Electric motors and generators are now utilized in marine propulsion systems to increase energy efficiency and reduce emissions (Nejad et al. 2021)

The most common signals measured for fault diagnosis in electrical machines are vibration and stator current. Vibration analysis is commonly used for condition monitoring and fault

detection in rotating machinery. Frequency analysis of vibration signals can reveal valuable information about the health of the machine and detect different types of faults. These include eccentricities, bearing damage, and short circuit faults. Monitoring the stator current signal for fault diagnosis has attracted a lot of research efforts in the past two decades, as this method, commonly referred to as MCSA, can detect a variety of electrical and mechanical faults. Signal processing techniques and development of Artificial Intelligence (AI)-based algorithms have featured in recent research works dealing with fault detection and classification in electrical machines. A desired fault diagnosis system should be able to detect different types of faults, separate them from each other, and prove functional in non-steady states of operation (Nejad et al. 2021).

4.4 Measurement signals

When conducting fault detection, it is essential to know which signal to monitor. Several parameters of machines can detect fault at different stages. As shown in figure 4.2, changes in vibration are the earliest indication of degradation of a machine. Further, the particles in lubrication is the next step, followed by noise, temperature, and finally excessive heat. Identifying a fault in the incipient stage of the degradation is crucial for maintenance planning and perform preventive measures to avoid further development of the fault. In this section, vibration analysis, motor current analysis, and temperature monitoring will be presented. As an induction motor does not have any lubrication in the system, except in journal bearings, this is not included.

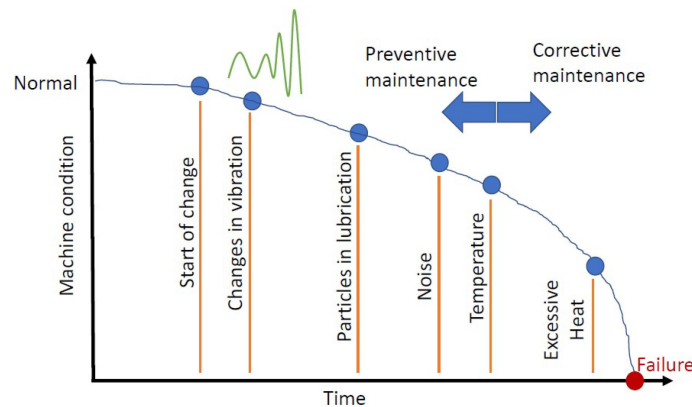


Figure 4.2: Condition monitoring and stages of identification of an incipient failure - overview (Ibrion et al. 2021)

4.4.1 Vibration analysis

Vibrations are produced in every rotating machine by the oscillation of mechanical parts. These oscillations are transferred to the rest of the system, which is coupled with the machine shaft. When a part of the rotating machine wears or breaks, the oscillation changes, and therefore the vibration spectrum will change. In addition, any abnormalities in air gap flux in an induction

| Range of typical zone boundary values for non-rotating parts | | | | |
|--|----------------------------------|---------------------------------|----------------------------------|------|
| r.m.s. vibration velocity mm/s | | | | |
| 0,28 | | | | 0,28 |
| 0,45 | | | | 0,45 |
| 0,71 | | | | 0,71 |
| 1,12 | Zone boundary A/B 0,71 to 4,5 | | | 1,12 |
| 1,8 | | | | 1,8 |
| 2,8 | | Zone boundary B/C 1,8 to 9,3 | | 2,8 |
| 4,5 | | | | 4,5 |
| 7,1 | | | Zone boundary C/D 4,5 to 14,7 | 7,1 |
| 9,3 | | | | 9,3 |
| 11,2 | | | | 11,2 |
| 14,7 | | | | 14,7 |
| 18 | | | | 18 |
| 28 | | | | 28 |
| 45 | | | | 45 |

NOTE 1 This table only applies to machines for which specific International Standards have not been developed and for which there is no suitable experience available.

NOTE 2 Small machines (e.g. electric motors with power up to 15 kW) tend to lie at the lower end of the range and large machines (e.g. prime movers with flexible supports in the direction of measurement) tend to lie at the upper end of the range.

Figure 4.3: Range of typical values for zone boundaries (ISO 2016)

motor change the torque and hence changing the vibration pattern. The vibration monitoring technique utilizes that each fault in a rotating machine produces vibrations with distinctive characteristic frequencies. By measuring these and comparing them with the reference once, fault detection and diagnosis can be performed (Shrivastava and Wadhvani 2012). ISO 13373 (ISO 2002) part 1 to 3 promotes the use of well-accepted guidelines for acquiring and evaluating vibration measurements for condition monitoring. Vibration measurements for condition monitoring can be done in many ways, from the very simple to the very complex, and can include continuous or periodic measurements. However, they all share the common goal of accurately and reliably assessing the condition of a system. The instrumentation and procedures recommended in this part of ISO that will assist in achieving this goal will be addressed in this section (ISO 2002).

It is possible to evaluate the vibration severity by comparing them to zone boundary layers. This comparison is made with the root mean square values of the mm/s velocities of the real time-series data of the vibration, and the zones are found in ISO Standard ISO20816-1 (ISO 2016) and described as:

- **Zone A:** The vibration of newly commissioned machines normally falls within this zone.
- **Zone B:** Machines with vibration within this zone are normally considered acceptable for unrestricted long-term operation.
- **Zone C:** Machines with vibration within this zone are normally considered unsatisfactory for long-term continuous operation. Generally, the machine may be operated for a limited period in this condition until a suitable opportunity arises for remedial action.
- **Zone D:** Vibration values within this zone are normally considered to be of sufficient severity to damage the machine.

The table showing the boundary ranges for vibration velocity is shown in Figure 4.3.

4.4.2 Motor current signature analysis

Among the different techniques for fault detection in induction machines, MCSA is one of the most widely used (Cusido et al. 2005). One of the main advantages of MCSA is that it provides sensor-less diagnosis of the rotor and bearing problems (Mortazavizadeh 2014). MCSA uses the spectral analysis of the stator current to identify characteristic fault frequencies. When a fault is present in the motor, the frequency spectrum of the line current becomes different than for the healthy motor. The fault modulates the air gap and produces rotating frequency harmonics in the self and mutual inductance of the machine. It rely on locating specific harmonic components in the stator current. Therefore, it offers significant implementation and economic benefits (Abhinandan and Sidram 2017).

4.4.3 Temperature

Both the rotor and stator temperature are of concern in short-term machine protection and in longer-term condition monitoring for large induction machines. Mainly when operating with overload cycles, it is necessary to monitor rotor bars and stator winding temperatures. This is to make sure that the temperature remains below prescribed limits (Beguenane and Benbouzid 1999).

The paper *Effect of temperature rise on the performance of induction motors* (Khalifa et al. 2010) conclude that the insulation resistance decreases with the increase of the winding temperature, the stator current decreases with the increase of the winding temperature. In addition, the motor's efficiency understudy becomes poor with the increase of winding temperature due to the increase of the motor losses. The unfavorable effect of temperature rise on motor performance is more significant in full-load cases, where the maximum temperature reached, according to the measurements, was 85° C, while in the simulation results, it was 68° C due to the negligence of the environmental conditions.

4.5 Data acquisition

Data acquisition is a process of collecting measurement signals using different kinds of sensors from the monitored asset. The measured signals should contain information that reflect the health conditions of the machines. There are many different types of measurement signals that can be used for this, such as vibration signals, acoustic signals, temperatures, and electric currents. Various sensors have been designed to collect different t types of signals like accelerometers, acoustic emission sensors, infrared thermometers, and ultrasonic sensors, to mention some. The measured signal is usually transmitted into a PC through a Data Acquisition (DAQ) equipment and stored in a memory location for further analysis. With the rapid development of advanced sensor and computer technology, many new data acquisition facilities and techniques have been designed and applied in modern industries. These powerful and adoptable facilities have made data acquisition for PHM implementation more convenient and feasible (Lei 2017).

4.5.1 Location of measurement

The location of transducers for condition monitoring depends on the particular machine and the specific parameter to be measured. Therefore, before specifying the location, it is necessary to identify which parameter should be monitored. The different parameters that can be measured are listed below.

- the absolute vibration of the machine housing
- the vibratory motion of the rotor relative to the housing
- the position of the shaft relative to the housing during machine operation, and
- the absolute motion of the shaft

In general, the transducers should be located at or near the bearings. However, if the experience is available for a particular type of machine and if such transducer locations are practical, it should be useful to locate transducers at other positions than the bearings, as listed below.

1. at the position which is most likely to provide maximum values of vibration (such as intermediate shaft midspan of large gas turbine units);
2. at the position where a small clearance exist between the static and rotating parts and rubbing may occur.

Whatever the plane chosen for the vibration measurement, transducers should be located at those angular positions, which are most likely to provide early indications of wear and failure (ISO 2002).

4.6 Signal processing

Signal processing aims to analyze the stored measurement signals in the data acquisition process using signal processing techniques and methods. The task of signal processing is to extract useful information that can reveal the health conditions of the machinery from the original measurement signals. The different techniques can be roughly classified into the following three categories: time-domain, frequency-domain, and time-frequency-domain analysis. The original measurement signals are generally sampled repeatedly between pre-specified time intervals and in the time domain. The traditional time-domain analysis calculates statistic characteristics describing the health condition of machines, such as peak, root mean square, mean, kurtosis, and skewness. The frequency-domain analysis is based on the transformed signal in the frequency domain. The advantage of frequency-domain analysis over time-domain analysis is that it decomposes the original signal into a series of frequency components. The most commonly used frequency-domain analysis is the spectrum analysis by means of Fast Fourier Transform (FFT). The main idea of spectrum analysis is to locate and isolate specific frequency components related to the fault characteristics of the machines. A limitation of the frequency-domain analysis is that it is only effective in handling stationary measurement signals, and the measurement signals generally present non-stationary characteristics. The time-frequency-domain analysis investigates measurement signals in both the time and frequency domain. The time-frequency analysis describes the characteristics of the measured signals in two-dimensional functions of both time and frequency. A widely used time-frequency-domain analysis tool is Short Time Fourier Transform (STFT), which divides the measured signals into

different segments with short time windows and then applies Fourier transform to each segment (Lei 2017).

4.6.1 Fast Fourier Transform

Signal processing in the frequency domain is based on Fourier Transform (FT), which transforms a time-domain signal into a frequency spectrum. This is done to analyze the signal characteristics in the frequency domain. The principle of FT is to first divide a periodical signal into a summation of several sinusoidal components by virtues of the Fourier series. Then, the frequency spectrum of the periodic signal can be obtained by the projection of these sin and cosine signals in the frequency axis as illustrated in figure 4.4. However, by the nature of the FFT, it is only suitable for stationary signals, as it only converts the signal to the frequency domain. This means that it can not show when a specific frequency occurs in the time domain. FT consists mainly of four essential parts, being Fourier series, Fourier integral, Discrete Fourier Transform (DFT) and FFT (Lei 2017). FFT is an efficient version of the DFT algorithm with respect to computation that greatly reduces the necessary number of computations (Miljković 2015). This thesis will focus on the FFT analysis of the measured signals of the induction motor.

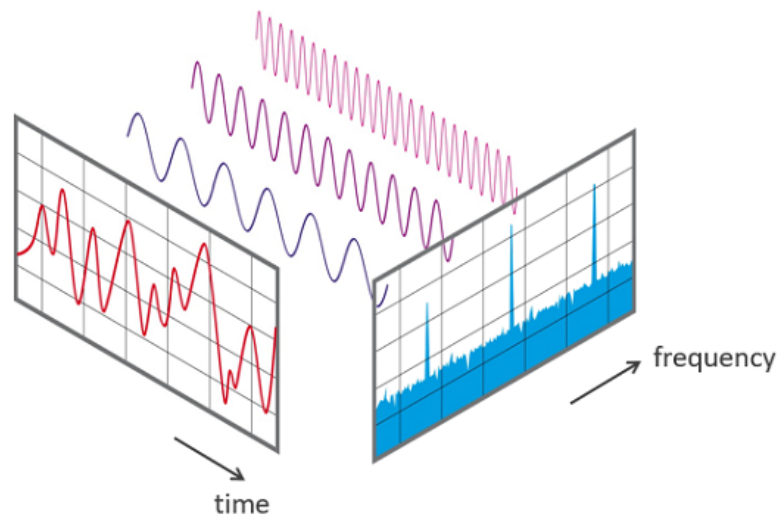


Figure 4.4: Visual illustration of FFT (UiO 2019)

4.6.2 STFT

Since FFT analysis is restricted to stationary signals, it is not suited to process faulty signals which are non-stationary. Moreover, as mentioned above, the frequency spectrum acquired by FFT cannot reflect the changes in each frequency with time. To overcome this challenge, time-frequency analysis techniques are developed to analyze non-stationary signals. Up to now, classical time-frequency analysis techniques mainly include STFT, Wavelet Transform, Hilbert-Huang Transform (HHT), etc. (Lei 2017). The principle of STFT is to divide the signal into

smaller pieces in the time domain, performing FFT on the short signal, and finally add up all the FFT for the signal. This results in a time-frequency analysis where the different amplitudes can be separated in time. An illustration of the STFT is shown in figure 4.5

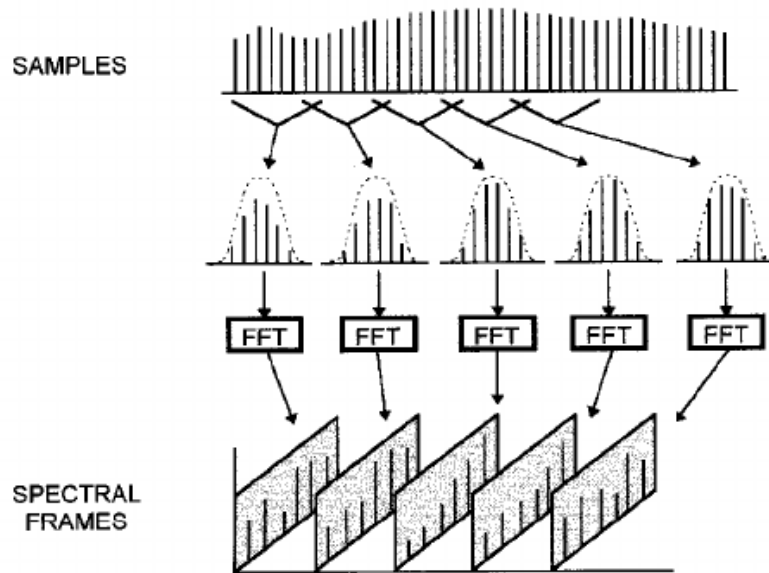


Figure 4.5: Visual illustration of STFT (Fischman 1997)

4.7 State of the art: Induction motor fault detection

In recent years, much attention has been put into condition monitoring and fault detection of industrial induction motors.

In the paper *Electromagnetic Analysis and Electrical Signature-Based Detection of Rotor Inter-Turn Faults in Salient-Pole Synchronous Machine* (Valavi et al. 2018), investigation of rotor inter-turn faults in salient-pole synchronous machines are conducted using finite-element analysis. The machine in the study is a 22 MVA eight-pole hydropower generator with fractional-slot windings. Furthermore, this paper investigates the online detection of inter-turn faults using spectral analysis of stator voltage or current. This paper also discusses the effects of parallel circuits in stator windings. In addition, a comparison between fault-related harmonics in the case of dynamic eccentricity and rotor inter-turn faults is presented.

Another paper investigating the use of FEA for condition monitoring is *Induction machine model with finite element accuracy for condition monitoring running in real-time using hardware in the loop system* (Sapena-Bano et al. 2019). What is proposed in this paper is to apply the sparse subspace learning in combination with the hierarchical Lagrangian interpolation to obtain the parametric solutions of the faulty IM model that cover the whole range of severity of a given fault, with a reduced number of FEA simulations. Utilizing this approach, it is possible to boost the computation speed and achieve a significant reduction of memory requirements while

retaining reasonable accuracy compared to traditional FEA, enabling the real-time simulation of predictive models.

The most relevant paper found in the literature is *Fault Analysis of Induction Machine using Finite Element Method* (Zaabi et al. 2014) The paper presents a finite element-based analysis procedure for an induction machine. Based on finite element models, the paper studies the influence of the stator and the rotor faults on the behavior of the IM. A simple dynamic model for an IM with an inter-turn winding fault and a broken bar fault is presented in the study. This fault model is used to study the IM under various fault conditions and severity. The comparison of the results obtained by simulation tests allowed verifying the precision of the proposed FEM model. The paper presents a technical method based on FFT analysis of stator current and electromagnetic torque to detect the faults of the broken rotor bar. The simulation results obtained show clearly the possibility of extracting signatures to detect and locate faults. The main differences between the work done in (Zaabi et al. 2014) and the work done in this thesis, is the difference in size of the motor, different modeling method of the induction motor and different way of modelling the faults.

Chapter 5

FEM modelling

To study the effect of the fault conditions mentioned in section 3.3.1, 3.3.2 and 3.3.3, time-stepping finite element (TSFE) -simulations were performed on a 2D model of an induction motor. The model of the induction motor is created in ANSYS Maxwell software. The model used in this thesis was created as a part of the HealthProp project, by Mostafa Valavi. The model is build based on technical drawings and parameter estimation of the propulsion motor onboard the research vessel SA Agulhaus II. The resulting model is shown in figure 5.1 and its general information is presented in table 5.1. The reason for the motor being modeled in 2D and not 3D is based on reducing computation time for the simulation. This result in the thesis being limited to fault conditions which are symmetrical in axial direction, making the 2D model the preferred approach. All the faults, except from one case of dynamic eccentricity is symmetrical in axial direction. This case is when only one side of the rotor is "loose" and is experiencing dynamic eccentricity, and is not evaluated in this thesis. By using finite element method to perform dynamical simulation, more precise results than other models are obtained, as the reel geometry and winding layout of the machine are used.

Table 5.1: General motor parameters

| | |
|-----------------------------|--------|
| Nominal effect | 22MVA |
| Nominal voltage | 2694 V |
| Nominal current | 1385 A |
| Number of phases | 3 |
| Number of rotor bars | 108 |
| Number of coils | 96 |
| Stator winding connection | Star |
| Number of parallel branches | 4 |
| Frequency, f_s | 9,5Hz |
| Outer rotor radius | 1410mm |
| Stator inner diameter | 1420mm |
| Stator outer diameter | 2000mm |

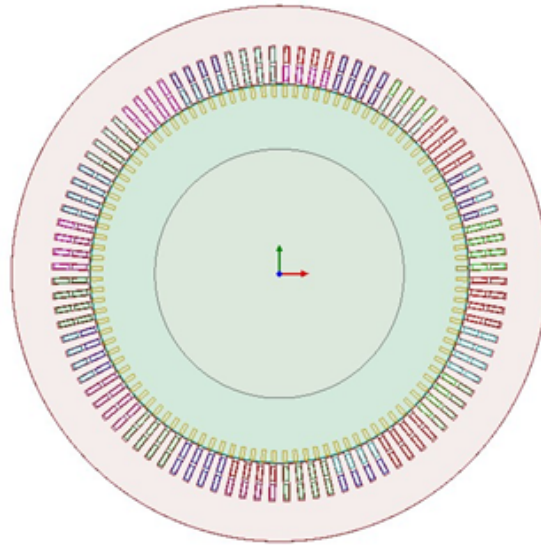


Figure 5.1: Induction motor model in Maxwell

5.1 Modeling of the Healthy Induction Motor

As mentioned above, the healthy induction motor was created as a part of the HealthProp project, by Mostafa Valavi. This section will describe the different components and parameters of the healthy motor.

The stator consists of 96 slots containing the stator windings. The stator windings are modelled as solid rectangles. This is a simplification as the coils in the stator windings consist of several strands. However, the simplification will not influence the amount of current flowing within each winding. This is because the effect of stranded coils was included in the model. Each stator slot contains two rectangles, as the induction motor has a doubled-layered winding layout. The rectangles representing the stator windings were modelled as annealed copper. The insulation and slot wedge are modelled as air, as these have little effect on the induced magnetic field which are of interest in this thesis. The windings are divided by the 3 phases, containing 32 coils each. The motor has 4 pole pairs per phase in addition to 4 parallel branches for each phase. Each coil in the model consists of 9 conductors, representing 9 turns. The effect of parallel branches is described below. The rotor contains 108 rotor bars, short-circuited in the end connection. The rotor bars were modelled as pure copper.

5.1.1 Effect of parallel branches

For large induction motors, it's not uncommon to be equipped with two or more parallel circuits in the stator winding Valavi et al. 2018. In healthy condition, the phase voltage in the parallel windings is equal. When a short circuit occurs in a winding in one of the branches, the resistance in the branch is reduced. The motor studied in this thesis has four parallel branches consisting of eight coils each. An illustration of the parallel circuit of one phase is shown in figure 5.2 below.

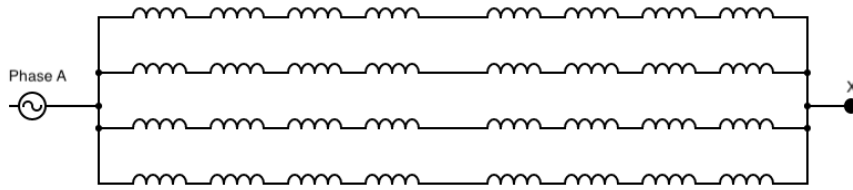


Figure 5.2: Schematic diagram of phase A stator winding

5.1.2 Mesh

Ansys Maxwell is a FEM software, as such it solves the calculations by reducing the problem's geometry into discretized building blocks. The collection of the discretized building blocks is called the mesh. The static algebraic equations of the problem are solved in the connecting points of the building blocks. The values outside the points are interpolated from the neighbouring points. The refinement of the mesh, the number of elements the problem geometry is reduced into, effects both the accuracy and computation time of the simulations. The finer the mesh, the more accurate the results. By increasing the number of points, more calculations have to be performed, resulting in increasing simulation time. Therefore, when deciding the mesh refinement, both the computational time and the accuracy of the simulations were taken into consideration. The refinement of the mesh can be specified for specific areas or components in the model. By doing this, the accuracy of the simulation can be increased in important areas and reduced in less important areas of the geometry, optimizing the computational time without sacrificing the accuracy in important areas.

For the model in this thesis, the length based mesh operation in ANSYS Maxwell was chosen. This gives the opportunity to specify the number of elements and the maximum distance between the points within a selected part of the model. Ansys Maxwell then generates a mesh following these restrictions. A visualisation of the mesh used for the simulations in this thesis are presented in figure 5.3.

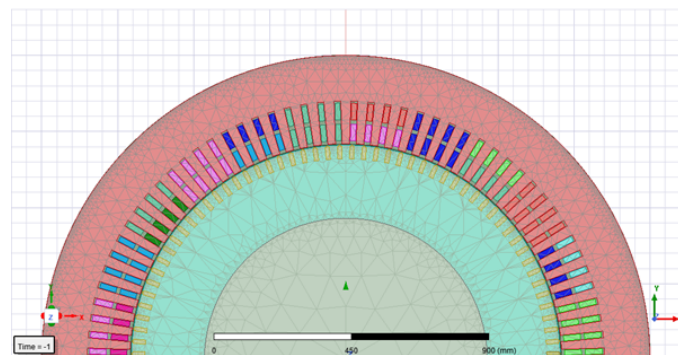


Figure 5.3: Mesh of the whole motor

The area of interest for the simulations, when it comes to accuracy, is the air-gap. The less important parts are the stator and rotor core. The motor was only assigned one specified mesh

operation in the air gap. This was done by specifying the maximum length of each element in the middle band of the motor, being 1mm. The simulations should have an acceptable accuracy in the results, with a moderate simulation time.

STFE analysis is employed for modeling and simulation of the faults in this thesis. Since the simulation results will be used to identify fault-related harmonics, special attention must be paid to the quality of mesh, especially in the air gap, as this is where the the distorted EMF waves are present. In addition, the time step and length of the simulations are important for having sufficient frequency range and frequency resolution respectively. A more detailed view of the air-gap mesh is presented in figure 5.4.

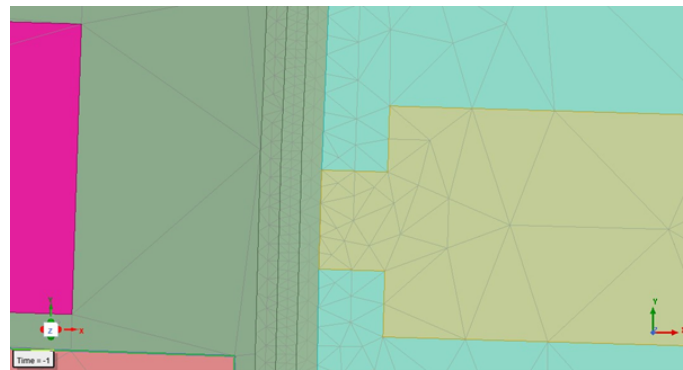


Figure 5.4: Air-gap mesh in Maxwell

5.2 Fault modeling

This section describes how the rotor ITSC, broken rotor bar, static and dynamic eccentricity were modelled. The faults are modelled by modifying the healthy motor described above.

It is important to note that by changing the geometry, as is done when modelling for static, dynamic and mixed eccentricity, the generated mesh will be different from that of the healthy generator. Still, by assigning a 1mm mesh in the air-gap, it gave mesh which was deemed satisfactory for all the simulated cases.

5.2.1 Modelling of inter turn short circuit fault

The inter turn short circuit fault of the stator winding was modelled by reducing the number of conductors in a selected coil. By doing this, the number of turns in the stator coils are reduced and hence simulating a short circuit fault in the stator. When a short circuit fault occur in one of the stator coils, the resistance in that coil is reduced. To include this effect, an external circuit must be made in Maxwell. The external circuit used for ITSC fault modelling is shown in figure 5.5.

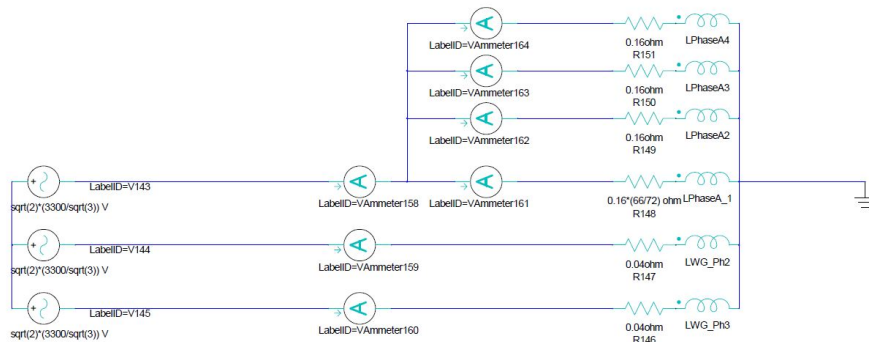


Figure 5.5: The external circuit for inter-turn short circuit fault

Here, the resistance of the branch is reduced by $\frac{66}{72}$ to simulate the resistance of 6 short circuited turns in one of the parallel branches of phase A, where 72 is the total number of turns in the branch.

The resistance value of the branch where the fault is present, depends on the severity of the fault, i.e the number of turns short circuited. The resistance in the branch is reduced linear with the number of short circuited turns, with respect to the total number of turns in the branch.

An example of 6 short circuited turns in two coils is illustrated in figure 5.6. The parameters of the coils are presented in table 5.2 where the number of conductors in two coils are reduced from 9 to 3.

The parameters and calculation of the characteristic frequencies for ITSC as described in section 3.3.1 for the induction motor studied in this thesis are presented in table 5.3. The only value of λ evaluated in this thesis was $\lambda = 1$.

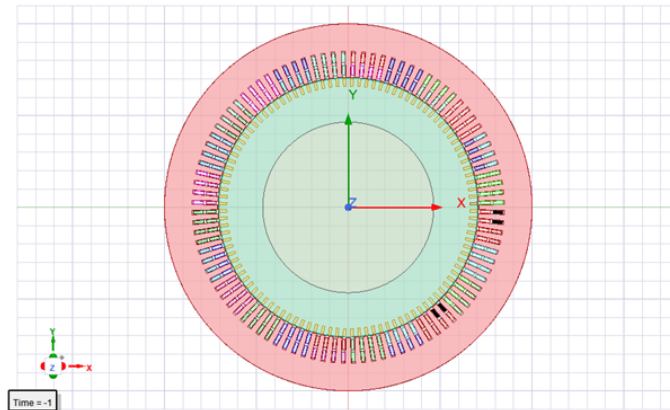


Figure 5.6: Short circuited coils in Maxwell

Table 5.2: Coil parameters for ITSC fault

| Coil Terminal | Conductor Number | Winding |
|---------------|------------------|---------|
| Ph1_P1_C1_Go | 3 | Phase A |
| Ph1_P1_C1_Ret | 3 | Phase A |
| Ph1_P1_C2_Go | 3 | Phase A |
| Ph1_P1_C2_Ret | 3 | Phase A |
| Ph1_P1_C3_Go | 9 | Phase A |
| Ph1_P1_C3_Ret | 9 | Phase A |
| Ph1_P1_C4_Go | 9 | Phase A |
| Ph1_P1_C4_Ret | 9 | Phase A |
| Ph1_P1_C5_Go | 9 | Phase A |
| Ph1_P1_C5_Ret | 9 | Phase A |
| Ph1_P1_C6_Go | 9 | Phase A |
| Ph1_P1_C6_Ret | 9 | Phase A |

Table 5.3: Characteristic frequencies for ITCS fault

| Type of Harmonic | Frequency [Hz] |
|---------------------------------------|----------------|
| Rotor slot Harmonic - Lower | 242,49 |
| Rotor Slot Harmonic - Upper | 261,51 |
| Saturation Permeance Harmonic - Lower | 223,48 |
| Saturation Permeance Harmonic - Upper | 280,52 |
| Principal Slot Harmonic - Lower | 218,62 |
| Principal Slot Harmonic - Upper | 237,63 |

5.2.2 Modelling of broken rotor bar

The broken rotor bar fault is modelled by deleting one or more rotor bars from the model. By doing this, the bar is removed in the whole axial-direction of the model. Since the fault condition is symmetrical in axial-direction, this will not have any other effect on the result

than the fact that no current will flow through the faulty bar. An illustration of one broken rotor bar is presented in figure 5.7.

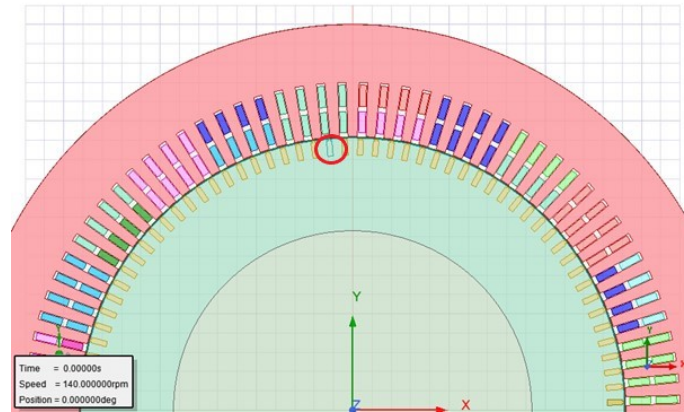


Figure 5.7: Broken rotor bar in Maxwell

The calculation of the characteristic frequencies for broken rotor bar fault as described in section 3.3.2 for the induction motor studied in this thesis are presented in table 5.4.

Table 5.4: Characteristic frequencies for broken rotor bar fault

| Type of Harmonic | Frequency [Hz] |
|------------------|----------------|
| LSB [Hz] | 9,16 |
| USB [Hz] | 9,84 |

5.2.3 Modelling of static eccentricity fault

The modelling of static eccentricity was done as described in section 3.3.3, where both the rotating parts and the band was moved a distance in the same direction, here being the x-direction. In ANSYS Maxwell, a wizzard for doing this was used. In the wizzard tool, both the rotating parts and rotating axis can be moved in x and y direction. The parameters for the static eccentricity is listed in table 5.5. The first harmonic components calculated as presented in section 3.3.3 are listed in table ???. These are the frequency components one can expect when dynamic eccentricity is present based on the literature. By moving the rotating axis 1mm, the level of eccentricity becomes 20% as the air-gap distance is 5mm.

Table 5.5: Static eccentricity parameters in Maxwell

| | |
|----------------------------|-----------------------------|
| Rotating part eccentricity | Translation (dx, dy): (0,0) |
| Rotating axis eccentricity | Translation (dx, dy): (1,0) |

Table 5.6: Characteristic frequencies for static eccentricity

| Frequency [Hz] | Frequency [Hz] |
|----------------|----------------|
| 9,33 | 177,33 |
| 46,66 | 214,66 |
| 65,33 | 233,32 |
| 102,66 | 270,66 |
| 121,33 | 289,32 |
| 158,66 | 326,65 |

5.2.4 Modelling of dynamic eccentricity

The modelling of static eccentricity was done as described in section 3.3.3, only the rotating parts was moved a distance from its original position, here being the x-direction. In ANSYS Maxwell, a wizard for doing this was used. The parameters for the dynamic eccentricity is listed in table 5.7. The first harmonic components calculated as presented in section 3.3.3 are listed in table 5.8. These are the frequency components one can expect when dynamic eccentricity is present based on the literature. By moving the rotating part 1mm, the level of eccentricity becomes 20% as the air-gap distance is 5mm.

Table 5.7: Dynamic eccentricity parameters in Maxwell

| | |
|----------------------------|-----------------------------|
| Rotating part eccentricity | Translation (dx, dy): (1,0) |
| Rotating axis eccentricity | Translation (dx, dy): (0,0) |

Table 5.8: Characteristic frequencies for static eccentricity

| Frequency [Hz] | Frequency [Hz] |
|----------------|----------------|
| 9,33 | 146,99 |
| 44,33 | 163,32 |
| 48,99 | 170,32 |
| 60,66 | 191,32 |
| 69,99 | 198,32 |
| 95,66 | 214,658 |
| 109,66 | 230,99 |
| 111,99 | 251,98 |
| 130,66 | |

5.3 Signal processing

FFT analysis is used as the signal processing tool for identifying the change of frequency components for the different faults. In order to do this, both the time step and sample length is important factors. The time step, or the sampling rate, determines the frequency range of the FFT analysis. The different sampling rates used for the different faults are presented in table 5.9.

Table 5.9: Time step for the different fault simulations

| Fault type | Time step [s] | Sampling frequency [Hz] |
|------------------------|----------------------|--------------------------------|
| ITCS faults | 0,001315 | 760,43 |
| Broken rotor bar fault | 0,01052 | 95,05 |
| Eccentricity faults | 0,001315 | 760,43 |

Having a higher sampling frequency for the ITSC and eccentricity fault analysis is that the signature frequencies of these types of fault are found in the higher frequency range of the FFT analysis. The broken rotor bar fault signature frequency is expected to be in proximity of the fundamental, hence, a sampling frequency of approx. 95 Hz is assumed sufficient. The signal length determines the resolution of the FFT analysis, i.e., the sampling step of the FFT spectrum. The signal length of the different fault simulations is presented in table 5.10.

Table 5.10: Signal length of the different fault simulations

| Fault type | Signal length [s] | Frequency resolution [Hz] |
|------------------------|--------------------------|----------------------------------|
| ITCS faults | 3,051 | 0,3278 |
| Broken rotor bar fault | 10,52 | 0,095 |
| Eccentricity faults | 3,051 | 0,3278 |

For the ITSC and eccentricity fault, a frequency resolution of approx. 0.33 is assumed sufficient, as all the simulation is analyzed with the same signal length and time step. For the broken rotor bar fault, the frequency resolution must be higher. This is because of the LSB and USB harmonics having a signature frequency of ± 0.3 Hz of the fundamental frequency.

5.4 Simulations

5.4.1 ITSC fault simulation

The different cases of ITSC fault simulation done in this thesis are presented in table 5.11

Table 5.11: ITSC fault simulations

| No. Short circuited turns | No. coils with short circuit | % short circuit in phase |
|---------------------------|------------------------------|--------------------------|
| 1 Turn | 1 | 0.35% |
| 3 Turns | 1 | 1.04% |
| 6 Turns | 1 | 2.08% |
| 6 Turns | 2 (3 turns in 2 coils) | 2.08% |
| 9 Turns | 2 (8 +1 turn in 2 coils) | 3.13% |
| 12 Turns | 2 (6 turns in 2 coils) | 4.17% |
| 14 Turn | 4 | 5% |
| 29 Turn | 4 | 10% |
| 43 Turn | 8 | 15% |
| 58 Turn | 8 | 20% |

5.4.2 Broken rotor bar simulations

The different cases of broken rotor bar fault simulated in this thesis are presented in table 5.12. The location of the faults refers to the relative location between two or more rotor bars in the induction motor.

Table 5.12: Broken rotor bar fault simulations

| No. broken bars | Location of fault |
|-----------------|-------------------|
| 1 broken bar | NA |
| 2 broken bars | Adjacent |
| 3 broken bars | Adjacent |
| 2 broken bars | 90 deg |
| 2 broken bars | 180 deg |

5.4.3 Eccentricity fault simulations

The different cases of eccentricity fault simulated in this thesis are presented in table 5.13.

Table 5.13: Eccentricity fault simulations

| Type of Eccentricity fault | displacement | % eccentricity |
|----------------------------|--------------|----------------|
| Static Eccentricity | 1mm | 20% |
| Dynamic Eccentricity | 1mm | 20% |

Chapter 6

Results

This chapter presents the results of the TSFE-simulations of the different fault presented in the thesis. The results presented is the FFT of the output stator phase current. The FFT requires a signal to be periodic. Therefore, the simulations were run until steady state was achieved. The result of the FFT gives the power spectra density (PSD) of the output signal, i.e. it gives the amplitude of the different frequency components the original signal is made up of. Since the difference between the amplitudes of the different harmonics are very large, the results are presented in logarithmic scale for the amplitudes.

6.1 Healthy Motor

6.1.1 Healthy motor with external circuit

The FFT of the phase current for the healthy motor is presented in figure 6.1. This model is excited with a voltage source in an external circuit. The sampling frequency of the simulation was reduced to include the higher frequency for comparison with ITSC faults, which have harmonic components in the upper frequency range as described in section 2.1. The frequency components with an amplitude above 0.1 are presented in table 6.1.

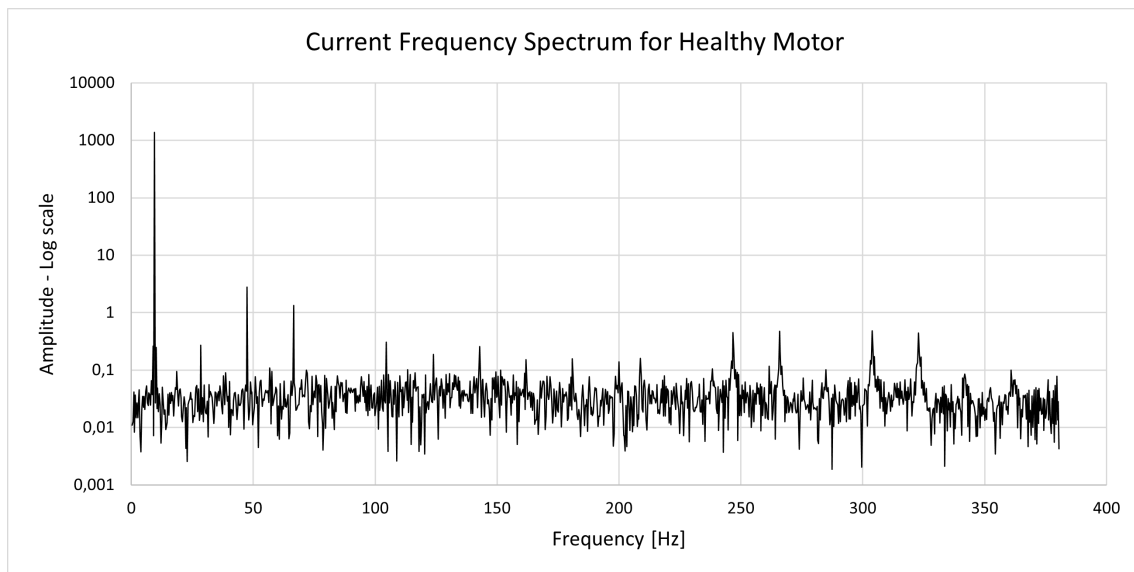


Figure 6.1: Current frequency spectrum of the healthy motor with external circuit

Table 6.1: Significant amplitudes of FFT spectrum for healthy motor

| Frequency [Hz] | Amplitude | Frequency [Hz] | Amplitude |
|----------------|-----------|----------------|-----------|
| 9,51 | 1385,18 | 246,81 | 0,45 |
| 10,16 | 0,25 | 247,14 | 0,22 |
| 28,52 | 0,27 | 265,82 | 0,48 |
| 47,53 | 2,78 | 266,15 | 0,21 |
| 66,54 | 1,32 | 303,84 | 0,49 |
| 104,56 | 0,31 | 304,17 | 0,20 |
| 142,91 | 0,26 | 322,86 | 0,44 |

6.1.2 Healthy motor without external circuit - Lower Frequency Range

Figure 6.2 show the FFT of the phase current for a healthy motor. This model is excited with a constant voltage source and is used for comparison with broken bar faults. As described in section 3.3.2, the signature frequencies are expected to be present as side-bands of the fundamental. As a result of this, the sampling frequency is reduced and simulation time increased to reduce computation time. This result in a low frequency range and high frequency resolution.

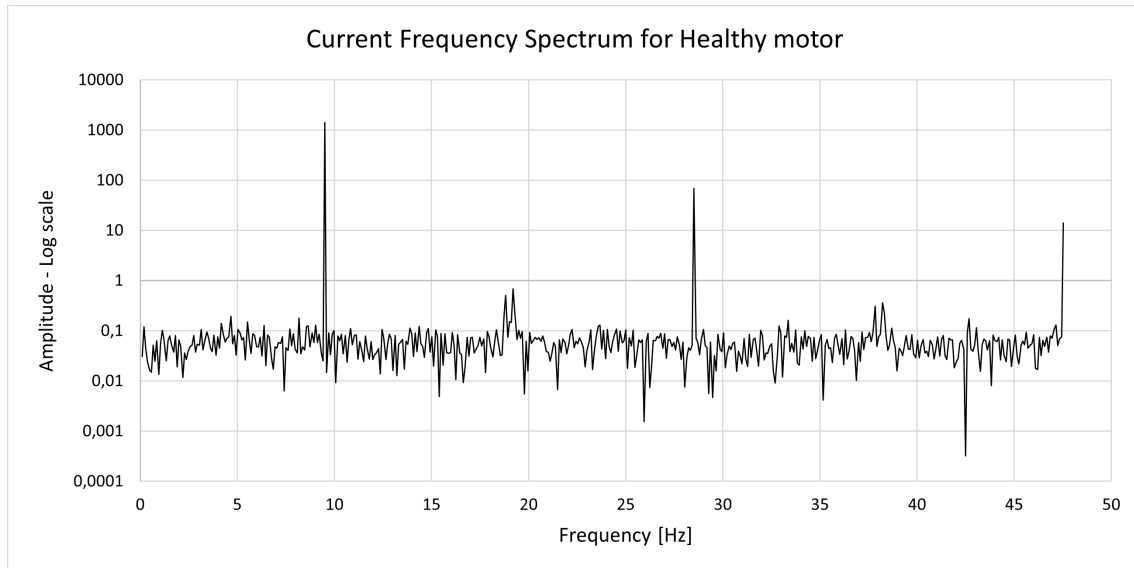


Figure 6.2: Low range current frequency spectrum of the healthy motor

6.1.3 Healthy motor without external Circuit - Higher Frequency Range

The FFT of the phase current of a healthy motor is presented in figure 6.3. This model is excited with a constant voltage source and is used for comparison with the eccentricity faults. Because of the characteristics of eccentricity faults presented in 3.3.3, a higher frequency range is required for the the FFT analysis as for the ITSC faults. The 3rd and multiple of this harmonic comes from a difference in phase connection between the model with external circuit and without.

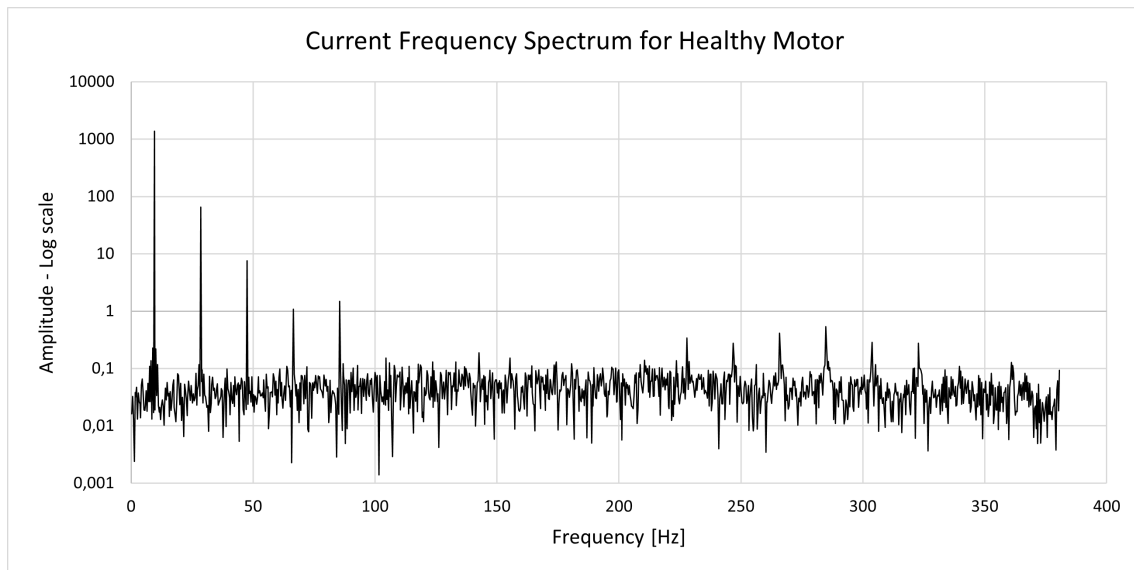


Figure 6.3: High range current frequency spectrum of the healthy motor

6.2 ITSC faults - 1 or 2 coils with Short Circuit

6.2.1 1 Turn Short Circuit

Figure 6.4 show the results of the FFT analysis for the stator phase current for 1 short circuited turn in one coil. All the frequency components with an amplitude above 0.2 are listed in table 6.2. From the plot is is clear that no significant rise in any higher frequency components occur. The only noticeable rise is for the 3rd harmonic component of the fundamental.

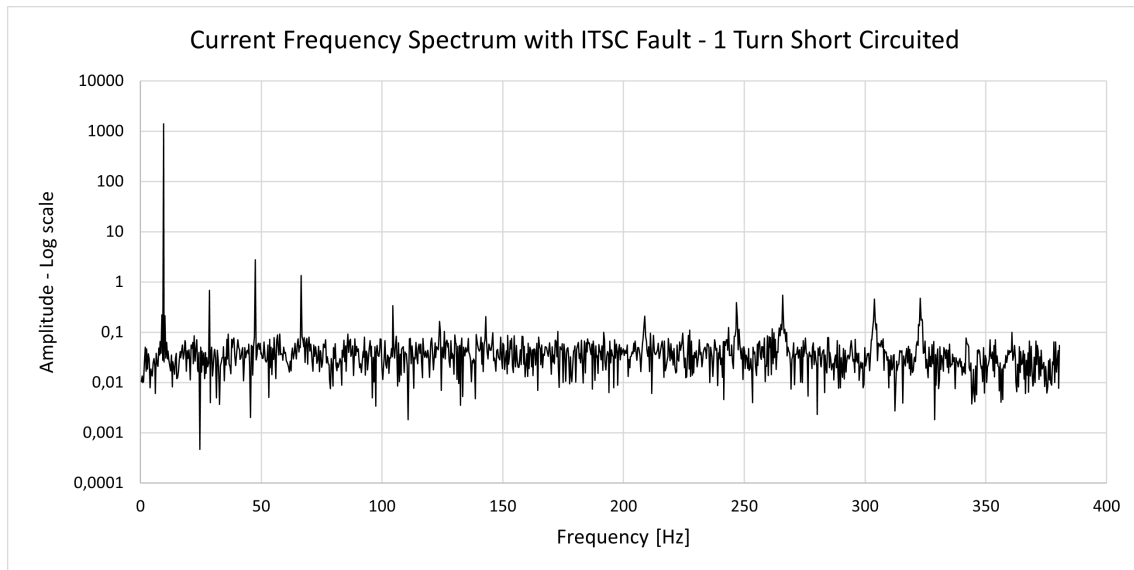


Figure 6.4: Current frequency spectrum of 1 short circuited turn

Table 6.2: Significant amplitudes of FFT spectrum - 1 turn short circuited

| Frequency [Hz] | Amplitude | Frequency [Hz] | Amplitude |
|----------------|-----------|----------------|-----------|
| 9,51 | 1392,85 | 208,79 | 0,21 |
| 10,16 | 0,21 | 246,81 | 0,39 |
| 28,52 | 0,68 | 265,82 | 0,54 |
| 47,53 | 2,78 | 266,15 | 0,26 |
| 66,54 | 1,36 | 303,84 | 0,46 |
| 104,56 | 0,34 | 322,86 | 0,47 |
| 142,91 | 0,20 | | |

6.2.2 3 Turn Short Circuit

Figure 6.5 show the results of the FFT analysis for the stator phase current for 3 short circuited turns in one coil. The frequency components with an amplitude above 0.2 are presented in table 6.3. The most significant change compared to the healthy case, is the rise of the 28.52[Hz] and the appearance of the 123.90[Hz] frequency component in the table of amplitudes above 0.2.

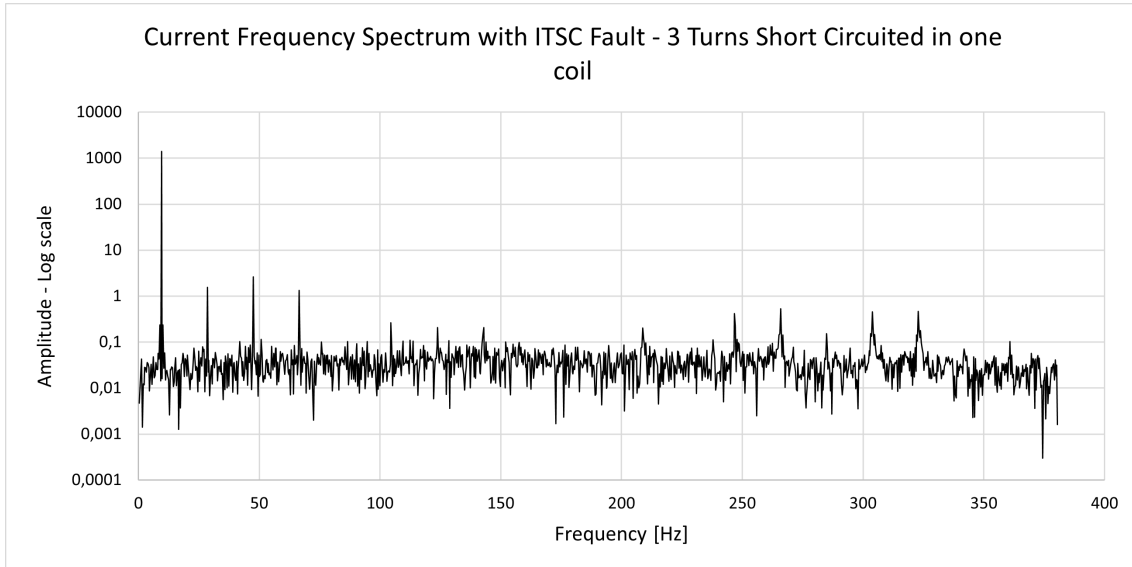


Figure 6.5: Current frequency spectrum of 3 short circuited turns

Table 6.3: Significant amplitudes of FFT spectrum - 3 turns short circuited

| Frequency [Hz] | Amplitude | Frequency [Hz] | Amplitude |
|----------------|-----------|----------------|-----------|
| 8,85 | 0,24 | 142,91 | 0,21 |
| 9,51 | 1409,54 | 208,79 | 0,20 |
| 10,16 | 0,23 | 246,81 | 0,42 |
| 28,52 | 1,54 | 247,14 | 0,23 |
| 47,53 | 2,64 | 265,82 | 0,53 |
| 66,54 | 1,33 | 266,15 | 0,21 |
| 104,56 | 0,26 | 303,84 | 0,46 |
| 123,90 | 0,21 | 322,86 | 0,46 |

6.2.3 6 Short Circuited Turns in one phase

Figure 6.6 show the results of the FFT analysis for the stator phase current for 6 short circuited turns in one coil. The frequency components with an amplitude above 0.2 are presented in taqble 6.4. The most noticeable change is the increasing 28.52[Hz] frequency component and the appearance of 85.55[Hz] and 284.83[Hz] in the table.

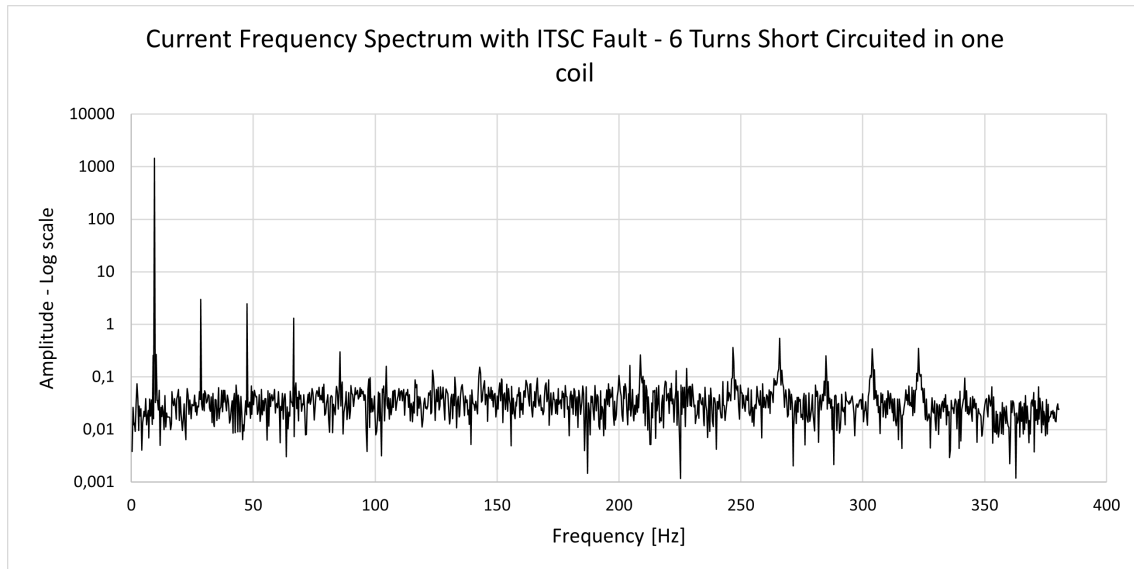


Figure 6.6: Current frequency spectrum with 6 short circuited turns

Table 6.4: Significant amplitudes of FFT spectrum - 6 turns short circuited

| Frequency [Hz] | Amplitude | Frequency [Hz] | Amplitude |
|----------------|-----------|----------------|-----------|
| 8,85 | 0,26 | 208,79 | 0,26 |
| 9,51 | 1438,06 | 246,81 | 0,37 |
| 10,16 | 0,27 | 265,82 | 0,54 |
| 28,52 | 3,00 | 266,15 | 0,23 |
| 47,53 | 2,47 | 284,83 | 0,25 |
| 66,54 | 1,30 | 303,84 | 0,35 |
| 85,55 | 0,30 | 322,86 | 0,35 |

6.2.4 6 Turn Short Circuited - 3 turns in 2 coil

Figure 6.7 show the results of the FFT analysis for the stator phase current for 6 short circuited turns, 3 turns in 2 coil. The frequency components with an amplitude above 0.2 are presented in table 6.5. The only change compared with the results in section 6.2.3 is the appearance of 247.14[Hz] component and missing 208.79[Hz] component.

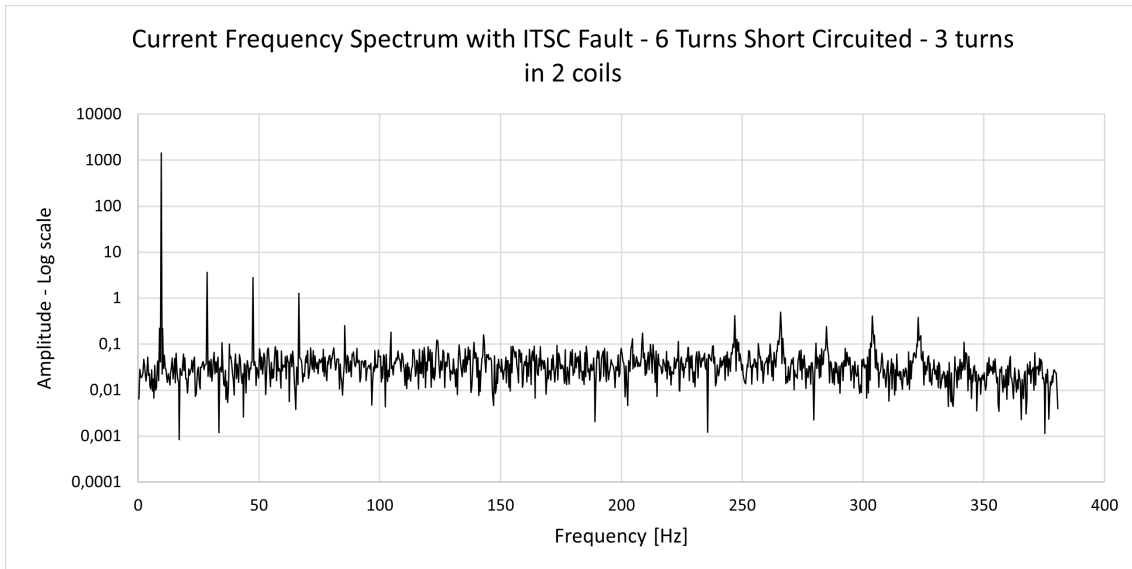


Figure 6.7: Current frequency spectrum with 6 turn short circuited, 3 turns in 2 coils

Table 6.5: Significant amplitudes of FFT spectrum - 6 Turn Short Circuited, 3 in 2 coils

| Frequency [Hz] | Amplitude | Frequency [Hz] | Amplitude |
|----------------|-----------|----------------|-----------|
| 8,85 | 0,22 | 246,81 | 0,42 |
| 9,51 | 1450,17 | 247,14 | 0,23 |
| 10,16 | 0,22 | 265,82 | 0,50 |
| 28,52 | 3,62 | 266,15 | 0,20 |
| 47,53 | 2,78 | 284,83 | 0,24 |
| 66,54 | 1,28 | 303,84 | 0,41 |
| 85,55 | 0,25 | 322,86 | 0,39 |

6.2.5 9 Short Circuited Turns

Figure 6.8 show the results of the FFT analysis for the stator phase current for 9 short circuited turns, 8 turns in one coil and 1 in the adjacent coil. All frequency component with an amplitude larger than 0.2 are listed in table 6.6. For the 9-turn short circuit fault, there exist 19 frequencies with an amplitude above 0.2. The component of 28.52[Hz] is still increasing. In addition, side band harmonics for the upper frequency range components also present for the healthy motor is appearing. Of these mentioned harmonics, it is only the 204.53[Hz] and 261.56[Hz] frequency component with an amplitude above 0.2.

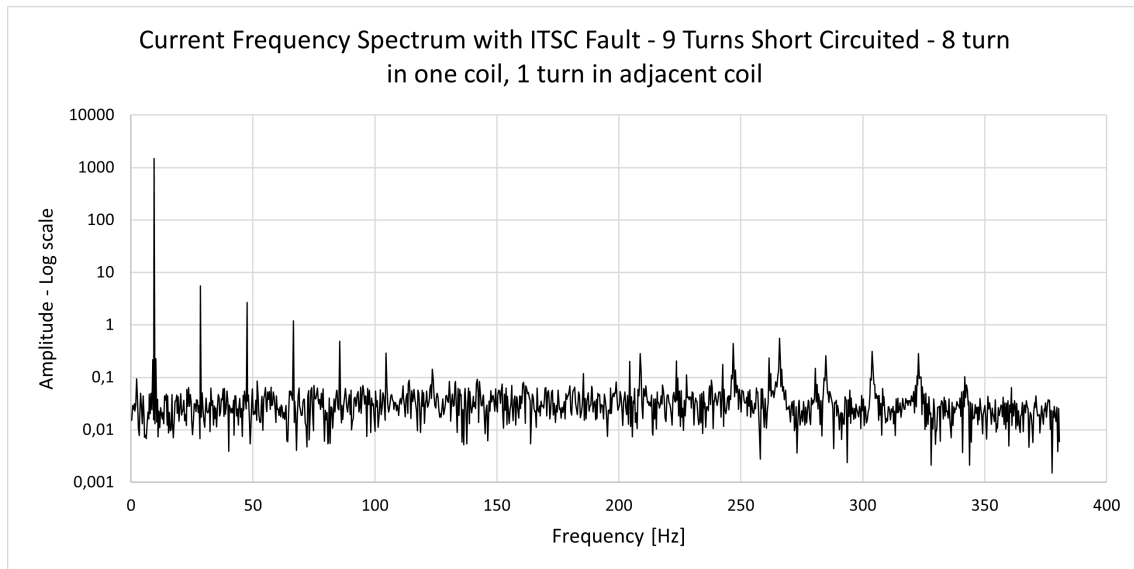


Figure 6.8: Current frequency spectrum with 9 short circuited turns

Table 6.6: Significant amplitudes of FFT spectrum - 9 turn short circuited

| Frequency [Hz] | Amplitude | Frequency [Hz] | Amplitude |
|----------------|-----------|----------------|-----------|
| 8,85 | 0,22 | 223,54 | 0,21 |
| 9,51 | 1477,25 | 246,81 | 0,44 |
| 10,16 | 0,23 | 247,14 | 0,24 |
| 28,52 | 5,56 | 261,56 | 0,23 |
| 47,53 | 2,67 | 265,82 | 0,55 |
| 66,54 | 1,19 | 266,15 | 0,20 |
| 85,55 | 0,49 | 284,83 | 0,26 |
| 104,56 | 0,29 | 303,84 | 0,31 |
| 204,53 | 0,20 | 322,86 | 0,28 |
| 208,79 | 0,28 | | |

6.2.6 12 Turn Short Circuited - 6 turns in 2 coil

Figure 6.9 show the results of the FFT analysis for the stator phase current for 12 short circuited turns, 6 turns in 2 adjacent coils. The 20 frequency components presented in table 6.7 have an amplitude above 0.2. The most noticeable changes are the new amplitudes in the higher frequency spectrum. These are 242.55[Hz] and 280.83[Hz]. In addition the frequency component of 261.56[Hz] and 28.52[Hz] have increased significantly. Also, the lower frequency of 2.29[Hz] have appeared in the table with an amplitude of 0.2.

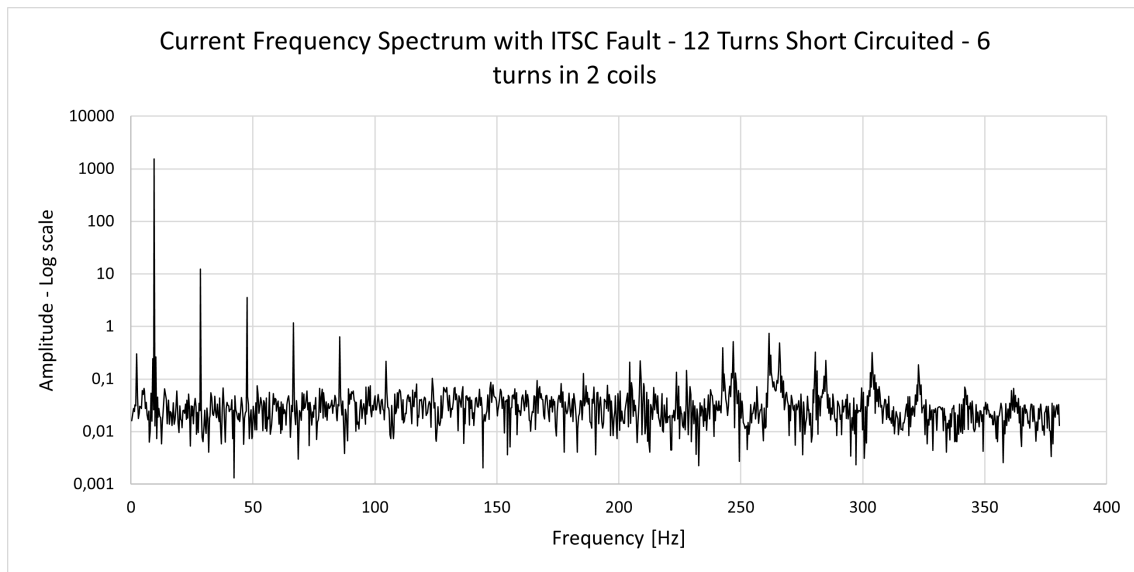


Figure 6.9: Current frequency spectrum with 12 short circuited turns

Table 6.7: Significant amplitudes of FFT spectrum - 12 turn short circuited

| Frequency [Hz] | Amplitude | Frequency [Hz] | Amplitude |
|----------------|-----------|----------------|-----------|
| 2,29 | 0,30 | 208,79 | 0,22 |
| 8,85 | 0,25 | 242,55 | 0,39 |
| 9,51 | 1549,12 | 246,81 | 0,51 |
| 10,16 | 0,26 | 247,14 | 0,24 |
| 28,52 | 12,32 | 261,56 | 0,73 |
| 47,53 | 3,58 | 262,22 | 0,29 |
| 66,54 | 1,17 | 265,82 | 0,49 |
| 85,55 | 0,63 | 280,57 | 0,33 |
| 104,56 | 0,22 | 284,83 | 0,23 |
| 204,53 | 0,21 | 303,84 | 0,32 |

6.3 ITSC Fault - Percent of turns in one phase

This section present the current frequency spectrum of 5%, 10%, 15% and 20% short circuited turns in one phase. The short circuited turns are distributed between the four parallel branches in the phase.

6.3.1 5% ITSC of phase A

The current frequency spectrum of the model with 5% short circuited turns in phase A are presented in figure 6.10. 5% of the turns in the phase equals 14 turns in total. These are as evenly distributed as possible between the four parallel branches in the phase. The spectrum show two clear increase in amplitude for the 28.5[Hz] and 284.83[Hz] frequency components compared to the healthy case. The frequencies with an amplitude above 0.2 are listed in table 6.8

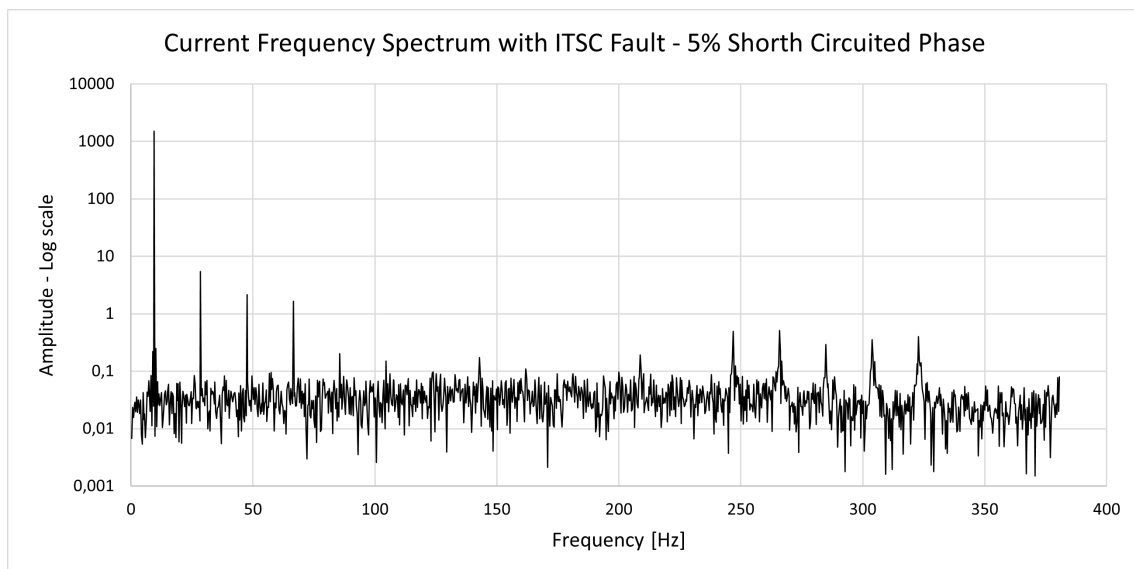


Figure 6.10: Current frequency spectrum for 5% short circuited phase

Table 6.8: Significant amplitudes of FFT spectrum - 5% short circuited phase

| Frequency [Hz] | Amplitude | Frequency [Hz] | Amplitude |
|----------------|-----------|----------------|-----------|
| 8,85 | 0,22 | 246,81 | 0,49 |
| 9,51 | 1500,77 | 247,14 | 0,24 |
| 10,16 | 0,25 | 265,82 | 0,51 |
| 28,52 | 5,44 | 266,15 | 0,23 |
| 47,53 | 2,13 | 284,83 | 0,29 |
| 66,54 | 1,66 | 303,84 | 0,35 |
| 85,55 | 0,20 | 322,86 | 0,40 |

6.3.2 10% ITSC of phase A

Figure 6.11 show the current frequency spectrum of phase A for 10% short circuited phase. 10% of the turns short circuited equals 29 turns in turns in total. These are as evenly distributed as possible between the four parallel branches in the phase. The most significant increase in amplitude is for the 28.5[Hz], 284.83 and the 208.79[Hz] frequency amplitude which is present in the table now. The frequency components with an amplitude above 0.2 are listed in table 6.9.

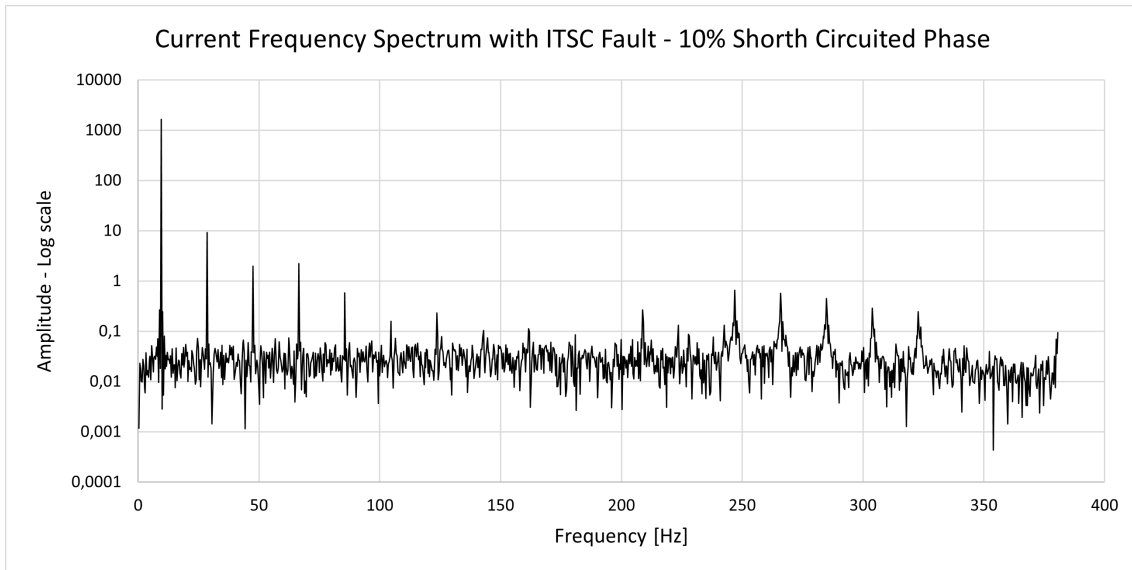


Figure 6.11: Current frequency spectrum for 10% short circuited phase

Table 6.9: Significant amplitudes of FFT spectrum - 10% short circuited phase

| Frequency [Hz] | Amplitude | Frequency [Hz] | Amplitude |
|----------------|-----------|----------------|-----------|
| 8,85 | 0,27 | 246,81 | 0,65 |
| 9,51 | 1649,01 | 247,14 | 0,31 |
| 10,16 | 0,25 | 265,82 | 0,57 |
| 28,52 | 9,28 | 266,15 | 0,23 |
| 47,53 | 1,96 | 284,83 | 0,45 |
| 66,54 | 2,21 | 285,16 | 0,20 |
| 85,55 | 0,58 | 303,84 | 0,29 |
| 123,57 | 0,23 | 322,86 | 0,25 |
| 208,79 | 0,27 | | |

6.3.3 15% ITSC of phase A

The current frequency spectrum of the model with 15% short circuited turns in phase A are presented in figure ???. 15% of the turns in the phase equals 43 turns in total. These are as evenly distributed as possible between the four parallel branches in the phase. The frequency components with an amplitude above 0.2 are listed in table 6.10. The spectrum show clear peaks for the same frequencies as for 10% short circuit, but the 285.16[Hz] and 322.86[Hz] are not present in table 6.10.

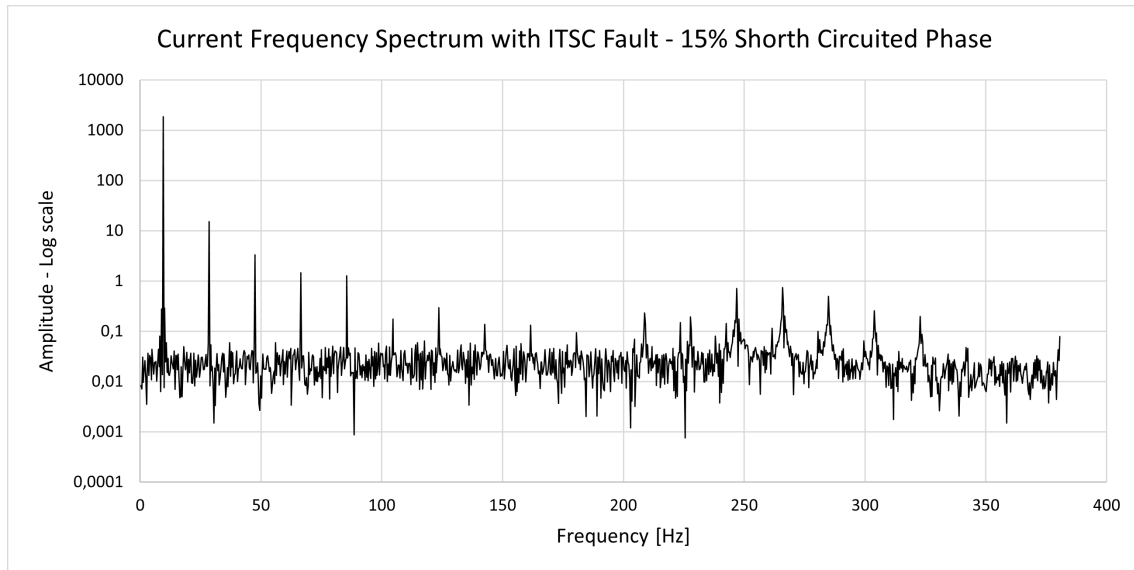


Figure 6.12: Current frequency spectrum for 15% short circuited phase

Table 6.10: Significant amplitudes of FFT spectrum - 15% short circuited phase

| Frequency [Hz] | Amplitude | Frequency [Hz] | Amplitude |
|----------------|-----------|----------------|-----------|
| 8,85 | 0,27 | 208,79 | 0,23 |
| 9,51 | 1874,28 | 246,81 | 0,71 |
| 10,16 | 0,29 | 247,14 | 0,34 |
| 28,52 | 15,21 | 265,82 | 0,73 |
| 47,53 | 3,33 | 266,15 | 0,32 |
| 66,54 | 1,47 | 284,83 | 0,50 |
| 85,55 | 1,27 | 303,84 | 0,26 |
| 123,57 | 0,30 | | |

6.3.4 20% ITSC of phase A

Figure 6.13 show the current frequency spectrum of phase A for 20% short circuited phase. 20% of the turns short circuited equals 58 turns in turns in total. These are as evenly distributed as possible between the four parallel branches in the phase. The frequency components with an amplitude above 0.2 are listed in table 6.11. Figure 6.13 show that is now exist several side-band harmonics for the higher range frequency components presented for the less severe faults above. These components are the 242.55[Hz] and 261.56[Hz] in particular. In addition, several new frequency components are now present in table 6.11.

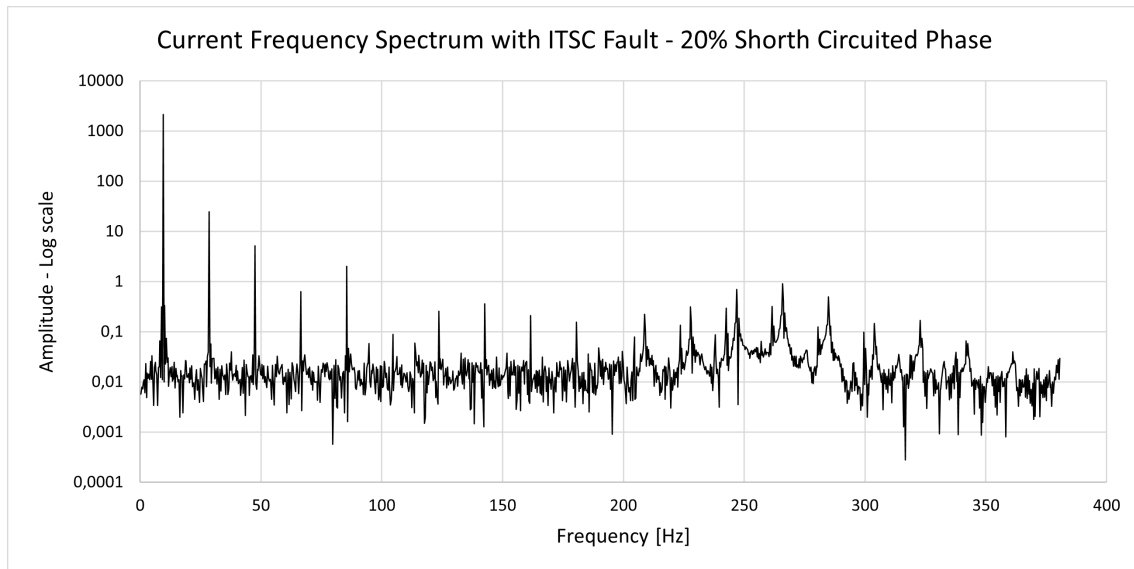


Figure 6.13: Current frequency spectrum for 20% short circuited phase

Table 6.11: Significant amplitudes of FFT spectrum - 20% short circuited phase

| Frequency [Hz] | Amplitude | Frequency [Hz] | Amplitude |
|----------------|-----------|----------------|-----------|
| 8,85 | 0,32 | 227,80 | 0,32 |
| 9,51 | 2152,50 | 242,55 | 0,29 |
| 10,16 | 0,33 | 246,81 | 0,70 |
| 28,52 | 24,44 | 247,14 | 0,35 |
| 47,53 | 5,12 | 261,56 | 0,32 |
| 66,54 | 0,63 | 265,17 | 0,20 |
| 85,55 | 2,03 | 265,50 | 0,22 |
| 123,57 | 0,25 | 265,82 | 0,90 |
| 142,58 | 0,36 | 266,15 | 0,40 |
| 161,59 | 0,21 | 266,81 | 0,24 |
| 208,79 | 0,22 | 284,83 | 0,50 |

6.4 Broken Bar Fault

6.4.1 1 Broken Bar

The FFT analysis of the phase current of the induction motor model with 1 broken bar is presented in figure 6.14. The frequencies with an amplitude above 5.0 are listed in table 6.12. The changes in the spectrum compared to the healthy model is the rise of lower side band harmonics at 9.13[Hz], 9.22[Hz], 27.85[Hz] and 28.14[Hz].

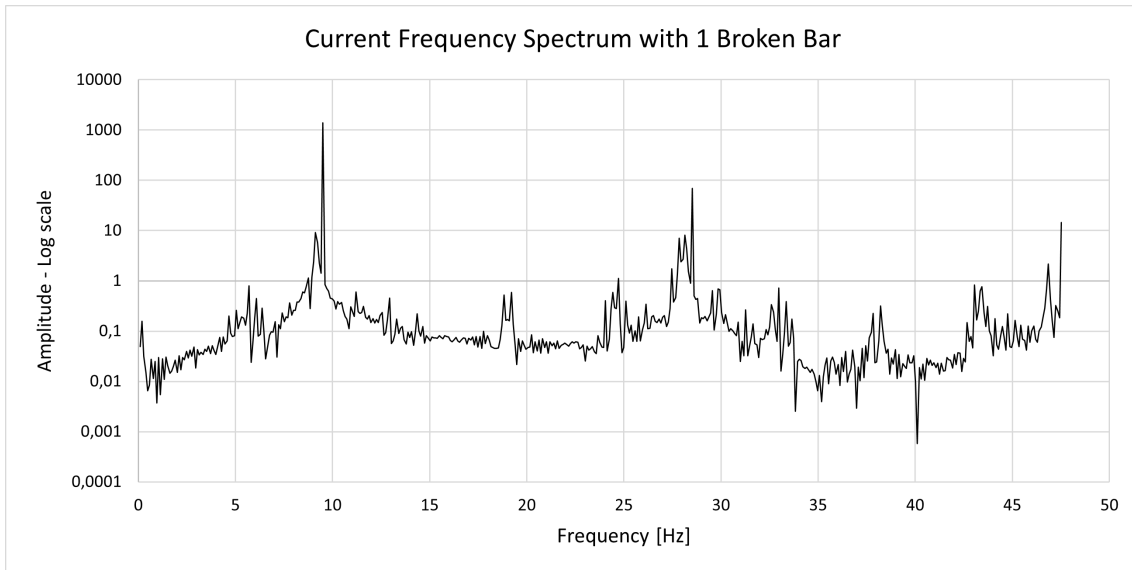


Figure 6.14: Current frequency spectrum with 1 Broken Bar

Table 6.12: Significant amplitudes of FFT spectrum - 1 Broken Bar

| Frequency [Hz] | Amplitude | Frequency [Hz] | Amplitude |
|----------------|-----------|----------------|-----------|
| 9,13 | 9,06 | 28,14 | 8,06 |
| 9,22 | 5,79 | 28,52 | 69,57 |
| 9,51 | 1390,35 | 47,53 | 14,40 |
| 27,85 | 7,07 | | |

6.4.2 2 Broken Bars

Figure 6.15 show the phase current frequency spectrum with 2 adjacent broken bars. The components with an amplitude above 5.0 is presented in table 6.13. The relevant changes are the significant rise in amplitude of the 9.13 [Hz], 9.22 [Hz], 27.85 [Hz] and 28.14 [Hz] components. In addition, the 28.04 [Hz] and 28.23 [Hz] frequencies components are now above 5.0 in amplitude and presented in the table.

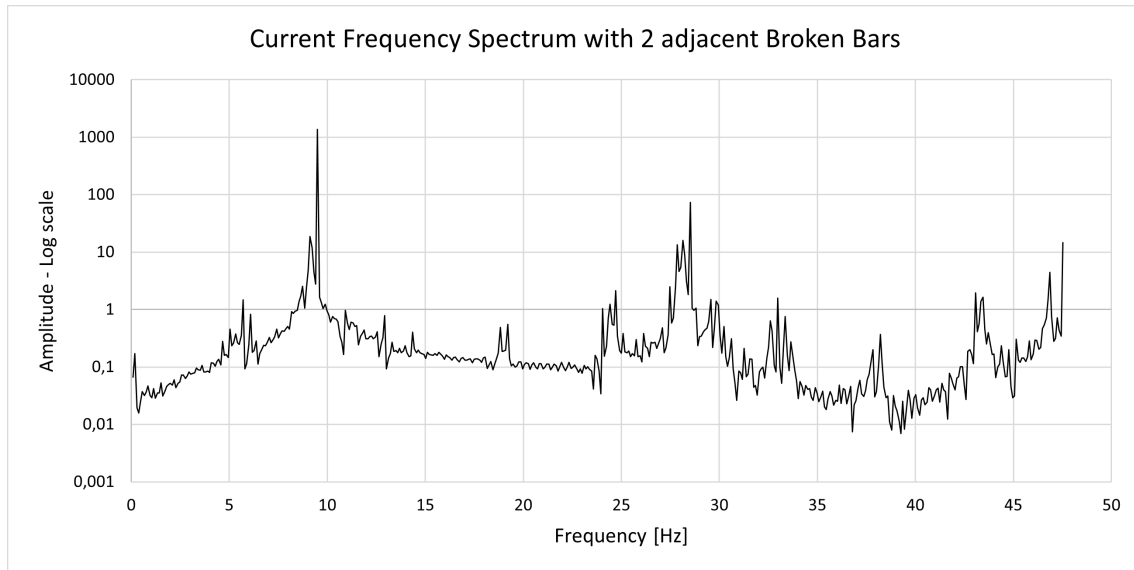


Figure 6.15: Current frequency spectrum with 2 Broken Bars

Table 6.13: Significant amplitudes of FFT spectrum - 2 Broken Bars

| Frequency [Hz] | Amplitude | Frequency [Hz] | Amplitude |
|----------------|-----------|----------------|-----------|
| 9,13 | 18,57 | 28,14 | 16,00 |
| 9,22 | 11,78 | 28,23 | 8,74 |
| 9,51 | 1377,99 | 28,52 | 73,55 |
| 27,85 | 13,33 | 47,53 | 14,54 |
| 28,04 | 5,38 | | |

6.4.3 3 Broken Bars

Figure 6.16 show the phase current frequency spectrum with 3 adjacent broken bars. The components with an amplitude above 5.0 is presented in table 6.14. The relevant changes are the significant rise in amplitude of the 9.13 [Hz], 9.22 [Hz], 27.85 [Hz], 28.04 [Hz], 28.14 [Hz] and 28.23 [Hz] frequency components. Two additional frequencies are now listed in the table, being the 9.03 [Hz] and 27.95 [Hz] frequency component.

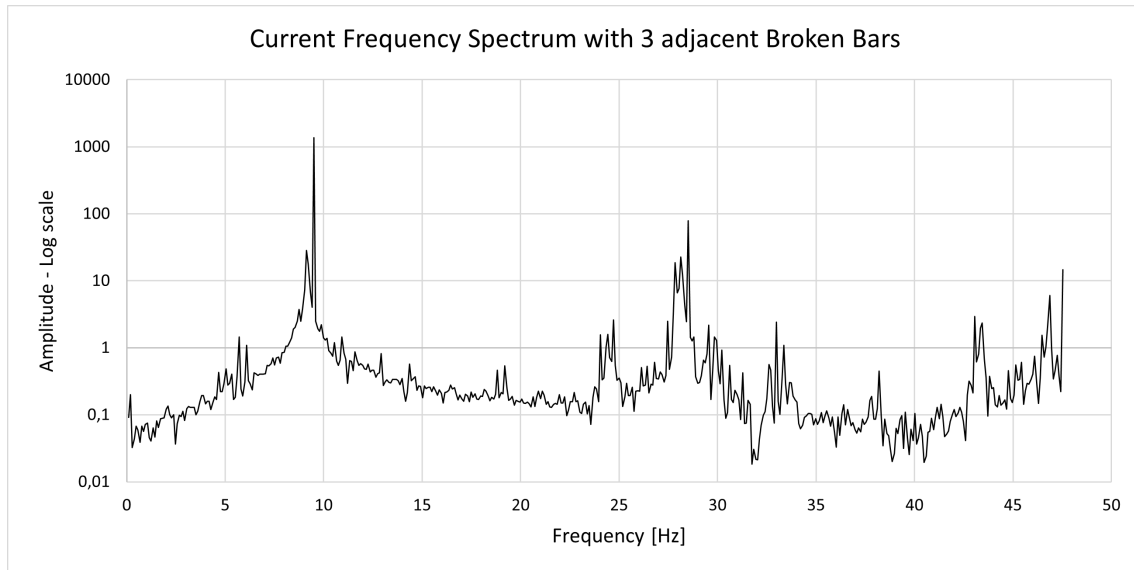


Figure 6.16: Current frequency spectrum with 3 Broken Bars

Table 6.14: Significant amplitudes of FFT spectrum - 3 Broken Bars

| Frequency [Hz] | Amplitude | Frequency [Hz] | Amplitude |
|----------------|-----------|----------------|-----------|
| 9,03 | 7,40 | 28,04 | 7,65 |
| 9,13 | 28,22 | 28,14 | 22,72 |
| 9,22 | 17,87 | 28,23 | 12,37 |
| 9,32 | 6,82 | 28,52 | 79,30 |
| 9,51 | 1366,48 | 46,86 | 6,08 |
| 27,85 | 18,68 | 47,53 | 14,56 |
| 27,95 | 6,62 | | |

6.4.4 2 Broken Bars - 90 deg relative

The FFT analysis of the phase current of the induction motor model with 2 broken bar 90 deg relative to each other is presented in figure 6.17. The frequencies with an amplitude above 5 are listed in table 6.15. Compared with the case of 2 adjacent broken bars, the amplitudes are much the same. The most noticeable change is the increased ripple in the whole frequency spectrum.

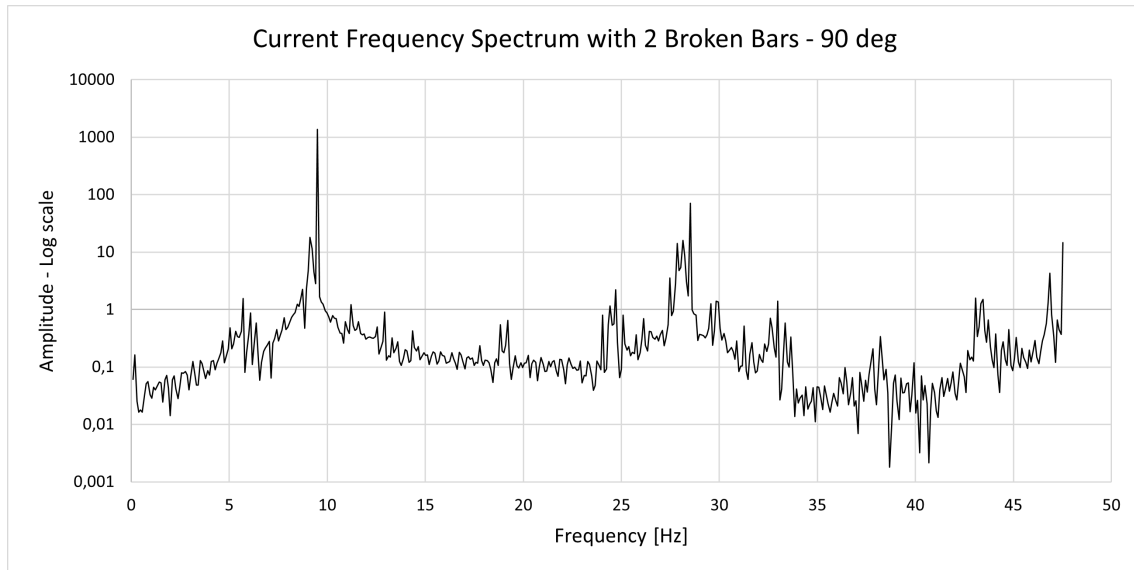


Figure 6.17: Current frequency spectrum with 2 Broken Bars 90 deg relative to each other

Table 6.15: Significant amplitudes of FFT spectrum - 2 Broken Bars 90 deg

| Frequency [Hz] | Amplitude | Frequency [Hz] | Amplitude |
|----------------|-----------|----------------|-----------|
| 9,13 | 18,04 | 28,14 | 16,00 |
| 9,22 | 11,46 | 28,23 | 8,64 |
| 9,51 | 1378,10 | 28,52 | 70,30 |
| 27,85 | 14,12 | 47,53 | 14,70 |
| 28,04 | 5,43 | | |

6.4.5 2 Broken Bars - 180 deg relative

Figure 6.18 show the phase current frequency spectrum with 2 broken bars 180 deg relative to each other. The components with an amplitude above 5 is presented in table 6.16. When comparing the frequency components and amplitudes in 6.15 and 6.16, they are almost identical. The most noticeable change is the reduced presence or ripple in the frequency spectrum.

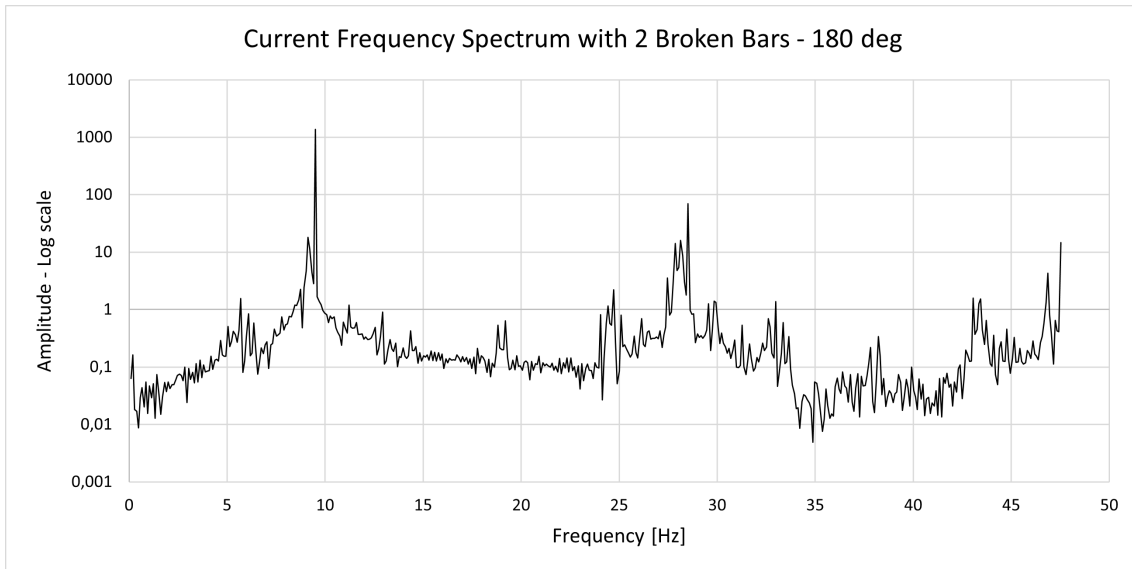


Figure 6.18: Current frequency spectrum with 2 Broken Bars 180 deg relative to each other

Table 6.16: Significant amplitudes of FFT spectrum - 2 Broken Bars 180 deg

| Frequency [Hz] | Amplitude | Frequency [Hz] | Amplitude |
|----------------|-----------|----------------|-----------|
| 9,13 | 18,04 | 28,14 | 15,99 |
| 9,22 | 11,46 | 28,23 | 8,61 |
| 9,51 | 1378,11 | 28,52 | 70,31 |
| 27,85 | 14,12 | 47,53 | 14,68 |
| 28,04 | 5,43 | | |

6.5 Eccentricity fault

6.5.1 Static Eccentricity

The phase current frequency spectrum of the model with static eccentricity is presented in figure 6.19. The most significant rise in amplitude is for the 3rd and 9th harmonic of the fundamental frequency. There also exist some side-band harmonics around other multiple of the fundamental frequency with static eccentricity present.

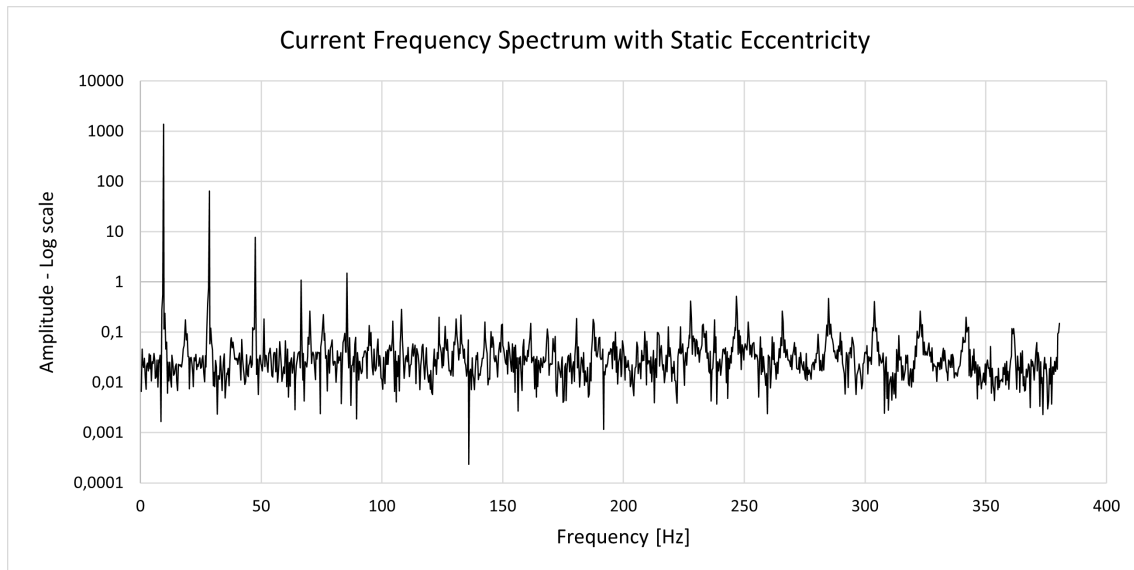


Figure 6.19: Current frequency spectrum with static eccentricity of 1mm

6.5.2 Dynamic Eccentricity

Figure 6.20 show the frequency spectrum of the phase current in the induction motor model with dynamic eccentricity. Compared to the healthy case, the most significant rise in amplitudes are for the 3rd and 9th harmonic components of the fundamental frequency. Several side-band harmonics around multiple of the fundamental frequency exist here, like for the static eccentricity.

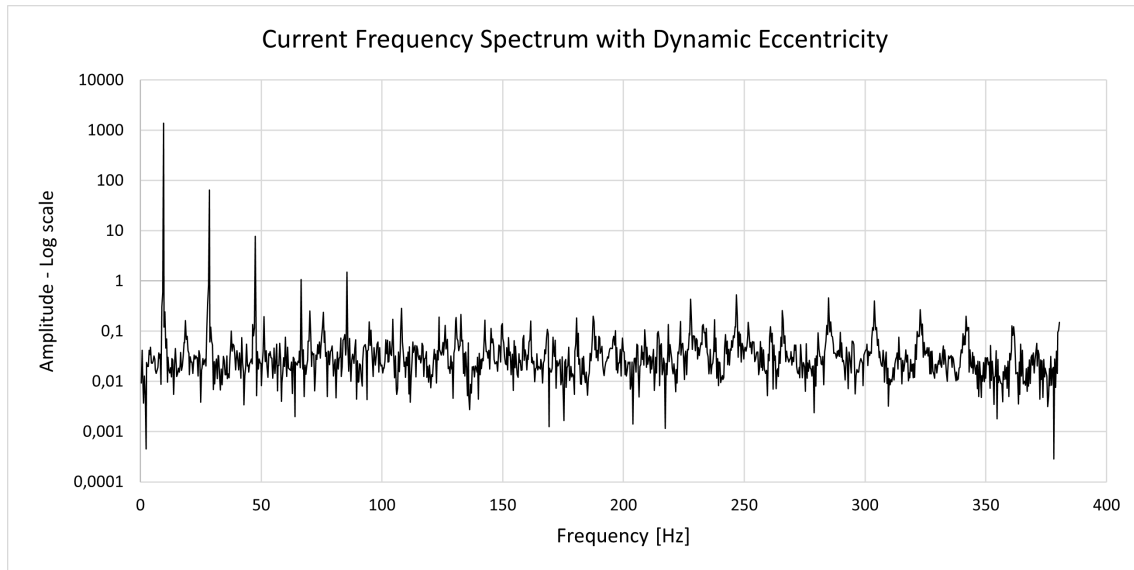


Figure 6.20: Current frequency spectrum with dynamic eccentricity of 1mm

6.6 Comparison of healthy and faulty cases

6.6.1 ITSC Faults with % Short Circuited Turns in Phase A

Based on a difference of 0.1 in amplitude between healthy and 20% short circuited turns in phase simulations, a selection of frequency components are selected for comparison. To have a better resolution, the frequencies are divided in three different plots, being the lower, mid and upper range.

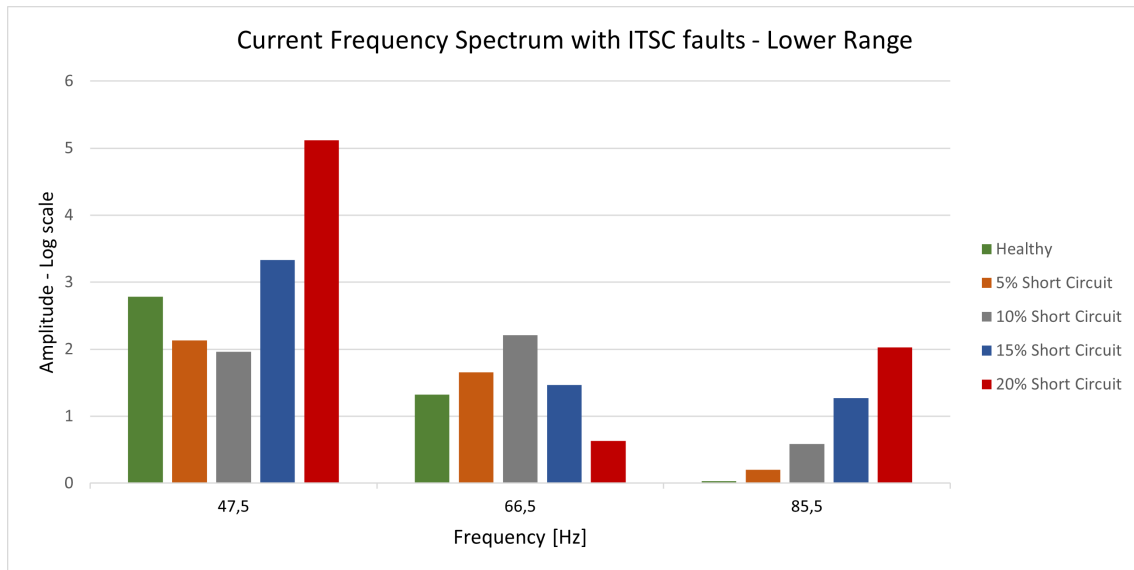


Figure 6.21: Comparison of lower range current frequency components for % ITSC of Phase A

Figure 6.23 show the upper frequency spectrum for the different faulty cases. Here, it is clear that the frequency components of 85.5[Hz], 123.9[Hz], 180.9[Hz], 284.8[Hz] and 303.8[Hz] are decreasing with increasing fault severity. In addition, the component of 281.2 [Hz] is increasing gradually with fault severity.

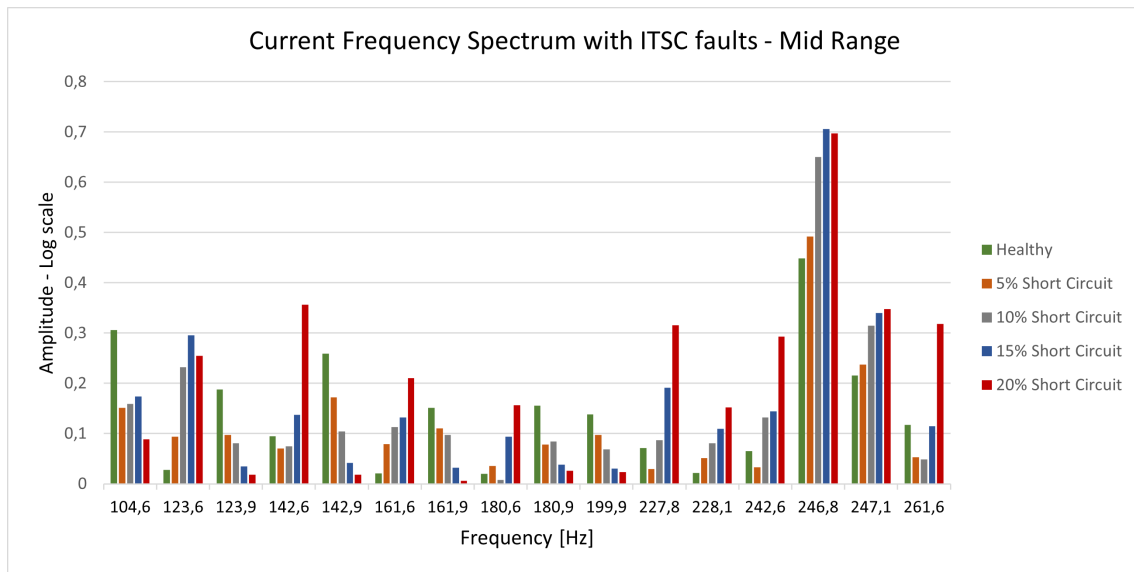


Figure 6.22: Comparison of mid range current frequency components for % ITSC of Phase A

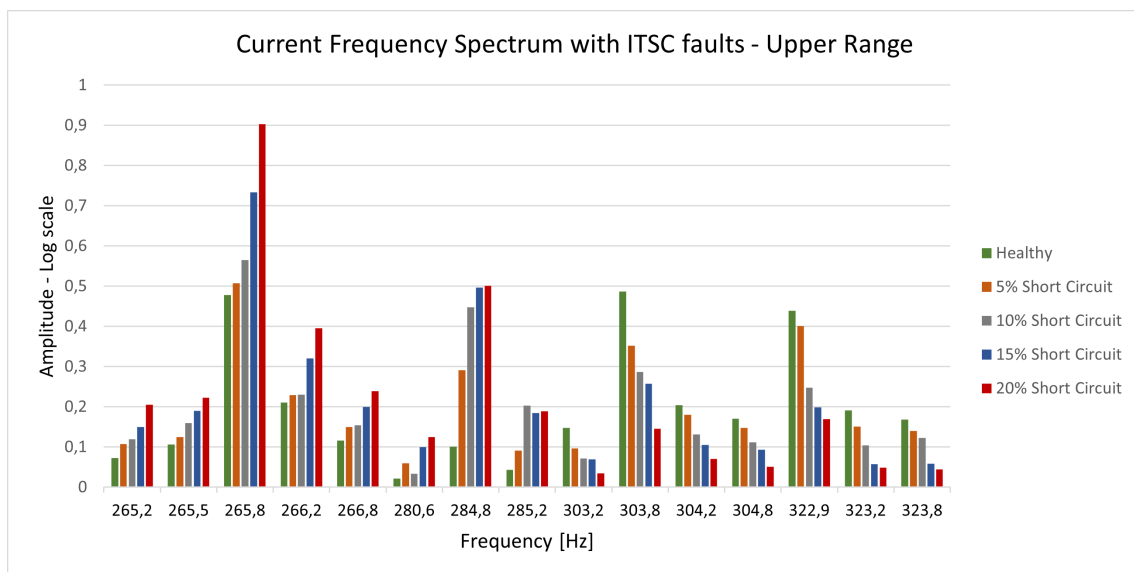


Figure 6.23: Comparison of upper range current frequency components for % ITSC of Phase A

6.6.2 ITSC Fault in 1 or 2 Coils

Based on the frequencies presented in table 6.7 from the case where 12 turns are short circuited, a selection of frequencies were selected for comparing the amplitudes of these frequencies for different fault severity. To have a better resolution, the frequencies are divided in two different plots, being the lower range and upper range. Figure 6.24 show a comparison of the lower amplitudes for ITSC faults in one or two coils. The result show a significant rise in the

amplitude of the 28.5[Hz] frequency component with increasing fault severity, except from the 1-Turn short circuit case.

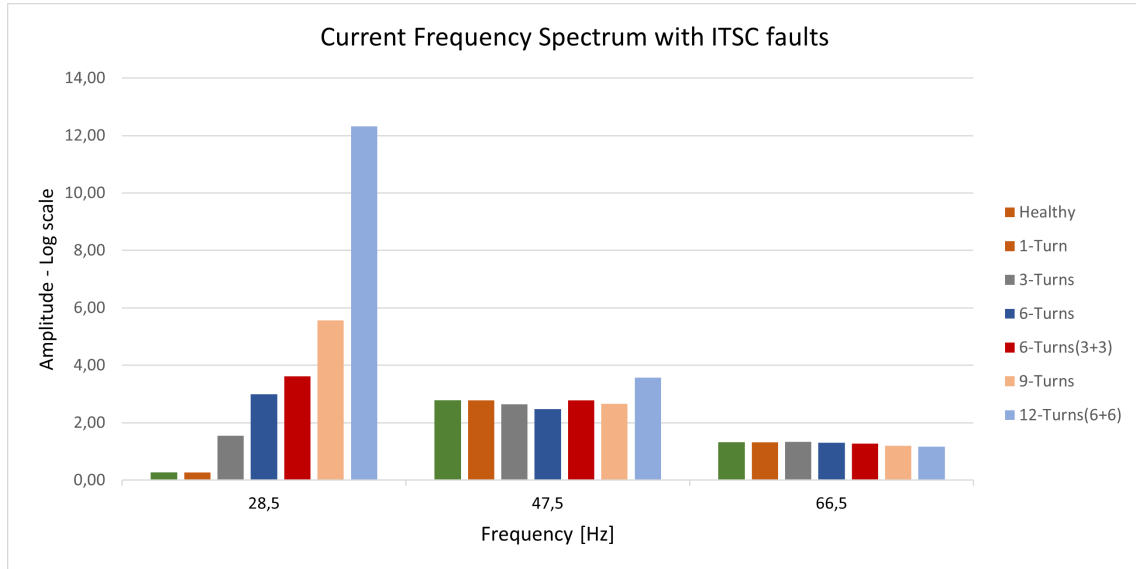


Figure 6.24: Comparison of lower current frequency components with ITSC fault

Figure 6.25 show a comparison of the amplitudes of the upper frequency range. The results show that the only frequency components with a steady rise in amplitude for increasing fault severity is 85.5[Hz] and 204.5[Hz]. Worth to mention is the fact that the 6-turn fault in one coil have a larger amplitude that the 6-Turn fault with 3 turn short circuited in two coils for these frequencies. The 280.6[Hz] Increase steady with increasing fault severity, except for the 1-turn and 3-Turn short circuit.

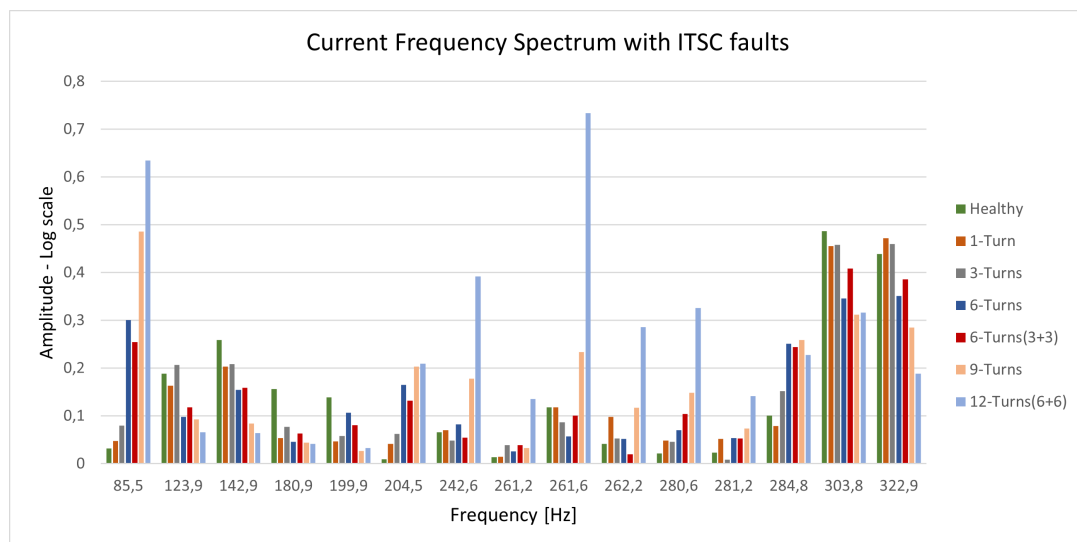


Figure 6.25: Comparison of upper current frequency components with ITSC fault

6.6.3 Broken Bar Faults

Figure 6.26 show a comparison of the most significant frequency amplitudes with different cases of broken bar fault. The results show a significant rise in all amplitudes with increasing fault severity. The only significant frequency component for the model with external circuit is the 9.1[Hz] and 9.2[Hz] frequency component. The effect of moving two broken bars in relation to each other have a very small impact on the frequency spectrum.

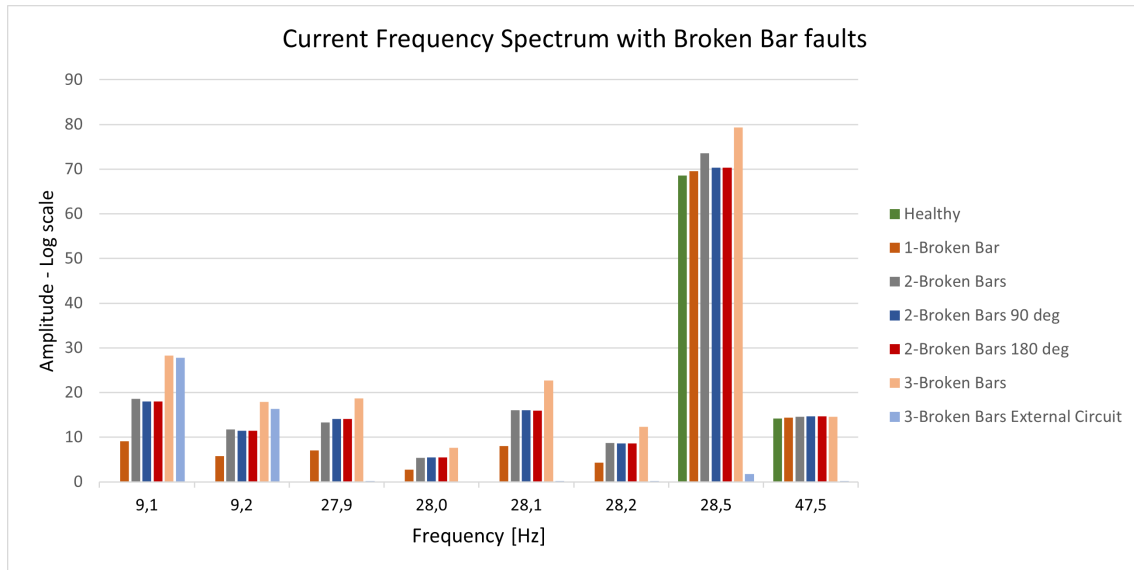


Figure 6.26: Comparison of current frequency components with broken bar fault

6.6.4 Eccentricity Faults

Figure 6.27 and 6.28 show present the frequency amplitude of a selected number of frequency components for healthy, static and dynamic eccentricity. The frequencies are selected by choosing the ones having an amplitude above 0.1 for both static and dynamic eccentricity. The result show a clear increase in several amplitudes when both static and dynamic eccentricity are present. As all multiple of 3 of the fundamental harmonic is not suitable for fault detection as discussed earlier, the frequency amplitude of 85.5[Hz] is excluded from the spectrum. The only frequency components where a rise for only one of the fault types occur is 94.7[Hz], 130.8[Hz] and 187.5 for static eccentricity and 251.7[Hz] for dynamic eccentricity.

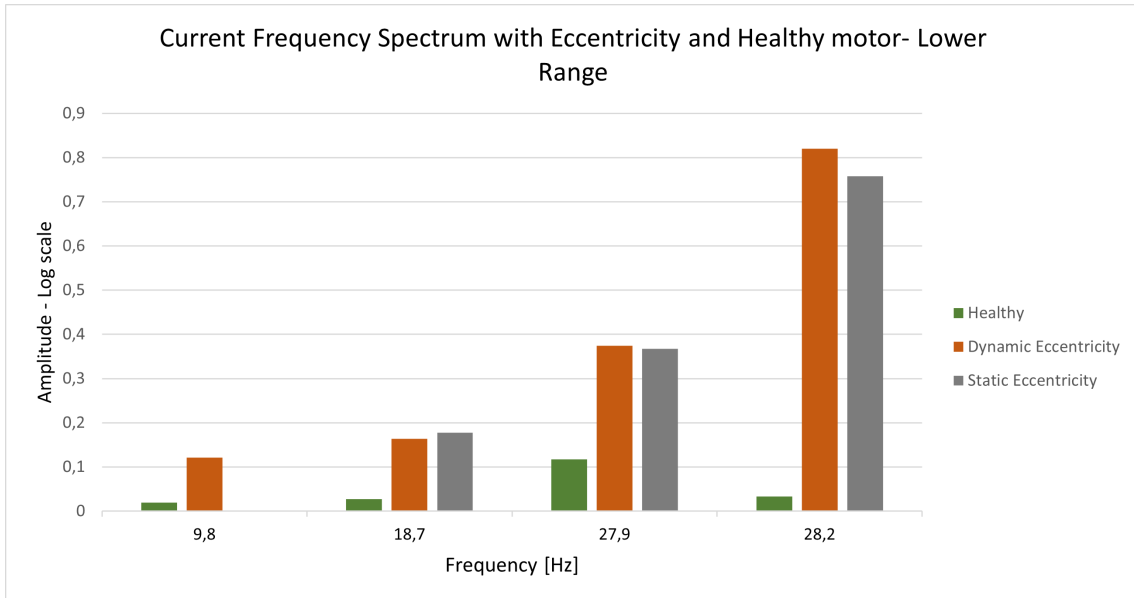


Figure 6.27: Comparison of lower range current frequency components with eccentricity fault

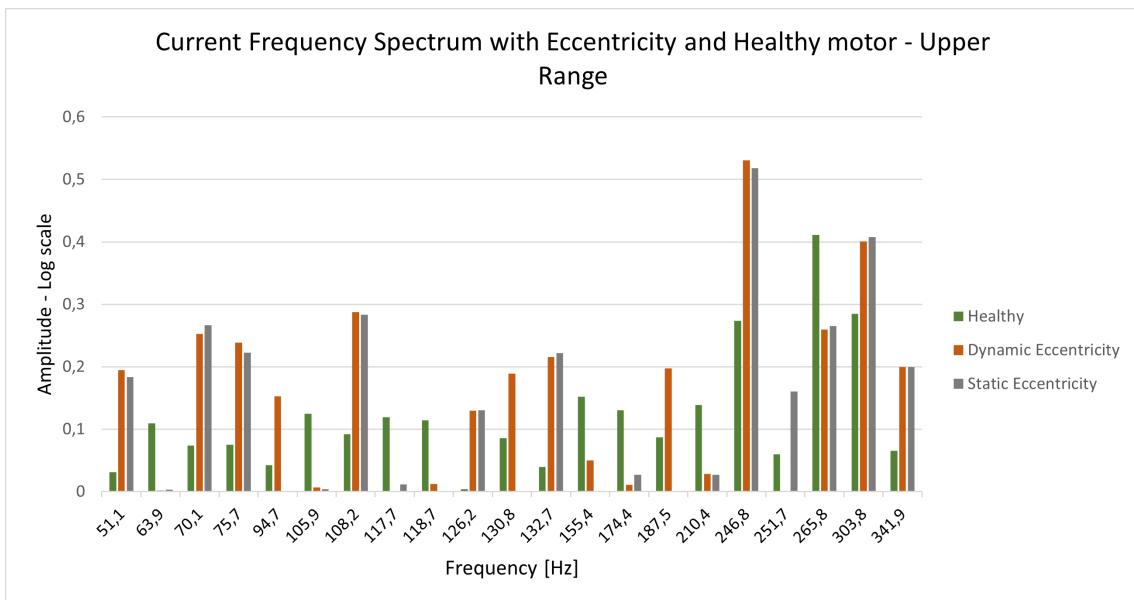


Figure 6.28: Comparison of upper range current frequency components with eccentricity fault

Chapter 7

Discussion

7.1 Healthy motor

The three different models of the healthy motor were made to compare the results from the different fault simulations with the same sampling frequency, signal length and winding excitation. The frequency components presented in section 2.1, describing the current spectrum content of a healthy cage rotor induction motor are listed in table 7.1.

Table 7.1: Current spectrum content - Healthy motor

| Harmonic type | Frequency [Hz] |
|--------------------------------------|-----------------------|
| Rotor Slot Harmonic - Upper | 261.50 |
| Rotor slot Harmonic Lower | 242.49 |
| Saturation Permance Harmonic - Upper | 280.51 |
| Saturation Permance Harmonic - Lower | 223.48 |
| Principal Slot Harmonic - Upper | 237.63 |
| Principal Slot Harmonic - Lower | 218.62 |

By comparing the current frequency spectrum for the healthy motor presented in section 6.1.1 with the harmonics presented in table 7.1, none of the frequencies presented in the literature have an amplitude above 0,1 for the modeled motor. The most significant amplitudes are found at the harmonics which are a multiple of the fundamental, in addition to the 246.81[Hz], 265.82[Hz], 303.84[Hz] and 322.86[Hz].

For the healthy motor without external circuit the amplitudes of the 3rd and 5th harmonic are much higher than for the model with external circuit. The reason for this is the difference in phase connection of the two motors. As the 3rd harmonic of the fundamental frequency and it's multiple is depended on the phase connection, these components are not suitable for fault detection and diagnosis of and induction motor.

7.2 ITSC fault

7.2.1 ITSC Faults in one and two coils

To identify the severity of a fault, the fault must follow a trend where the rise in amplitude follow the increasing fault severity. From the comparison of frequency amplitudes for ITSC faults in one and two coil, presented in figure 6.24 and 6.25, it is clear that the only frequency components following a specific trend are the 28.5[Hz], 85.5[Hz] and 204.5[Hz]. Frequencies which is a multiple of the fundamental is not suitable for fault detection as these can be eliminated based on the type of phase connection. Other frequencies as 280.6[Hz] are close to following this trend, but have a drop in amplitude from 1-turn short circuit to 3- turn short circuit. The other amplitudes have a more random rise and drop in amplitude with increasing fault severity. An interesting aspect of figure 6.25 is the difference in amplitude for the 6-turn short circuit in one phase and 6-turn short circuited, 3 in 2 coils. Depending on the frequency, they switch on having the highest amplitude. Worth to mention is the impact the 9-turn and 12-turn short circuit case have on the rotor slot harmonic frequencies of 242.6[Hz] and 261.6[Hz]. This is the largest increase in amplitude compared to the healthy motor of all frequencies.

7.2.2 ITSC Faults - Percent in one phase

From the comparison of frequency amplitudes for the % ITSC faults in one phase, presented in figure 6.21, 6.22 and 6.23, it is clear that there exist several frequency components with a rising trend in amplitude with increasing fault severity. In addition, there exist several frequency components with a decreasing trend in the amplitude with increasing fault severity. By comparing figure 6.25, with figure 6.21, 6.22 and 6.23, the resulting amplitudes with increasing fault severity are very different for the same frequency components. A reason for this can be the distribution of the short circuited turns. The simulations with 5-20% short circuited turns in one phase are evenly distributed in all parallel branches of one phase. Similar to the case of short circuited turns in one or two coils, a large peak exist for the upper rotor slot harmonic for the most severe fault condition. However, the peak for the lower rotor slot harmonic is significant less. In stead, a higher peak exist for the 204.5[Hz] frequency component.

7.3 Broken Bar Faults

The results presented in figure 6.26, where the amplitudes several frequencies for different broken bar faults are presented, show a clear trend for most of the frequencies. The lower side band harmonics for both the fundamental and the 3rd harmonic component are rising with increased fault severity. This matches the literature presented in section 3.3.2. As mentioned, the lower side band harmonics are visible from the simulations, but the upper side-bands are missing. The reason for this is assumed to be the constant speed of the simulation. The upper side-band is a result of torque ripple and speed oscillation, which doesn't happen in the simulated model. Another interesting finding is the effect of the location of the broken rotor bars. From the comparison in figure 6.26, there doesn't exist any significant changes for the

three different cases of 2 broken bars. The only effect can be seen in the FFT analysis for the 2-broken bar 90 deg case, where the ripple effect in the spectrum is noticeable. A simulation with 3-broken bars with external circuit was done for comparing the two methods. The lower side-bands of the fundamental harmonic are visible both with and without external circuit, but for the remaining frequency components presented in figure 6.26, the contribution from the 3-broken bar with external circuit are barely present. This is assumed to be a result of the difference in phase connection between the two models as described earlier.

7.4 Eccentricity Faults

7.4.1 Static Eccentricity

By comparing the current frequency spectrum of the motor with static eccentricity with the healthy one, as in figure 6.27 and 6.28, it is clear that there exist several frequency component with a significant rise in amplitude when the fault is present. When comparing this result with the literature and the expected frequency components during static eccentricity given by

$$f_e = \left(\frac{n}{p}\right) p f_r, \quad f_r = \frac{\omega_r}{2\pi},$$

there are no match between the two.

7.4.2 Dynamic Eccentricity

From the comparison done in figure 6.27 and 6.28, it is clear that the amplitude of several frequency components of the phase current increase with the presence of dynamic eccentricity. By comparing the frequency components with the literature and expected frequency components, there exist no match.

By comparing the results from static and dynamic eccentricity, there exist several common frequency components with significant rise in amplitude, as expected from the literature in section 3.3.3. There exist several frequency components that are unique for each of the eccentricity faults which can separate the two.

Chapter 8

Conclusion and Further Work

The aim of this master thesis was to investigate a simulation based fault detection and diagnosis technique capabilities of detecting stator short circuit, broken rotor bar and eccentricity faults of a large induction motor. The method is based on the asymmetrical air-gap flux wave distribution when a fault is present. This asymmetrical operation produces sideband harmonic component in the input current which can be detected and identified through harmonic analysis of the stator winding current. The method was investigated by simulating the faults through TSFE simulations and the resulting stator phase current was analyzed. The simulations were done on a model based on the propulsion induction motor installed onboard the polar supply and research vessel SA Agulhaus II. The healthy motor was first made and validated before the model was modified to include the different faults. It is worth to mention that no similar study has been found in the literature, as the novelty of the work include modeling of faults with FEM.

By comparing the results for the ITSC fault in one or two coils and the literature, it exist clear deviations with regards to the harmonic components. The harmonic components presented in the literature does not appear unless a severe ITSC fault is present. In addition, not all of them are present in the frequency spectrum. For the ITSC of one or two coils, the comparison of the frequency components show that there exist three frequency components with a significant rise in amplitude with increasing fault severity. These frequency components are the 3rd and 9th harmonic component of the fundamental in addition to the 204.6[Hz] which is not a multiple of the fundamental frequency. Based on the fact that the 3rd harmonic of the fundamental and multiple of this is not suited for condition monitoring, as these components can be eliminated based on phase connection, it is only the frequency component of 204.6[Hz] which can potentially be used for fault detection and diagnosis. This frequency also show promising results for identify a fault at an incipient stage.

For the ITCS where a percent of all windings in one phase are short circuited, the frequency spectrum looks different from the case above where only one or two coils have short circuited turns. It is clear that there exist several frequency components with a rising trend with fault severity which can be used to identify the fault. In addition, there exist several frequencies with a dropping trend in amplitude with increased fault severity. These trends in combination could potentially be used for fault detection and diagnosis of the induction motor. Based on the fact that 5% short circuited turns in one phase relates to 14 short circuited turns in total,

this method is assumed not suitable for detecting faults at an incipient stage.

For the broken rotor bar faults, it is clear that the lower side band harmonics are present for 1 broken bar, and the amplitude is rising with increased fault severity. The upper side band of the fundamental frequency in the result are not present, contradicting the expectations from the literature. This harmonic is a result of torque ripple and speed oscillations. This effect is not included in the simulations and hence, this side-band is not visible. Based on the results, the method show promising capabilities of detecting broken rotor bar faults at an incipient stage from the appearance of the lower side band harmonic component. A model including the speed oscillation effect due to broken rotor bars is recommended for further work, to have precise results for further developing a digital twin of the motor.

When static or dynamic eccentricity is present in the motor, the results show several potential frequency components that can be used for fault detection and diagnosis. However, there only exist four frequencies that can separate the two faults from each other. Three of these are unique for the dynamic eccentricity and only one is unique for the static eccentricity. This can be a challenge when separating the two different faults from each other is essential.

The work presented in this thesis show clear deviations from the expected results presented in the literature. However, all the faults show significant rise in one or more frequency amplitudes which can potentially be used for fault detection and diagnosis. There also exist frequency components which can identify faults at an incipient stage for the faults evaluated in this thesis. There exist uncertainties to the work presented in this thesis, as limited simulations are performed and the results must be validated with real data to draw any final conclusion.

Recommendations for further work is to verify the results in this thesis with real data from the polar supply and research vessel SA Agulhaus II as the fault modeling methods proposed in this thesis are new and limited research have been done on this topic in the past. A more detailed investigation for the appearance of specific frequency components, especially for ITSC and eccentricity faults, and why they occur should be performed. As there exist several deviations between the literature of induction motor failure signatures and the results presented in this master thesis, a better understanding of the results is recommended. In addition, more simulations with different load conditions and layout of faults should be performed. For the development of a digital twin of the system, this is assumed to be essential in order to build a good virtual model of the induction motor and the propulsion system as a whole.

Bibliography

- Abhinandan, A C and M H Sidram (2017). 'Fault diagnosis of an induction motor through motor current signature analysis, FFT DWT analysis'. In: *2017 4th IEEE International Conference on Engineering Technologies and Applied Sciences (ICETAS)*, pp. 1–7. DOI: 10.1109/ICETAS.2017.8277869.
- Bagheri, Ahmad, Mansour Ojaghi and Amir Bagheri (May 2020). 'Air-gap eccentricity fault diagnosis and estimation in induction motors using unscented Kalman filter'. In: *International Transactions on Electrical Energy Systems* 30. DOI: 10.1002/2050-7038.12450.
- Bazurto, Alvaro, Enrique Quispe and Rosaura Castrillon (Oct. 2016). 'Causes and failures classification of industrial electric motor'. In: DOI: 10.1109/ANDESCON.2016.7836190.
- Beguenane, R. and M.E.H. Benbouzid (1999). 'Induction motors thermal monitoring by means of rotor resistance identification'. In: *IEEE Transactions on Energy Conversion* 14.3, pp. 566–570. DOI: 10.1109/60.790915.
- Chen, P, Y. Xie and S. Hu (2019). 'The Effect of Stator Inter-Turn Short Circuit Faults on Electromagnetic Performances of Induction Motors'. In: *2019 22nd International Conference on Electrical Machines and Systems (ICEMS)*, pp. 1–5. DOI: 10.1109/ICEMS.2019.8921850.
- Cusido, Jordi, Javier Rosero Garcia, E. Aldabas, Juan Ortega and Luis Romeral (Feb. 2005). 'Fault detection techniques for induction motors'. In: vol. 2005, pp. 85–90. ISBN: 0-7803-9343-0. DOI: 10.1109/CPE.2005.1547550.
- Dash, Rudra Narayan, Sangeeta Sahu, Chinmoy Ku. Panigrahi and Bidyadhar Subudhi (2016). 'Condition monitoring of induction motors: — A review'. In: *2016 International Conference on Signal Processing, Communication, Power and Embedded System (SCOPES)*, pp. 2006–2011. DOI: 10.1109/SCOPES.2016.7955800.
- de Waal, R.J.O., A. Bekker and P.S. Heyns (2018). 'Data for indirect load case estimation of ice-induced moments from shaft line torque measurements'. In: *Data in Brief* 19, pp. 1222–1236. ISSN: 2352-3409. DOI: <https://doi.org/10.1016/j.dib.2018.05.115>. URL: <https://www.sciencedirect.com/science/article/pii/S2352340918306218>.
- DNV-GL (2016). *Class programme: DNV GL approval of service supplier scheme*.
- DNV-GL (2020a). *Rules for classification: Part 1 General regulations, Chapter 1 General regulations*.
- DNV-GL (2020b). *Rules for classification: Part 7 Fleet in service, Chapter 1 Survey requirements for fleet in service*.
- Eftekhari, Maryam, Mehdi Moallem, Saeed Sadri and Min-Fu Hsieh (2014). 'Online Detection of Induction Motor's Stator Winding Short-Circuit Faults'. In: *IEEE Systems Journal* 8.4, pp. 1272–1282. DOI: 10.1109/JSYST.2013.2288172.

- Faiz, Jawad, B. M. Ebrahimi and M. B. B. Sharifian (2006). 'Different Faults and Their Diagnosis Techniques in Three-Phase Squirrel-Cage Induction Motors—A Review'. In: *Electromagnetics* 26.7, pp. 543–569. DOI: 10.1080/02726340600873003. eprint: <https://doi.org/10.1080/02726340600873003>. URL: <https://doi.org/10.1080/02726340600873003>.
- Fischman, Rajmil (Aug. 1997). 'The phase vocoder: theory and practice'. In: *Organised Sound* 2, pp. 127–145. DOI: 10.1017/S1355771897009060.
- Geertsma, R.D., R.R. Negenborn, K. Visser and J.J. Hopman (2017). 'Design and control of hybrid power and propulsion systems for smart ships: A review of developments'. In: *Applied Energy* 194, pp. 30–54. ISSN: 0306-2619. DOI: <https://doi.org/10.1016/j.apenergy.2017.02.060>. URL: <https://www.sciencedirect.com/science/article/pii/S0306261917301940>.
- Glowacz, Adam (Sept. 2016). 'Diagnostics of Rotor Damages of Three-Phase Induction Motors Using Acoustic Signals and SMOFS-20-EXPANDED'. In: *Archives of Acoustics* 41, pp. 507–515. DOI: 10.1515/aoa-2016-0049.
- Gonçalves, Mário J. M., Renato C. Creppe, Emanuel G. Marques and Sérgio M. A. Cruz (2015). 'Diagnosis of bearing faults in induction motors by vibration signals - Comparison of multiple signal processing approaches'. In: *2015 IEEE 24th International Symposium on Industrial Electronics (ISIE)*, pp. 488–493. DOI: 10.1109/ISIE.2015.7281516.
- Hansen, Jan Fredrik and Frank Wendt (2015). 'History and State of the Art in Commercial Electric Ship Propulsion, Integrated Power Systems, and Future Trends'. In: *HealthProp* (2020). *Health Prop Project - NTNU*. URL: <https://www.ntnu.edu/imt/healthprop> (visited on 06/06/2021).
- Ibrion, Michaela, Nicola Paltrinieri and Amir R. Nejad (2021). 'Learning from failures in cruise ship industry: The blackout of Viking Sky in Hustadvika, Norway'. In: *Engineering Failure Analysis* 125, p. 105355. ISSN: 1350-6307. DOI: <https://doi.org/10.1016/j.engfailanal.2021.105355>. URL: <https://www.sciencedirect.com/science/article/pii/S1350630721002156>.
- Isermann, R. and P. Ballé (1997). 'Trends in the application of model-based fault detection and diagnosis of technical processes'. In: *Control Engineering Practice* 5.5, pp. 709–719. ISSN: 0967-0661. DOI: [https://doi.org/10.1016/S0967-0661\(97\)00053-1](https://doi.org/10.1016/S0967-0661(97)00053-1).
- ISO (Feb. 2002). *Condition monitoring and diagnostics of machines—Vibration condition monitoring – Part 1: General procedure*. Standard. Geneva, CH: International Organization for Standardization.
- ISO (Nov. 2016). *Mechanical vibration – Measurement and evaluation of machine vibration – Part 1: General guidelines*. Standard. Geneva, CH: International Organization for Standardization.
- Joksimovic, Gojko and Jim Penman (Nov. 2000). 'The detection of inter-turn short circuits in the stator windings of operating motors'. In: *Industrial Electronics, IEEE Transactions on* 47, pp. 1078–1084. DOI: 10.1109/41.873216.
- Joksimovic, Gojko, Jaksa Riger, Thomas Wolbank, Nedjeljko Peric and Mario Vasak (Oct. 2011). 'Stator line current spectrum content of a healthy cage rotor induction machine'. In: pp. 113–118. DOI: 10.1109/DEMPED.2011.6063610.

- Khalifa, Fahim, Sobhy Dessouky, Mohamed Ismail and Basem El Elnaghi (Jan. 2010). 'Effect of Temperature Rise on the Performance of Induction Motors'. In: pp. 549–552. DOI: 10.1109/ICCES.2009.5383074.
- Kirtley, James L., Arijit Banerjee and Steven Englebretson (2015). 'Motors for Ship Propulsion'. In: *Proceedings of the IEEE* 103.12, pp. 2320–2332. DOI: 10.1109/JPROC.2015.2487044.
- Lei, Yaguo (2017). *Intelligent fault diagnosis and remaining useful life prediction of rotating machinery*. Elsevier Inc.
- Mais, Jason (2002). *Spectrum Analysis - The key features of analyzing spectra*. URL: https://www.skf.com/binaries/pub12/Images/0901d1968024acef-CM5118-EN-Spectrum-Analysis_tcm_12-113997.pdf (visited on 04/05/2021).
- Miljković, Dubravko (June 2015). 'Brief Review of Motor Current Signature Analysis'. In: *CrSNDT Journal* 5, pp. 14–26.
- Mortazavizadeh, Seyed Abolfazl (Jan. 2014). 'A Review on Condition Monitoring and Diagnostic Techniques of Rotating Electrical Machines'. In: *Physical Science International Journal* 4, pp. 310–338. DOI: 10.9734/PSIJ/2014/4837.
- Nandi, Subhasis, Thirumarai Chelvan Ilamparithi, Sang Bin Lee and Doosoo Hyun (2011). 'Detection of Eccentricity Faults in Induction Machines Based on Nameplate Parameters'. In: *IEEE Transactions on Industrial Electronics* 58.5, pp. 1673–1683. DOI: 10.1109/TIE.2010.2055772.
- Nejad, Amir R., Etienne Purcell, Mostafa Valavi, Roman Hudak, Benjamin Lehmann, Francisco Gutiérrez Guzmán, Felix Behrendt, Angelo Mario Böhm, Franz von Bock und Polach, Brendon M. Nickerson, Anriette Bekker and Withold Drazyk (2021). 'CONDITION MONITORING OF SHIP PROPULSION SYSTEMS: STATE-OF-THE-ART, DEVELOPMENT TREND AND ROLE OF DIGITAL TWIN'. In:
- RELJIC, D., D. JERKAN, Darko Marcetic and D. Oros (Jan. 2016). 'Broken Bar Fault Detection in IM Operating Under No-Load Condition'. In: *Advances in Electrical and Computer Engineering* 16, pp. 63–70. DOI: 10.4316/AECE.2016.04010.
- Safety4sea (2019). *Machinery failure the top cause of shipping incidents in last decade*. URL: <https://safety4sea.com/machinery-failure-the-top-cause-of-shipping-incidents-in-last-decade/> (visited on 28/04/2021).
- Sapena-Bano, A., F. Chinesta, M. Pineda-Sanchez, J.V. Aguado, D. Borzacchiello and R. Puche-Panadero (2019). 'Induction machine model with finite element accuracy for condition monitoring running in real time using hardware in the loop system'. In: *International Journal of Electrical Power and Energy Systems* 111, pp. 315–324. ISSN: 0142-0615. DOI: <https://doi.org/10.1016/j.ijepes.2019.03.020>. URL: <https://www.sciencedirect.com/science/article/pii/S0142061518330126>.
- Shrivastava, Amit and Sulochana Wadhvani (Jan. 2012). 'Vibration signature analysis for Ball Bearing of Three Phase Induction Motor'. In: *IOSR Journal of Electrical and Electronics Engineering* 1. DOI: 10.9790/1676-0134650.
- Supangat, R., N. Ertugrul, W.L. Soong, D.A. Gray, C. Hansen and J. Grieger (2005). 'Broken rotor bar fault detection in induction motors using starting current analysis'. In: *2005 European Conference on Power Electronics and Applications*, 10 pp.–P10. DOI: 10.1109/EPE.2005.219402.

- Tavner, P.J., Li Ran, Jim Penman and Howard Sedding (Jan. 2008). 'Condition Monitoring of Rotating Electrical Machines'. In: *Bibliovault OAI Repository, the University of Chicago Press*. DOI: 10.1049/PBP0056E.
- UiO (2019). *Optimalisering av FFT - IN2060 - Høst 2019 - Universitetet i Oslo*. URL: <https://www.uio.no/studier/emner/matnat/ifi/IN2060/h19/obliger/oblig3/oppgave.html> (visited on 21/05/2021).
- Valavi, Mostafa, Kari Gjerde Jørstad and Arne Nysveen (2018). 'Electromagnetic Analysis and Electrical Signature-Based Detection of Rotor Inter-Turn Faults in Salient-Pole Synchronous Machine'. In: *IEEE Transactions on Magnetics* 54.9, pp. 1–9. DOI: 10.1109/TMAG.2018.2854670.
- Wärtsilä (2018). *Wärtsilä propulsion condition monitoring service brochure*.
- Zaabi, W., Y. Bensalem and H. Trabelsi (2014). 'Fault analysis of induction machine using finite element method (FEM)'. In: *2014 15th International Conference on Sciences and Techniques of Automatic Control and Computer Engineering (STA)*, pp. 388–393. DOI: 10.1109/STA.2014.7086711.
- Zhang, Pinjia, Yi Du, Thomas G. Habetler and Bin Lu (2011). 'A Survey of Condition Monitoring and Protection Methods for Medium-Voltage Induction Motors'. In: *IEEE Transactions on Industry Applications* 47.1, pp. 34–46. DOI: 10.1109/TIA.2010.2090839.

